Spring 2010

Development and validation of a robust model to predict the response of wave energy conversion devices

James Wright
University of New Hampshire, Durham

Development and Validation of a Robust Model to Predict the Response of Wave Energy Conversion Devices

BY

James Wright

BSME, University of California at Berkeley, 2004

THESIS

Submitted to the University of New Hampshire
in Partial Fulfillment of
the Requirements for the degree of

Master of Science

in

Mechanical Engineering

May 2010

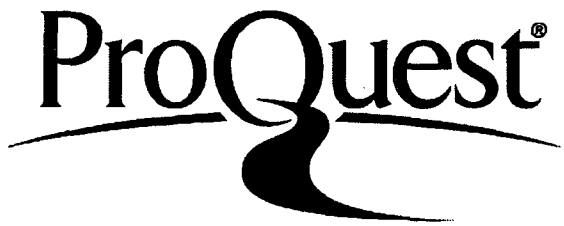

ProQuest LLC
789 East Eisenhower Parkway
P.O. Box 1346
Ann Arbor, MI 48106-1346

This thesis has been examined and approved.

Thesis Director, Christopher M. White
Assistant Professor of Mechanical Engineering

M. Robinson Swift
Professor of Mechanical Engineering and Ocean Engineering

May-Win L. Thein
Associate Professor of Mechanical Engineering

5/03/10
Date

ACKNOWLEDGMENTS

I would like to thank my advisor, Professor Christopher White, for his guidance and encouragement throughout this project. I also thank Professor Robinson Swift for the opportunities he gave me to learn and evolve as a research scientist.

I thank Professor Kenneth Baldwin, Judson DeCew, Ryan Despins and all the members of the Chase Ocean Engineering Laboratory for their help and support.

I would also like to acknowledge Michael Allard, Colin Fischer, Tania Grindrod, Jessica Murray, and Kyle Russ for their part in developing the ocean wave energy prototype evaluated in this thesis.

I am grateful for the moral and intellectual support of my colleagues Gopala Mulukutla, Timothy Pickett, Gary Margelowsky, Sylvia Rodriguez-Abudo, and Donya Frank.

Thank you family and friends for supporting me, and to my college sweetheart Anjuli Appapillai for making every day better than the last.

Table of Contents

List of Tables

List of Figures

ABSTRACT

Development and Validation of a Robust Model to Predict the Response of Wave Energy Conversion Devices

by

James Wright
University of New Hampshire, May, 2010

In this study, a computer model of the dynamics and generator output of a point-absorber-type wave energy converter (WEC) was developed and evaluated against a 1:25 scale prototype in wave tank tests. The WEC consists of a circular wave follower buoy with a central hole which fits over a slender spar buoy that extends up through the follower buoy opening. The wave follower buoy slides axially on the spar, providing relative motion for the power take-off unit consisting of a rack-and-pinion configuration connected through gears to a permanent magnet generator. Linear wave theory is applied to determine the response of the floating buoys to ocean wave excitation, while the coupled dynamics of the internal components of the power take-off system are derived from first principals where possible and characterized experimentally. Analysis is performed in the time domain where the dynamics of the WEC can be optimally evaluated.

Model validation was completed by way of mechanical bench testing and by comparing predictions and measurements obtained in an independent series of wave tank experiments. The robustness of the model was investigated by evaluating

its accuracy at predicting WEC performance with and without a damping plate attached to the spar buoy.

The results show good correlation of the predicted model performance to measured positional data and power generation. In regular waves, the predicted average power generation was within 6-54% of the measured value for configurations without the damping plate attached to the spar. With the addition of the damping plate attached to the spar, model predictions improved to within 0.9-37% of the measured value. A similar trend was observed for the power generation predictions in irregular sea states. Predictions of average power generation in irregular sea were within 55-510% of the measured value for configurations without the damping plate attached to the spar, and within 12-33% of the measured value for configurations with the damping plate attached to the spar.

CHAPTER 1

INTRODUCTION

1.1 Objective

The objective of this research is to develop and experimentally validate a numerical model of a point-absorber type wave energy conversion device that can accurately predict behavior and performance in a variety of sea states. The model should be both modular and robust in its ability to accommodate the physical uniqueness of a particular design, such that the internal workings describing the power extraction system may be interchanged or replaced to include a wide variety of available technologies (i.e., Permanent Magnet linear generator or hydraulic pump).

1.2 Motivation

The ability to accurately model Wave Energy Converters (WEC) is a critical step required to gain a solid understanding of the device's operation and performance. Knowledge of the interactions between wave forcing and WEC system response plays a crucial role in making a confident transition from a cost-effective small-scale prototype WEC, to intermediate, then full-scale system. The development of large oceangoing structures generally undergo validation at increasing

scales, typically abiding by the *Irish Protocol* (A scale-up process developed by the Irish Hydraulic and Maritime Research Centre, and based on the NASA Space Exploration Protocol). Oceangoing energy generation systems are not exempt from the scaled assessment of performance and require the inclusion of their internal energy extraction components to accurately predict the device operation.

The focus of this research is to develop a robust modular model that allows for modification or substitution of major components. Utilizing such a model, sound decisions may be implemented to optimize the performance of unique systems at each production scale. The benefit of discovering optimization methods or critical survivability flaws during scaled trials or by computational modeling, as opposed to after a full-scale device has been constructed, is a significant cost and time savings.

1.3 Ocean Energy and Extraction Methods

1.3.1 The Ocean as an Energy Resource

Ocean waves are created by the interactions between water and air. The energy transfered to the ocean becomes spatially concentrated as the sea develops, resulting in an increase of wave size. The energy is then, rather efficiently, delivered to coastal regions.

The total amount of energy contained in a water wave can be determined by independently examining its potential and kinetic energy. For the progressive regular wave illustrated in Figure 1-1, the potential energy is that required to raise water mass from the trough to the crest of a wave. As shown by Dean and Dalrymple

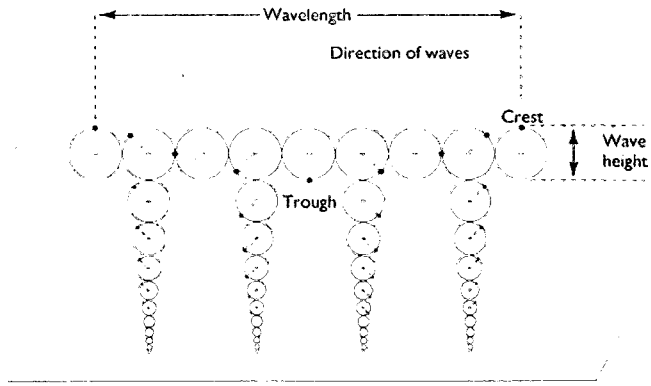

Figure 1-1: Progressive deep water wave with particle excursion shown.

(1984), the average potential energy per unit surface area can be calculated as

$$\overline{\mathbf{PE}} = \frac{1}{16}\rho g H^2, \tag{1.1}$$

where ρ is the density of the water, g is the gravitational force, and H is defined as the wave height.

The kinetic energy of water waves is related to the movement of water particles, which is both horizontal and vertical. Utilizing solutions for water particle velocities under a progressive wave, the kinetic energy per unit surface area is calculated to be

$$\overline{\mathbf{KE}} = \frac{1}{16}\rho g H^2. \tag{1.2}$$

Hence, the potential and kinetic energy associated with ocean waves is equal. The sum of the potential and kinetic energy per unit surface area provides the total energy, E,

$$E = \overline{\mathbf{PE}} + \overline{\mathbf{KE}} = \frac{1}{8}\rho g H^2. \tag{1.3}$$

The transport, or *Flux* of this energy can be calculated to provide an average

wave power per unit width of wave front by multiplying by the speed at which the energy is being transported. For deep water, the average power per unit wave front can be calculated as

$$\overline{P} = E\,C_g = E\left(\frac{1}{2}\cdot\frac{g}{2\pi}\right)T, \tag{1.4}$$

where C_g is the group velocity, the speed at which trains of waves travel, and T, the time it takes for two consecutive wave crests to pass a reference point, is the wave period.

However, the real ocean surface is irregular and comprised of a assortment of waves which appear random, varying in heights, frequencies, and incident directions. The energy present in the ocean is therefore variable and dependent on many factors, such as:

- The local wind conditions which change on the order of seconds, and on the arrival of distant swells that can take hours to days for arrival.
- The location and direction of the originating wind field.
- Energy lost near shore because of the wave frictional interaction with the seabed.
- Diffraction caused by interaction with shoreline geography, which can both focus and diffuse the energy in localized areas.

The resulting surface profile at a specific location may look similar to that of Figure 1-2. A common method used to characterize the wave height distribution in such a sea is to determine the *significant* wave height, $H_{1/3}$. Defined as the average height of the highest $1/3$ of waves, the significant wave height can be determined

by utilizing the root mean square (H_{RMS}) of a series of wave heights occurring at a specific location

$$H_{RMS} = \sqrt{\frac{1}{N}\sum_{i=1}^{N} H_i^2}, \tag{1.5}$$

where N is the total number of waves detected over the range of time evaluated, and H_i is the individual wave height of waves $i = 1$ to N. The significant wave height is then calculated as

$$H_{1/3} = \left(\sqrt{ln\left(\frac{1}{1/3}\right)} + \sqrt{\frac{\pi}{2/3}}\, erfc\left(\sqrt{ln\left(\frac{1}{1/3}\right)}\right)\right) H_{RMS}$$

$$H_{1/3} \approx (1.416)\, H_{RMS}. \tag{1.6}$$

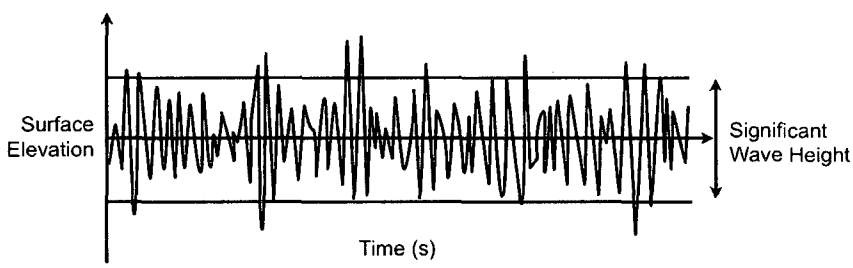

Figure 1-2: Surface elevation over time with the significant wave height illustrated.

Utilizing the significant wave height, determination of the average energy associated with a unit area of sea composed of irregular waves can be calculated as

$$\mathbf{E} = \frac{\rho g H_{1/3}^2}{16} = \int_0^\infty S(f)d(f), \tag{1.7}$$

where $S(f)$ is the wave spectrum, which quantitatively describes how different wave frequencies contribute to the wave energy. The *Flux*, of this energy can be calculated

by multiplying the energy per unit surface area by the velocity at which the energy is being delivered. In doing so, the average power being delivered by waves at any location can be determined. An estimate of the worldwide distribution of wave power, averaged over a yearly cycle as described by Thorpe (1992), is shown in Figure 1-3.

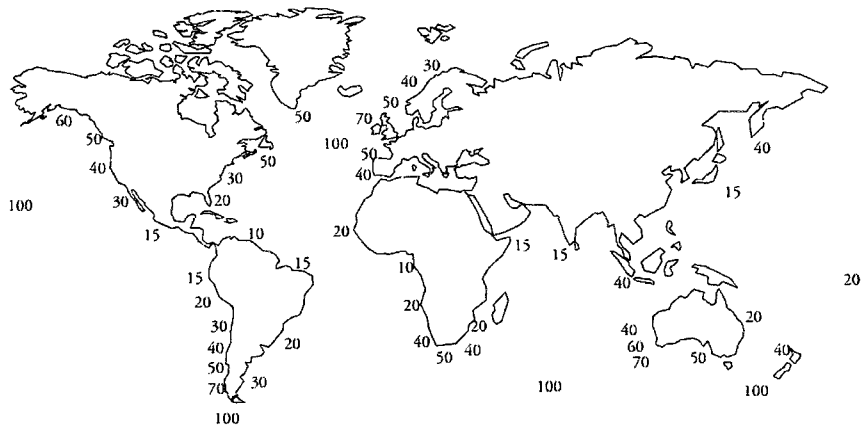

Figure 1-3: Approximate worldwide distribution of wave energy. Given as kW/m of wave front.

SInce major wind systems generate the ocean waves, there are significant contributions from extra-tropical storms and trade winds. In areas such as the Indian subcontinent, local monsoons also heavily influence the wave climate. As described in further detail by Brooke (2003), the Northern Hemisphere experiences north-easterly tracking extra-tropical cyclones, building waves in the storm's southern sector, which travel in the same direction as the storm. Conversely, waves that are generated in the northern sector of the Northern Hemisphere cyclone travel in the opposite direction to that of the storm. As such, swells traveling *backwards* from such a storm have much less power then swells leaving the storms southern sector. This results in wave resources along the western part of an ocean basin generally

being less energetic, as is evident by the lower annual average wave-power levels along North America's eastern continental shelf.

The disparity in wave power distribution, in favor of the European western coastlines, has contributed to the effect of increased academic research and private company investment in Europe (Cantillon-Murphy, 2005). However, Europe is not the only one with vested interest in wave energy as there has been significant interest and investment in wave-power in Australia, the United States, and Japan. As the economics governing the support for this technology continue to improve, the strategic investments will as well.

1.3.2 Methods of Extracting Energy from Ocean Waves

In order for a energy-extraction device to be effective, it must destructively interfere with the incident wave. In other words, "...for an oscillating system to be a good wave absorber it should be a good wave generator." (J. and K., 1978)

Inherent in the processes of extracting energy from ocean waves is the conversion of that energy to another form. As explained by Falnes (2007), the primary conversion of energy occurs when energy is transferred from the wave to the oscillating system. That oscillating system could be composed of one or more floating bodies, solid or flexible. Alternatively, water could be oscillating within a structure that is floating, on the seabed, or located on shore. The second conversion step takes the oscillatory motion of the system and makes it into a more useful form of mechanical energy, e.g. rotating shafts, racks and pinions, hydraulics, or pneumatic components. If electricity is to be generated, then an electric generator can serve as

the tertiary conversion step. During each conversion step, thermodynamics dictates an inefficient transfer of energy. Therefore, the device must be optimized in order to extract the maximum amount of power.

There are innumerable device concepts and developed technologies for converting wave energy to electricity, many of which are outlined by Mike Previsic (2004) and Vining (2007). Most of these wave energy converters (WEC), however, can be generally placed into one of several categories described below.

Oscillating Water Columns

Oscillating water column (OWC) devices generally operate by utilizing a submerged chamber with a large opening below the sea level and a smaller opening above the sea level for air to pass through. The action of the waves entering the chamber has the oscillating effect of both forcing and drawing air through the smaller air opening, as illustrated in Figure 1-4. In this way, the OWC converts the relatively slow movement of ocean waves into a high velocity airflow capable of powering turbines for electricity generation.

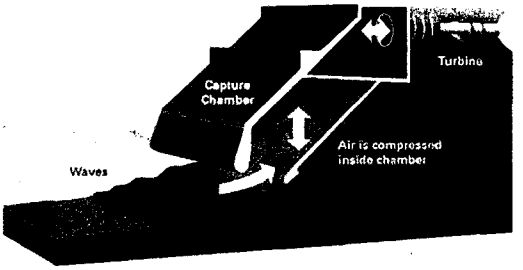

Figure 1-4: Diagram of an oscillating water column device.

Overtopping Devices

Overtopping devices operate by elevating ocean waves to a reservoir above sea level, then allowing water at an increased head pressure to run a specially designed turbine. Most designs utilize a narrowing channel that increases the height of waves as they travel along its length, allowing water to spill into the reservoir at the base. An example of an overtopping device currently deployed in Nissum Brendning, Denmark is the Wave Dragon and is shown in Figure 1-5.

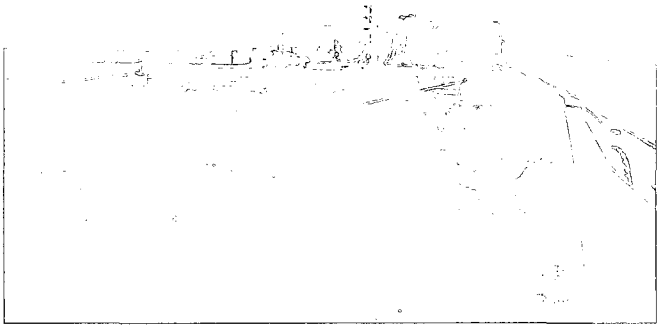

Figure 1-5: Overtopping Device: The Wave Dragon.

Surging Devices

Surging devices typically consist of articulated structures residing at the surface of the ocean. Wave-induced motion at the joints, caused by pitching and surging, is then resisted by a mechanical power take-off system. An example of this type of device is known as Pelamis. This device, developed by Pelamis Wave Power (2009) in Edinburg, Scotland, is composed of cylindrical sections and linked by hinged joints. Energy is extracted from the joint movement by hydraulic rams, which pump high-

pressure oil through hydraulic motors via smoothing accumulators. The hydraulic motors then drive electrical generators to produce electricity. A photograph of a Pelamis is shown in Figure 1-6.

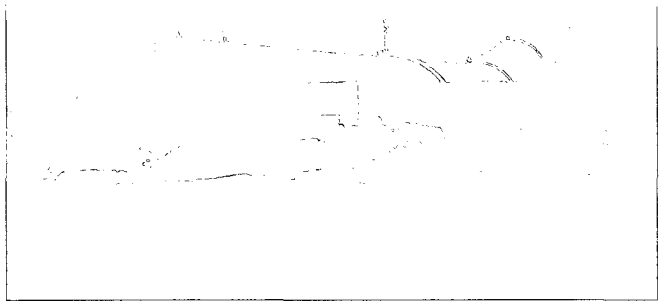

Figure 1-6: Surging Device: Photograph of the Pelamis WEC.

Point Absorber

Point absorber devices are named after their typically small surface size compared to the prevailing wavelength. These devices generally utilize wave induced heaving motion to react against either a rigid mooring or another component that is oscillating out of phase, thereby creating relative motion.

An example of a submerged point-absorber WEC is the Archimedes Wave Swing (AWS, 2009), shown in Figure 1-7. This device operates by utilizing the dynamic pressure field below the waves. As a wave crest approaches, the water pressure on the top of the device increases and the upper section, which is filled with a gas, compresses to balance the pressure. The reverse happens as the wave trough passes and the upper section expands. The relative movement between the upper and

lower part is then converted to electricity by means of a hydraulic system coupled to a generator.

Figure 1-7: Point Absorber: Archimedes Wave Swing prior to being submerged to its operating depth.

Another common point-absorber configuration is composed of two major components, a floating section that utilizes its buoyancy to rise and fall with the ocean waves and a second component against which to react to. In the case of Finavera's AquaBuoy 2009 design (Figure 1-8), the cylindrical floating component reacts against the mass of entrapped water contained within a long submerged tube section open to the sea at the bottom. Relative motion between the main floating body and a piston within the submerged tube section contracts and expands a unique hose-pump, from which power is generated.

Alternatively, as in the case of Ocean Power Technologies (OPT) PowerBuoy shown in Figure 1-9, the point absorber configuration consists of a surface following element that reacts against a massive spar designed to resist heave motion. The resulting mechanical stroke is converted via a power take-off mechanism to drive an electrical generator.

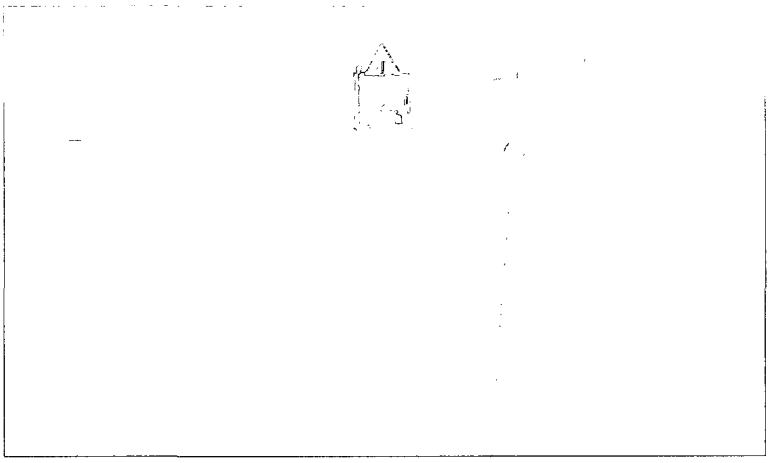

Figure 1-8: Point Absorber: Illustration showing conceptual AquaBuoys deployed in the ocean environment.

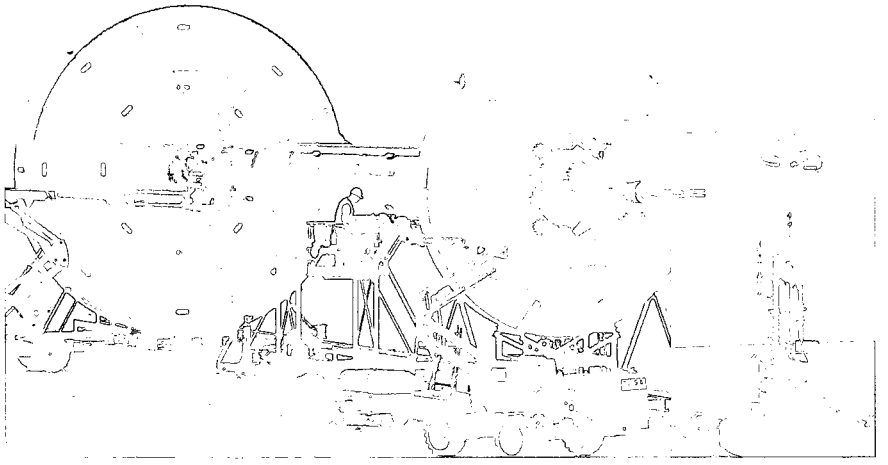

Figure 1-9: Point Absorber: Images of two versions of OPT's PowerBuoy.

1.4 Approach

The present work is to analyze a two-bouy point absorber. Owing to the complexities of WEC devices, a systematic approach was employed. First an analytical examination of the forces which define the system dynamics was performed. Next, the WEC system was reduced to several subsystems that were modeled on first principles. These major subsystems include: two concentrically-oriented buoys that heave due to forcing of incident waves, a mechanical transmission system that conditions relative motion for energy extraction, and a power take-off device that generates electricity. Each of the subsystems are illustrated in Figure 1-10.

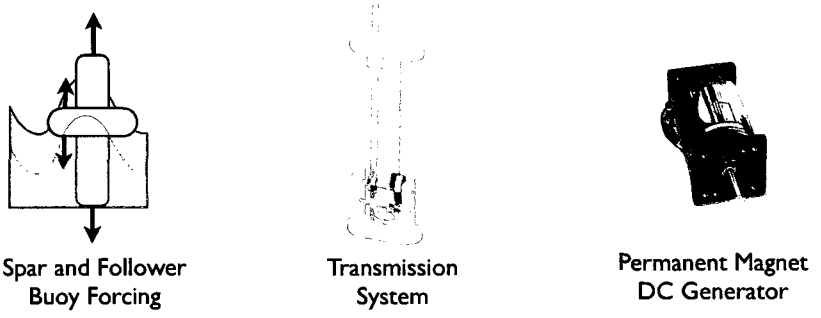

Figure 1-10: Illustration of the WEC subsystems

The subsystem models were experimentally validated by performing parametric tests on the response of each individual subsystem, then coupled subsystems. Bench-top experiments were performed on the transmission system, the PM DC generator, and the coupled transmission and generator utilizing a wave motion simulator. Wave tank validation of uncoupled spar and follower buoy's heave motions were performed by tracking their motion over a range of regular waves and making comparisons to values predicted by the model. Finally, the coupled WEC system

model was validated by comparing its predicted motion and power generation to that of a functional prototype in both regular and irregular waves. The robustness of the model was further investigated by comparing the predicted model performance to the experimentally measured performance using a submerged damping plate attached to the spar to alter its hydrodynamic behavior.

Utilizing results from the comparative analysis between experiments and simulations, conclusions were drawn and scaled performance predictions were made for a full size device.

CHAPTER 2

Development of Computational Model

2.1 System Description

The WEC system under investigation consists of two concentric buoys which are able to heave in ocean waves relative to one another as shown in Figure 2-1. The relative oscillation occurs as a result of significant differences in both the geometry and inertia of each of the buoys. The spar buoy is the long, vertical cylinder which is centrally located with much of its length submerged below the surface. The spar is optionally configured with a circular damping plate attached to its bottom end via a rigid rod. Surrounding the spar is a modified torus shaped buoy, referred to as the follower. The follower has a high buoyancy and floats horizontally on the water surface.

The two buoys are coupled via a frame that is rigidly attached above the follower buoy, which extends downward a toothed-rack into the top of the spar buoy (see detailed section in Figure 2-1). The rack contacts a pinion mounted internally in the spar, thus enabling the conversion of relative linear motion into rotational motion. The rotational speed is increased by a gear train coupled to a permanent magnet DC generator as shown in Figure 2-1, enabling power generation.

This WEC system can be organized into four major subsystems. The first two

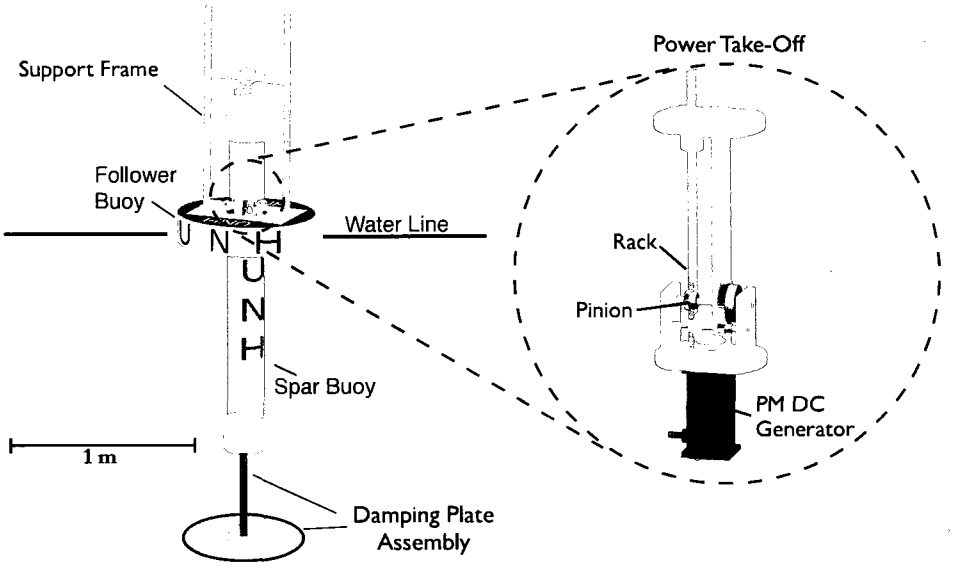

Figure 2-1: Illustration of the WEC system in its neutral position, with a detailed enlargement of the transmission and generator.

subsystems are comprised of the incident wave forcing acting on the spar and follower buoys. The third subsystem contains the internal transmission, including the rack-and-pinion and gearing mechanism. The fourth subsystem describes the complete operation of the permanent magnet DC Generator. Each of these subsystems are further developed in the following sections.

2.2 Incident Wave Forcing

For a single free-floating buoy in still water, two forces that hold the buoy in vertical equilibrium are the weight, W, of the buoy acting downwards,

$$W = m\,g = \rho g A D, \tag{2.1}$$

and the pressure of the fluid, P_{static}, acting upwards on bottom of the buoy,

$$P_{static} = \rho g A D, \tag{2.2}$$

where m is the mass of the buoy, ρ is the density of salt water, g is the gravitational constant, A is the cross-sectional area of the buoy, and D is defined as the draft of the buoy in still water. Figure 2-2 (a) shows a free floating buoy subjected to its weight force and static water pressure.

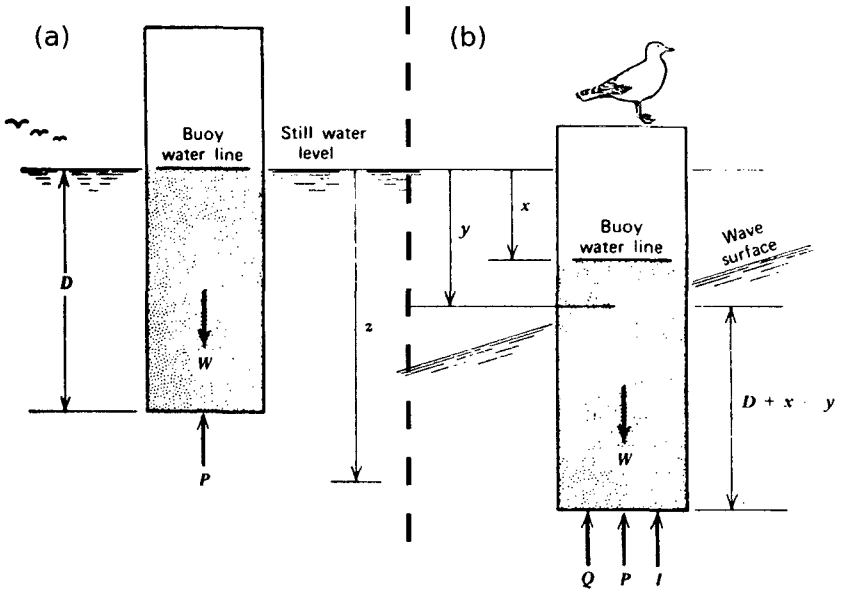

Figure 2-2: (a) Reference frame for a free floating ocean buoy in still water. (b) Reference from of the same buoy experiencing additional vertical forcing due to an incident wave, where the values P, Q, I, and W are the *pressure*, *viscous*, *inertial*, and *weight* forces, respectively. (Berteaux, 1976)

If the coordinates are defined such that the still water surface acts as the zero reference with the positive z-direction measured downwards, as in Figure 2-2 (b), then from this still water reference, the vertical distance to the buoy water line is given by x and the vertical distance to the wave surface is given by y.

In the presence of waves, the pressure force becomes dynamic and dependent on the relative position of the buoy to the height of the incident wave. By using small-amplitude wave theory (Berteaux, 1976), the dynamic pressure can be approximated as

$$P = \rho g A \left(D + x - y\, e^{-k(x+D)} \right), \tag{2.3}$$

where $k = \frac{2\pi}{L}$ is defined as the *wave number*, L is the incident wave length, and $e^{-k(x+D)}$ is an attenuation term which accounts for the diminishing fluid particle velocity field below surface waves in deep water. For buoys of large draft that extends beyond one half the length of the incident wavelength, the attenuation term is approximately equal to e^{-kD}, while for small drafts, where the buoys rests near the surface the attenuation term can be neglected.

In addition to dynamic pressure effects in the presence of waves, a damping force acting between the buoy and water interface arises due to viscosity. In the linear assumption, this damping force is proportional to the relative speed between the buoy and the water particles. If the buoy speed is represented by $\dot{x}$ and the speed of the water by $\dot{y}e^{-kz}$, then the damping force due to viscosity is

$$Q = b \left(\dot{x} - \dot{y}\, e^{-kD} \right), \tag{2.4}$$

where b is the linear coefficient of friction and most of the damping is assumed to be occurring at the bottom of a large draft buoy.

During the acceleration of a buoy immersed in water, not only is the mass of the buoy accelerated but also the mass of a certain amount of water entrained in the

motion, i.e., water close to or ahead of the buoy. As a result, an *added* mass term is included by examining the force required to accelerate a body in water compared to in vacuum.

$$\begin{aligned} F'_{water} &> F_{vacuum} \\ (m + m')\, a &> m\, a \end{aligned} \tag{2.5}$$

In Equation 2.5, m' is the added mass. The inclusion of added mass as an inertial force opposing relative acceleration between the buoy, $\ddot{x}$, and water, $\ddot{y}e^{-kz}$, for the case of a large buoy draft is

$$I = m' \left(\ddot{x} - \ddot{y}\, e^{-KD} \right). \tag{2.6}$$

The forces described above, with the exception of the buoy weight, are each dependent on the immediate wave dynamics, both on and below the surface. To investigate these dependencies and their effects, regular and irregular waves are defined in greater detail below.

2.2.1 Regular Waves

For regular incident waves, the wave surface elevation is approximated by a sinusoidal function

$$y = r\, cos(\omega t), \tag{2.7}$$

where ω is the wave angular frequency equal to $\frac{2\pi}{T}$, T is the period of the wave, and r is the wave amplitude. The resulting surface profile is shown in Figure 2-3.

Taking sequential derivatives of the time-dependent surface elevation in Equation 2.7, for a constant wave period, provides the vertical velocity of water particles at the surface

$$\dot{y} = -\omega r sin(\omega t), \tag{2.8}$$

and the acceleration of those particles

$$\ddot{y} = -\omega^2 r cos(\omega t). \tag{2.9}$$

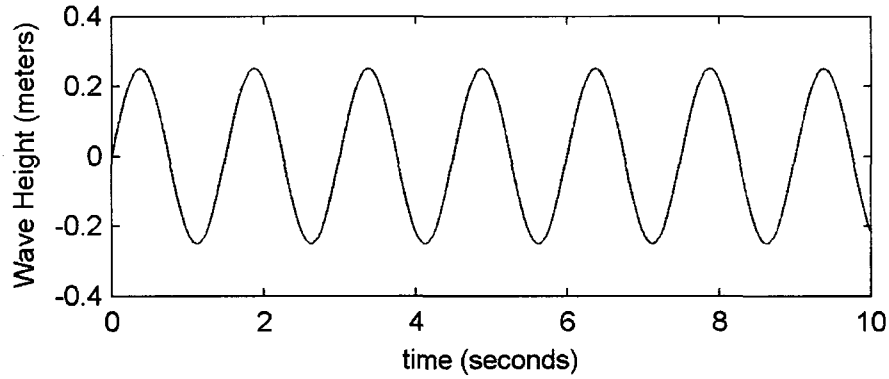

Figure 2-3: Regular wave sea surface profile as a function of time

The dispersion relation for deep water waves is used to define a relationship between the angular frequency, ω, and wavelength L (Dean and Dalrymple, 1984). The general form of the dispersion relation can be written as

$$\left(\frac{2\pi}{T}\right)^2 = g\left(\frac{2\pi}{L}\right) tanh\left(\frac{2\pi}{L}h\right). \tag{2.10}$$

For deep water, commonly denoted as a depth greater than half the wavelength, the hyperbolic tangent in Equation 2.10 approaches unity

$$tanh\left(\frac{2\pi}{L}h\right) \rightarrow 1 \ \ (in\ deep\ water). \tag{2.11}$$

Therefore, the wavelength can be assumed to be a function of only the wave period squared and the gravitational constant

$$L = \frac{gT^2}{2\pi}. \tag{2.12}$$

2.2.2 Irregular Seas

In the ocean, an irregular sea surface prevails most of the time. However, despite the absence of regularity, there are predominant features which are present for any given sea. These features can be quantified using statistical analysis of a surface profile for a given time span. The probability of waves with specific heights and periods that define a given sea state is commonly referred to as the wave spectral density.

There are several empirical formulas designed to represent a wide variety of sea states based on historic records of wave amplitudes from several locations around the world. For this research, both numerical simulation and wave tank experiments are confined to random sea states defined by the Bretschneider Spectrum, as this spectrum accurately portrays the fully developed sea states found off the northeastern US coastline. The Bretschneider Spectrum utilizes the significant wave height

and modal period in its formation and can be calculated as

$$S(\omega) = \frac{1.25}{4}\frac{\omega_m^4}{\omega^5} H_{1/3}^2 \, e^{-1.25(\omega_m/\omega)^4} \quad (meter^2 \cdot sec), \tag{2.13}$$

were $H_{1/3}$ is the significant wave height and ω_m the modal frequency. A plot of a particular Bretschneider spectrum is shown in Figure 2-4 with a corresponding surface profile.

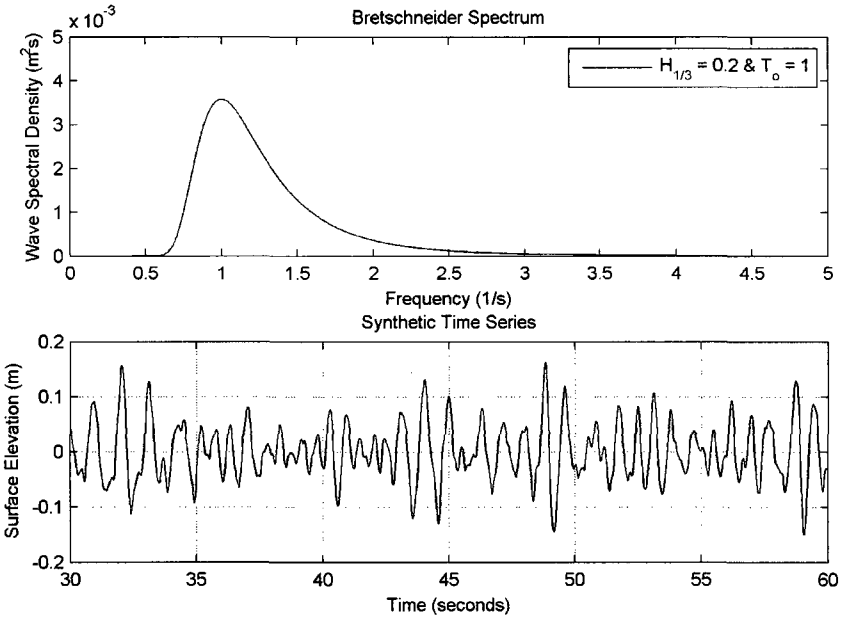

Figure 2-4: Brentschneider wave spectrum generated and corresponding time series surface elevation.

2.2.3 Equations of Motion

The forces acting on a buoy and the regular or random sea wave definitions can be combined to obtain the equation of vertical motion for a partially submerged

buoy as determined by Newton's second law of motion given by

$$W - \rho g A(D + x - y\, e^{-K\,D}) - b(\dot{x} - \dot{y}\, e^{-K\,D}) - m'(\ddot{x} - \ddot{y}\, e^{-K\,D}) = m\ddot{x}. \quad (2.14)$$

Expanding on the concept of a single buoy to a two buoy system, a set of two equations can be derived that accounts for the unique properties of both buoys

$$\begin{aligned} W_1 - \rho g A_1(D_1 + x_1 - y\, e^{-K\,D_1}) - b_1(\dot{x}_1 - \dot{y}\, e^{-K\,D_1}) - m_1'(\ddot{x}_1 - \ddot{y}\, e^{-K\,D_1}) + F_R &= m_1\ddot{x}_1 \\ W_2 - \rho g A_2(D_2 + x_2 - y\, e^{-K\,D_2}) - b_2(\dot{x}_2 - \dot{y}\, e^{-K\,D_2}) - m_2'(\ddot{x}_2 - \ddot{y}\, e^{-K\,D_2}) - F_R &= m_2\ddot{x}_2, \end{aligned} \quad (2.15)$$

where subscripts 1 and 2 denote the spar and follower buoys and the coupling force, F_R, represents the interaction between the two buoys.

2.3 Internal Transmission System

The internal transmission system includes those components which facilitate the transfer of the reaction force, F_R, from the point of coupling (i.e., where the rack-and-pinion make contact) to the generator input. The reaction force is opposed by inertial forces attributed to the accelerated mass of individual gears and shafts, damping forces caused primarily by velocity dependent bearing and gear friction, and the response torque of the generator subsystem. An illustration representing the transmission system is shown in Figure 2-5. By assuming a no-slip condition between all gears, the relative speed of buoy oscillations can be related to rotational speeds within the transmission system. Specifically, determination of the generator

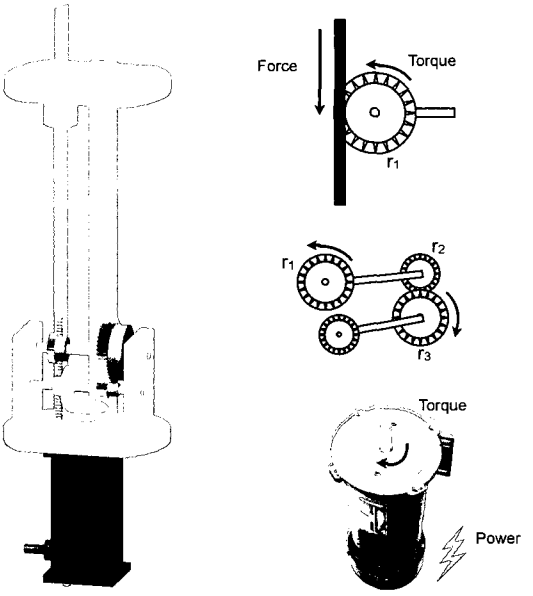

Figure 2-5: Internal WEC force transmission system.

shaft rotational speed can be determined by

$$\dot{\theta}_2 = (\dot{x}_1 - \dot{x}_2)\left(\frac{r_2}{r_3\, r_1}\right), \tag{2.16}$$

where $\dot{\theta}_2$ is the angular speed of the generator shaft, $\dot{x}_1$ and $\dot{x}_2$ are the heaving velocities of the spar and follower buoys, respectively, and r_1 through r_3 are the defining gear sizes.

Applying a Newtonian force balance to the transmission system produces the governing equation for the transmission system given by

$$T_1 = F_R\, r_1 = \underbrace{\left(J_1\frac{r_3}{r_2} + J_2\frac{r_2}{r_3}\right)}_{J_{eq}}\ddot{\theta}_2 + \underbrace{\left(b_1\frac{r_3}{r_2} + b_2\frac{r_2}{r_3}\right)}_{b_{eq}}\dot{\theta}_2 + T_{gen}\left(\frac{r_2}{r_3}\right), \tag{2.17}$$

where F_R is the coupling reaction force at the point of contact between spar and

follow buoy, T_1 is the torque delivered by the rack-and-pinion due to the coupling reaction force, T_{gen} is the response torque of the generator, and J_{eq} and b_{eq} represent the equivalent inertia and damping coefficients of the transmission system, accounting for the combined contributions from all components, as explained by Ogata (2004).

By substituting the no-slip equation (2.16) into the governing equation (2.17), the dependence of rotational speed of the generator shaft can be replaced with that of the heave velocity and acceleration of the spar and follower buoys

$$F_R\, r_1 = \Big(J_{eq}(\ddot{x}_1 - \ddot{x}_2) + b_{eq}(\dot{x}_1 - \dot{x}_2)\Big)\left(\frac{r_2}{r_3\, r_1}\right) + T_{gen}\left(\frac{r_2}{r_3}\right). \tag{2.18}$$

2.4 Permanent Magnet DC Generator

As the torque generated by the relative buoy motion is transfered to the PM DC generator, mechanical energy is converted to electrical energy. This conversion processes is governed by the electro-mechanical properties of the generator and can be represented with the equivalent circuit diagram in Figure 2-6, as shown by Guru and Hiziroğlu (2001). Performing a force balance on the system shows that the input torque transfered to the generator, T_{gen}, is opposed by velocity-dependent friction and windage damping, acceleration dependent inertial force, and the back electro-motor force (e.m.f.) which is linearly dependent on the current generated. A representative equation describing these dynamics follows

$$J_{gen}\frac{d^2}{dt^2}(\theta_2) = T_{gen} - b_{gen}\frac{d}{dt}(\theta_2) - K_t i, \tag{2.19}$$

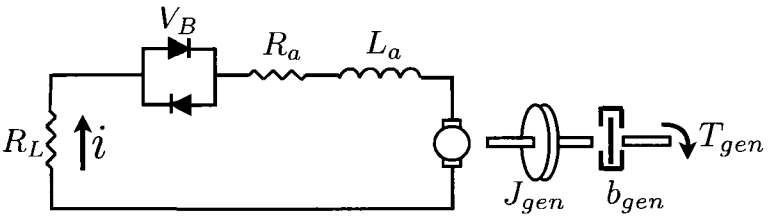

Figure 2-6: Equivalent circuit for the PM DC generator.

where i is the current produced by the generator, J_{gen} is the inertia associated with the generator's stator and shaft, b_{gen} is the velocity dependent damping coefficient, and K_t is the torque constant of the generator.

The conversion from mechanical energy to electricity is primarily dependent on the rotational velocity of the generator. By applying Kirchhoff's laws and equating the sum of the electrical potential difference around a closed circuit loop to zero, the electro-mechanical system can be represented as

$$L_a \frac{d}{dt}(i) = K_e \frac{d}{dt}(\theta_2) - R_a i - R_L i - V_B, \tag{2.20}$$

where L_a is the inductance, K_e is the back e.m.f. constant, R_a is the wire resistance in the armature, R_L is the resistive load applied across the generator terminals, and V_B is the voltage drop across the brushes (Kenjo and Nagamori, 1985). Combined, equations 2.19 and 2.20 describe the dynamic response of the PM DC generator.

2.5 MATLAB/Simulink Implementation

The governing equations describing each individual subsystem are reproduced in Simulink®, a computer program that provides an environment for multi-domain

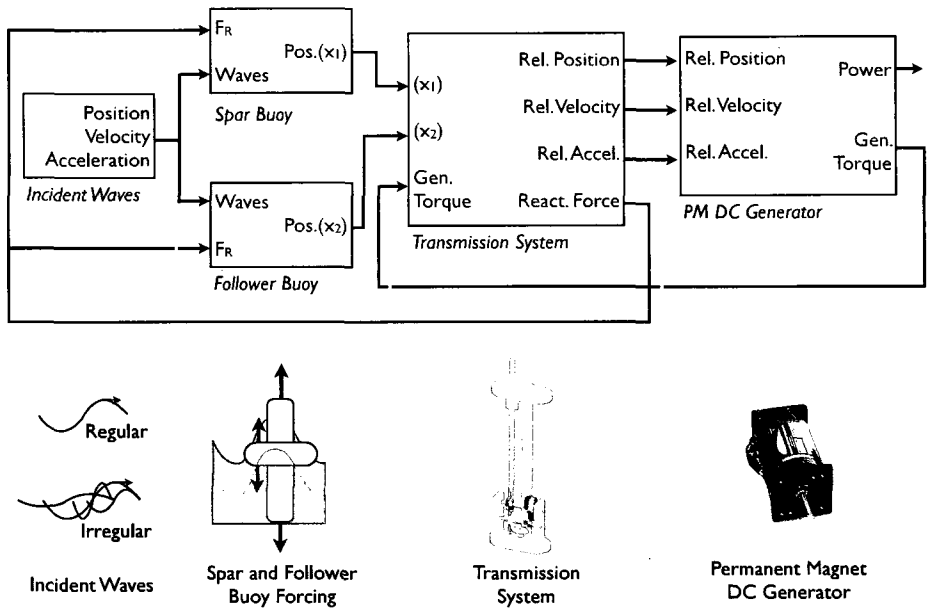

Figure 2-7: Overview of Simulink WEC subsystems.

simulation and model-based design for dynamic and embedded systems. Equations are represented graphically as combinations of functional blocks which act to perform operations on dependent variables. The flexibility alloted to this working environment allows efficient design, simulation, implementation, and testing of a variety of time-varying systems.

By implementing the governing equations in a modular fashion, such that they represent separate physical subsystems, a model may be produced with the inherent flexibility to be modified by substituting other subsystem modules. As illustrated in Figure 2-7, the WEC system being studied is divided into four major subsystems: Incident Waves, Spar and Follower Buoys, Transmission System, and the PM DC Generator. Each of these WEC system components are developed as individual modules in the following sections.

2.5.1 Incident Waves Simulink Block

The incident waves are responsible for the forcing applied to both the spar and follower buoys. As illustrated in wave forcing of a single buoy, equation 2.14, the wave surface level, vertical surface velocity, and vertical surface acceleration are required to solve for the buoy forcing. Generation of these values depends on the type of wave environment to be analyzed. Both regular waves, of single amplitude and frequency, and irregular waves, consisting of a random assortment of waves with multiple amplitudes and frequencies based on the Brentscheider Spectrum, are investigated.

Regular Waves

Regular waves are implemented by generating a sinusoidal surface level defined by a wave amplitude and period. The velocity and acceleration of this surface level are produced by taking its first and second derivative with respect to time as shown in equations 2.7-2.9. Simultaneous generation of surface level, velocity, and acceleration are combined into a single output and passed out of the Regular Waves block, as illustrated by the Simulink block diagram in Figure 2-8.

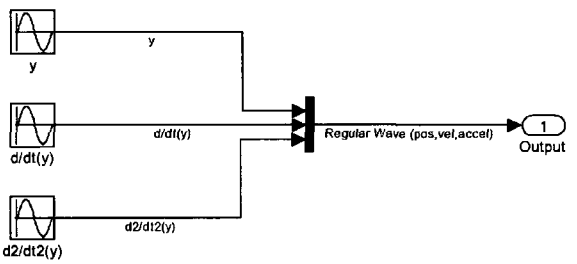

Figure 2-8: Simulink Block: Regular Waves

Irregular Waves

Irregular waves representing a realistic sea state are created by generating a water surface level time series based on the Bretschneider Spectrum. The desired significant wave height and modal period are input into the spectral Equation 2.13, and spectral density values are generated for a large range of equally spaced frequencies, thus representing a variety of waves found in a real sea. For each frequency, a sinusoidal function can be generated that includes an amplitude, dependent upon that particular frequency, and a random phase. The probability of occurrence of each wave with a particular amplitude (based on the spectral value at its frequency) is then used to generate a time series for the surface elevation. The algorithm used to create this synthetic data series can be referenced in the MATLAB code section of the appendix.

The time series for the surface is numerically differentiated twice to determine both the velocity and acceleration of the surface level. During simulation, Simulink uses a variable timestep and therefore performs a two-dimensional interpolation to generate required position, velocity, and acceleration values which are passed out of the Irregular Sea Waves block as shown in Figure 2-9. An example of a time series surface elevation, velocity, and acceleration output are shown in Figure 2-10.

2.5.2 Spar and Follower Buoy Simulink Blocks

Both the Spar and Follower Buoy Simulink blocks are representations of equations 2.15, which describe the response of each buoy to an incident wave. Surface level, velocity, and acceleration of the incident wave are inputs to each block, as

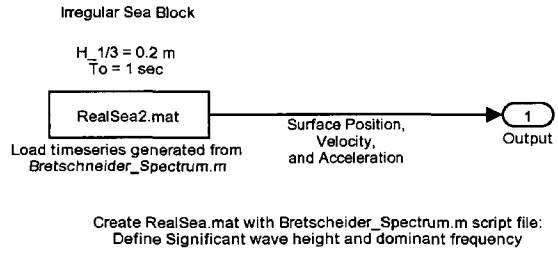

Figure 2-9: Simulink Block: Irregular Waves

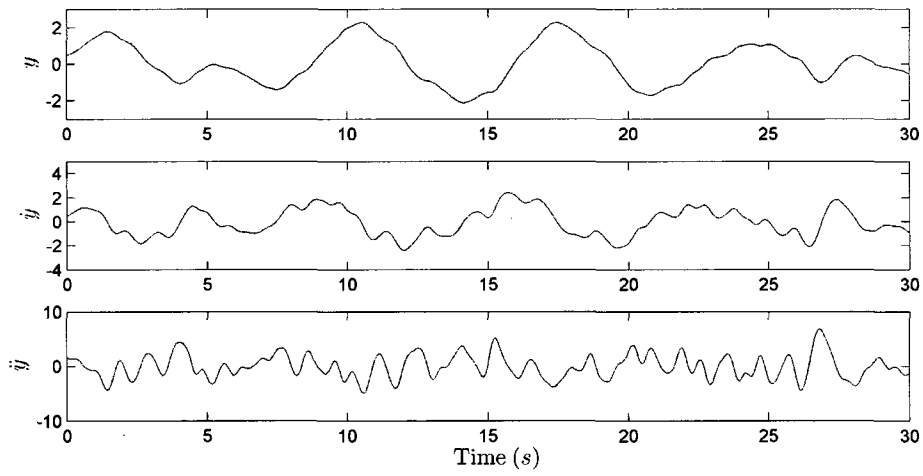

Figure 2-10: Irregular Waves block output signals: Surface (y), Velocity ($\dot{y}$), and Acceleration ($\ddot{y}$)

well as the feedback reaction force from the transmission (i.e., the coupling between buoys). The output of the Spar and Follower Buoy blocks are the vertical positions of each buoy.

As described previously (see section 2.2), the pressure forces acting on each buoy are a function of the buoy's vertical position and the instantaneous wave surface level: the damping forces are a function of the relative velocity of each buoy and vertical velocity of the incident wave; the inertial effect of each buoy's added mass is a function of the relative acceleration of each buoy and vertical acceleration of

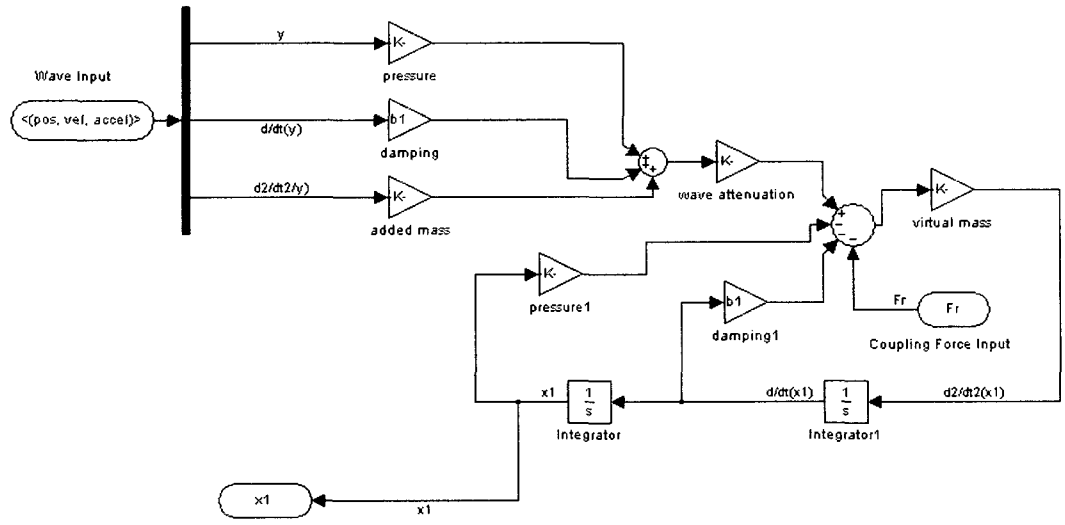

Figure 2-11: Simulink Block: Spar and Follower Buoy

the incident wave.

An illustration of the the Spar and Follower buoy Simulink block is shown in Figure 2-11, where the unique parameters of each buoy are identified as:

A : Cross-sectional area of buoy

D : Draft of buoy in still water

m : Mass of buoy

b : Hydrodynamic damping coefficient

m' : Hydrodynamic added mass

2.5.3 Transmission Simulink Block

As the physical transmission is coupled to the PM DC generator and both the Spar and Follower buoys, so are the input and output junctions of the Transmission Simulink block. The position of both Spar and Follower buoys are input values into

the Transmission block in addition to the response torque of the generator. The Transmission block output provides the rotational position, rotational velocity, and rotational acceleration of the generator drive shaft along with the buoy coupling reaction force. An illustration of the Transmission Simulink block is shown in Figure 2-12.

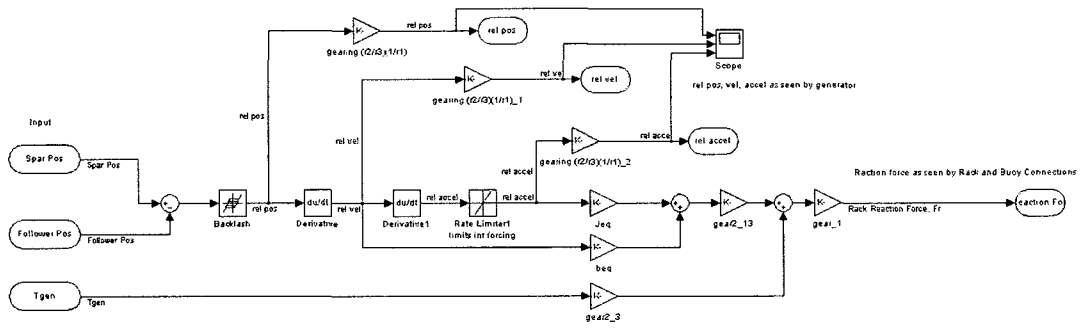

Figure 2-12: Simulink Block: Transmission

As defined by the governing equation (Eq. 2.18), the forcing developed by the equivalent damping is a function of the rotational velocity of the generator shaft, while the equivalent inertial forcing dependents on the rotational acceleration of that shaft. Accordingly, the rotational position of the generator shaft is determined by taking the difference in vertical Spar and Follower buoy positions and multiplying by a gearing ratio. Two subsequent derivatives of the positional differences between the buoys are taken and again multiplied by gearing ratios to provide the rotational velocity and rotational acceleration of the generator drive shaft.

Backlash within the gear system, which can cause a sudden impact of force due to discontinuities in contact between gears, is accounted for by including a native functional block within Simulink that implements a static amount of play. Mathematically, the Simulink backlash block returns a zero output when the rate

of change of the input, u, is within the defined lower and upper bounds

$$f(u) = \begin{cases} \textit{Output} & & \textit{Criteria} \\ u - u_{upper} & for & u \geq u_{upper} \\ 0 & for & u_{lower} < u < u_{upper} \\ u - u_{lower} & for & u \leq u_{upper}. \end{cases} \tag{2.21}$$

Lastly, the Transmission block outputs the reaction force values, F_R, utilizing the response of the PM DC Generator block.

A summary of the parameters used to define the transmissions characteristics follows:

r_1, r_2, r_3 : Internal gearing sizes

J_{eq} : Equivalent inertia as defined by Equation 2.17

b_{eq} : Equivalent damping as defined by Equation 2.17

Backlash : *Play* throughout transmission as defined by Equation 2.21

2.5.4 Permanent Magnet DC Generator Simulink Block

The PM DC Generator Simulink block represents Equations 2.19 - 2.20 and is responsible for coupling to the transmission by accepting input drive shaft rotational velocity and acceleration. The feedback provided by the PM DC generator is the output torque created by the generators operation which opposes the driving forces. This torque includes not only the back-e.m.f. forces generated, but also damping and inertial forces associated with its operation. Additionally, the electrical power

generated using a static resistive load is provided as an output. Figure 2-13 shows the block representation of the system.

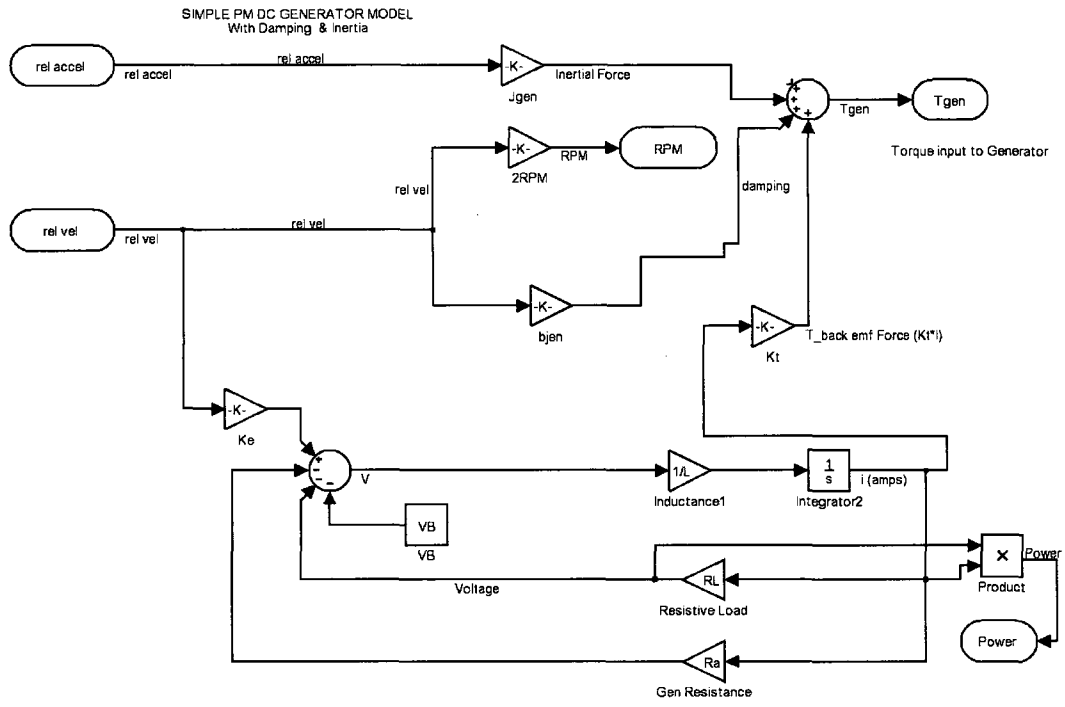

Figure 2-13: Simulink Block: PM DC Generator

The following lists the characteristic parameters which are used to define the generators operation:

K_t : Torque constant

K_e : Back e.m.f. constant

L_a : Inductance

R_a : Wire resistance in armature

R_L : Resistive load applied to generator terminals

V_B : Voltage drop across brushes

J_{gen} : Inertia associated with shaft and rotor

b_{gen} : damping coefficient

2.5.5 Complete WEC System Simulink Block

The combination of all subsystem Simulink blocks yields the complete WEC system Simulink model. Each subsystem block has a set of input and output variables that coincide with the physical interactions of that component with another subsystem. When fully assembled, the Simulink WEC system model is able to implement a wave action driving force and predict the systems response in the form of forces, position, and energy generation throughout the model. The block diagram in Figure 2-14 depicts the complete Simulink WEC system.

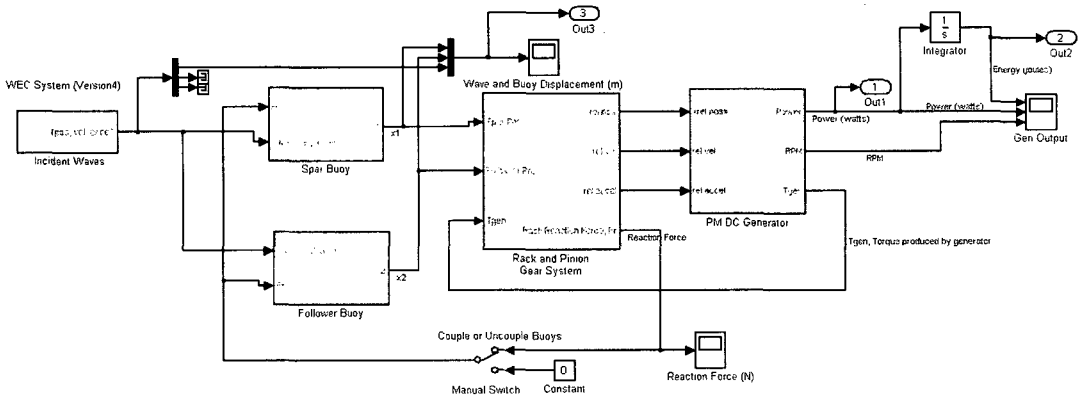

Figure 2-14: Simulink Block: Complete WEC System

2.5.6 Simulink/MATLAB Solver

The Simulink model is simulated by computing the states of all functional blocks at successive time steps. The model analyzed in this research utilizes Simulink's *ode45* solver, based on the Dormand-Prince pair, an explicit Runga-Kutta formula. This is a one-step solver, that is, it requires only the state values for the immediately preceding time point to solve for the next time step. Additionally, the solving

method uses a variable time-step size, thereby increasing accuracy during rapid changes in the model's states. This is a common method to maintain a specified level of accuracy for models with changing or piecewise continuous states.

CHAPTER 3

Characterization of Experimental Parameters

3.1 Overview

Several characteristic properties of components within the prototype WEC system require quantification in order to be applied to the Simulink model. To quantify these critical values, tests were performed on the prototype system in a manner that allowed measurement of the critical values, either directly or indirectly. The specific parameters investigated relate to the PM DC generator's mechanical and electro-mechanical operation, the transmission's mechanical properties, and the hydrodynamic properties of both the spar and follower buoys. An explanation of each of the characterization procedures as well as their results are presented in this chapter.

3.2 PM DC Generator Characterization

In order to produce an analytical model that can accurately predict the performance of a particular permanent magnet DC generator, the physical properties of that generator must be known. Referring to the equivalent-circuit diagram for the generator shown in Figure 2-6, the parameters required to define the operation of the generator are as follows:

J_{gen} = Inertia associated with generator rotation

b_{gen} = Frictional bearing and windage damping

K_t = Torque constant

R_a = Armature wire resistance

V_B = Voltage drop across brushes

L_a = Inductance

Each of the above parameters are characterized by either a static or a dynamic bench-top experiment as outlined by Kenjo and Nagamori (1985). The basis of these experiments lie in the ability to represent each experiment with an equivalent circuit for which unknown parameters may be solved for from measured values. Each of the characterization experiments are performed by reversing the operation of the generator and running it as a motor. This allows for a simple representation of the system and measurement of the necessary data required to determine the unknown parameters with minimal equipment.

3.2.1 Measurement of Static Generator Characteristics

The required data for the determination of the static parameters of the generator are obtained from two types of tests: a *no-load* test in which the motor shaft rotates freely and *lock-load* test in which the shaft is fixed in position. The experimental setup for these tests are depicted in Figure 3-1, where two different circuits are used depending on the type of measurement required. Circuit (a) is used for the *no-load* test since the impedance seen by the motor far exceeds the impedance of the ammeter during rotation, hence the voltage drop across the ammeter is negligible.

Circuit (b) is used for the *lock-load* test because the motor impedance is much smaller than the impedance of the ammeter when rotational speed is zero.

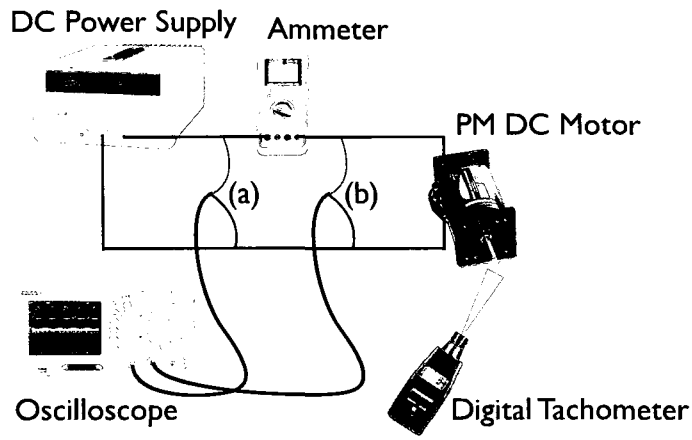

Figure 3-1: Experimental setup for measuring parameters during: (a) no-load test, (b) lock-load test

The equivalent circuit representation for the depicted static parameter experimental setup is shown in Figure 3-2, where V is the applied voltage, I_a is the current running through the system, V_B is the voltage drop across the brushes, R_a is the resistance due to the copper wire wound armature, R_h represents resistance due to losses including bearing friction, windage, and iron losses (including eddy-current hysteresis loss), and R_L represents the resistance of a load applied to the motor. When a lock-load is applied to the motor, the load resistance is equal to zero. Solving the equivalent circuit using this assumption leads to

$$R_L = 0 \tag{3.1}$$

$$V = V_B + I_a R_a.$$

Therefore, by measuring the current, I_a, at varied input voltages, V, a linear rela-

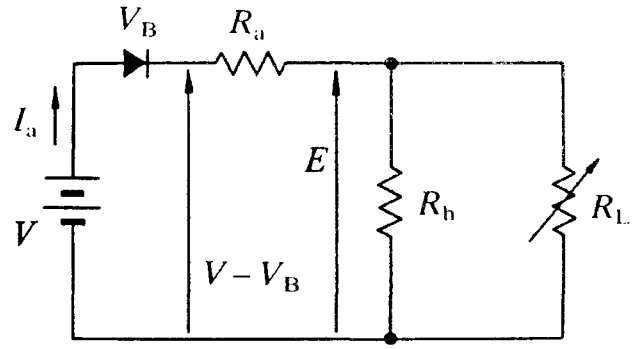

Figure 3-2: Equivalent circuit for PM DC motor static parameter analysis.

tionship is discovered which allows for the determination of V_B (y-intercept) and R_a (slope) as shown in Figure 3-3.

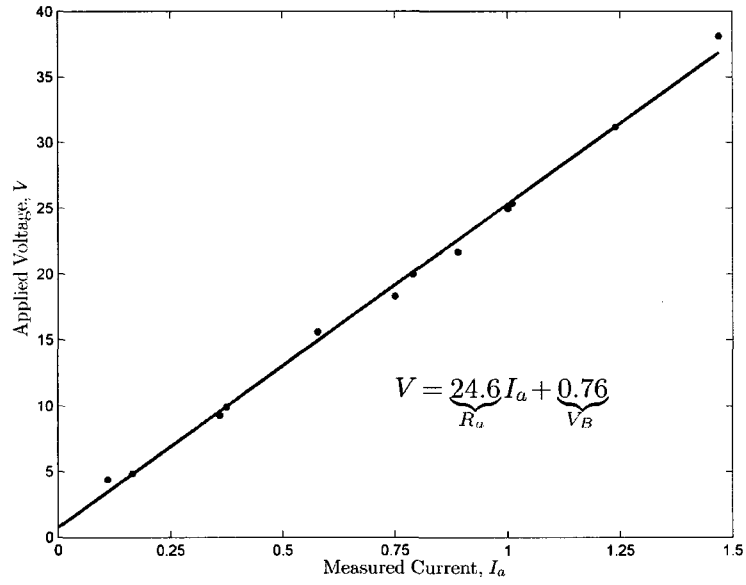

Figure 3-3: Results from lock-load test with V_B and R_a shown.

Releasing the lock and allowing the motor to rotate freely with no load applied results in an infinite value for R_L shown in the equivalent circuit, which leads to

the solution:

$$R_L = \infty$$

$$V = V_B + I_a \left(R_a + R_h\right). \tag{3.2}$$

Equation 3.2 may then be arranged to obtain R_h:

$$R_h = \left(\frac{V - V_B}{I_a}\right) - R_a \tag{3.3}$$

Values for the voltage drop across the brushes, V_B, and the armature resistance, R_a, may be substituted into Equation 3.3 allowing for determination of R_h values for a variety of input voltages, V. Measuring the voltage input into the motor, V, the current supplied, I_a, and the rotational speed of the motor, ω, enables the determination of the motor constant, K, as illustrated in Figure 3-4.

The motor constant defines the linear relationship between the applied voltage and resulting rotational speed, therefore the losses associated with R_h may be calculated and a relationship developed for its response to rotational speed as shown in Figure 3-5.

The resistance, R_h, may be transitioned from the equivalent circuit analysis to the physical damping coefficient that it represents, shown in Figure 2-6, with knowledge of the motor constant:

$$b_{gen} = \frac{K^2}{R_h} \tag{3.4}$$

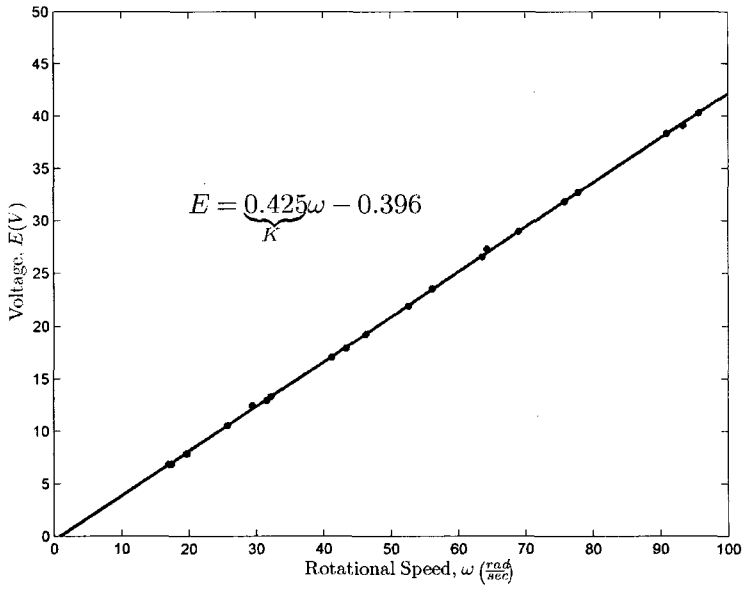

Figure 3-4: Results from no-load test. Motor constant, K, shown.

Calculating the damping coefficient, b_{gen}, for the range of tested rotational speeds allows for a direct correlation to the torque generated by this damping, $T_{damp} = b_{gen} \times \omega$. Performing a linear fit to the data allows extraction of the slope of the curve equal to b_{gen}, shown in Figure 3-6.

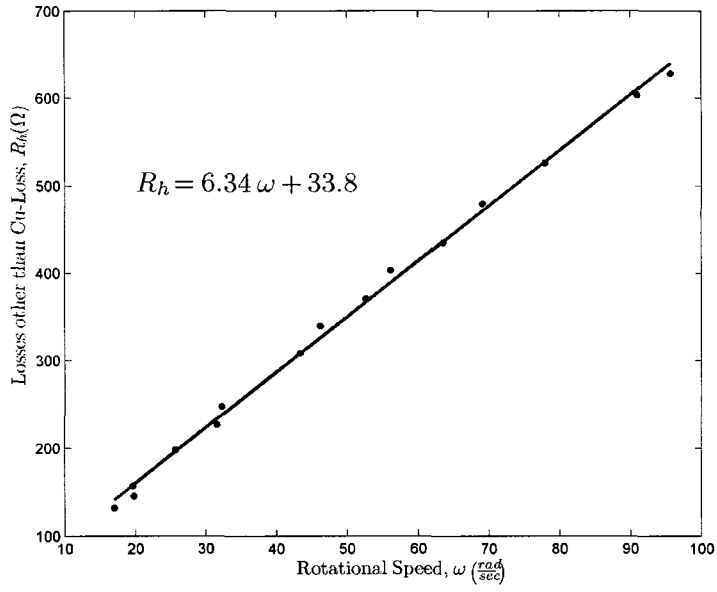

Figure 3-5: Non-Cu losses, R_h, results for no-load generator characterization test.

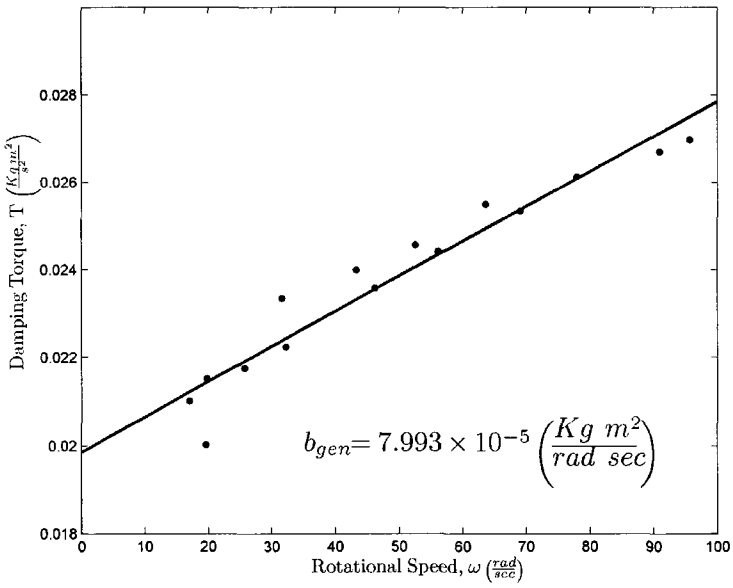

Figure 3-6: Damping Coefficient, b_{gen}, results from no-load generator characterization test.

3.2.2 Measurement of Dynamic Generator Characteristics

The parameters related to the dynamic generator characteristics include the mechanical time constant, τ_m, the electrical time constant, τ_e, and the inertia associated with rotation, J_{gen}. The mechanical time constant describes the delay in rotational response of a motor to the applied voltage and is defined as the time required for the rotational speed to achieve about 63% of its final value when a step input voltage is applied. Similarly, the electrical time constant is described as the delay in current response of a motor to the applied voltage and is defined as the time required to achieve about 63% of the steady-state current drawn by a fixed-shaft motor when a step voltage is applied.

Using the approach developed by Page (1981), the equivalent circuit that describes the generator while characterizing dynamic parameters is shown in Figure 3-7. The armature current after switch S is closed can be derived from transient theory, and is given by

$$i_a = \frac{V}{R_a + R_D} + \frac{V\,R_D}{R_a(R_a + R_D)} \frac{\tau_m}{(\tau_m - \tau_e)} e^{-t/\tau_m} - \frac{V}{R_a}\left(1 + \frac{\tau_e}{(\tau_m - \tau_e)} \frac{R_D}{R_a + R_D}\right) e^{-t/\tau_e}. \tag{3.5}$$

If $\tau_m \gg \tau_e$, Equation 3.5 reduces to

$$i_a = \frac{V}{R_a + R_D} + \frac{V\,R_D}{R_a(R_a + R_D)} e^{-t/\tau_m} - \frac{V}{R_a} e^{-t/\tau_e}. \tag{3.6}$$

The implications of Equation 3.6 are:

1. At $t = 0$, the armature current is zero.

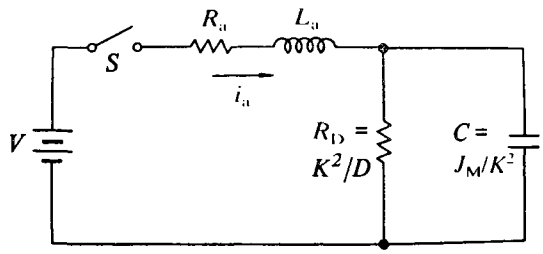

Figure 3-7: Equivalent circuit for PM DC motor dynamic parameter characteristics.

2. After the application of voltage, the current increases exponentially. Therefore, for time $t < \tau_e$

$$e^{-t/\tau_m} \simeq 1.$$

Equation 3.6 may then be approximated by

$$i_a \simeq \frac{V}{R_a}\left(1 - e^{-t/\tau_e}\right). \tag{3.7}$$

Equation 3.7, in this case, describes the current rise while the motor shaft is locked, and therefore will be used to acquire the electrical time constant.

3. For the time range $5\tau_e < t < 5\tau_m$,

$$e^{-t/\tau_e} \simeq 0.$$

Substitution of this into Equation 3.6, yields

$$i_a = \frac{V}{R_a + R_D} + \frac{R_D\, V}{R_a(R_a + R_D)} e^{-t/\tau_m}. \tag{3.8}$$

Additionally, because $R_D \gg Ra$, further simplification can be made as

$$i_a \simeq \frac{V}{R_D} + \frac{V}{R_a} e^{-t/\tau_m}. \tag{3.9}$$

Using Equation 3.9, it is then possible to solve for the mechanical time constant.

The experimental setup for measuring the generator's electrical time constant, mechanical time constant, and rotational inertia is shown in Figure 3-8. A DC power supply provides constant voltage, initialized with a switch. Voltage is monitored across the motor and a resistor, R_s, is used to measure values for the supplied voltage and current. Using the step application of applied voltage as a trigger, the transient response of two voltages are then captured with an oscilloscope. The

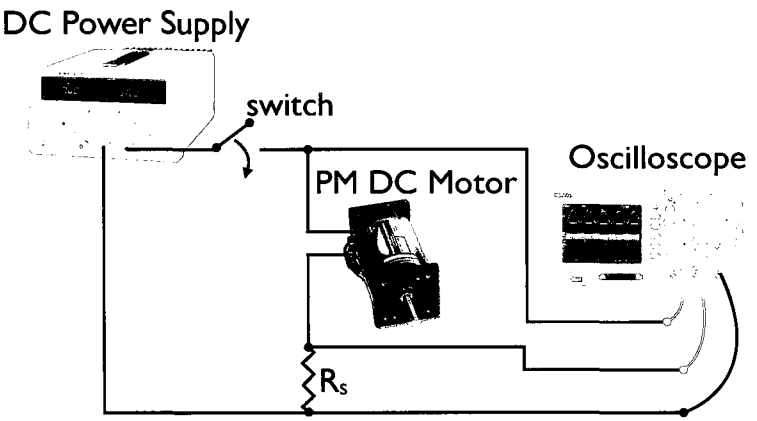

Figure 3-8: Experimental setup for measurement of dynamic generator characteristics.

resulting response for both the lock-load and no-load characterization tests are depicted in Figures 3-9 and 3-10. Calculations of the electrical time constant, mechanical time constant, and inertia are described below.

As illustrated in Figure 3-9, the lock-load stationary current is $0.955A$ when a voltage of $24.89V$ is applied. The time to required to reach 63.2% of the stationary current is $2.8ms$. Compensating for the resistance, $R_s = 1\Omega$, the electrical time constant is calculated to be

$$\tau_e = (2.80\ ms)\frac{R_a + R_s}{R_a} = 2.92\ ms. \tag{3.10}$$

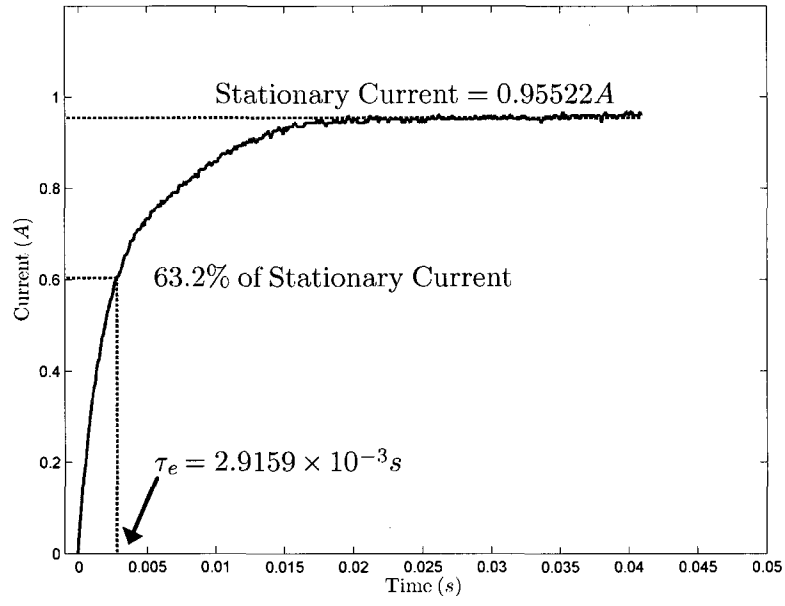

Figure 3-9: Determination of the electrical time constant, τ_e, from lock-load dynamic characterization test with $24.89V$ applied.

The no-load test is preformed with an applied voltage of $24.14V$. The resulting stationary current is measured at $I_{steady} = 59.17mA$, while the lock-load current is determined to be $I = V/(R_a + R_s) = .9595A$. The resistance R_D is then calculated

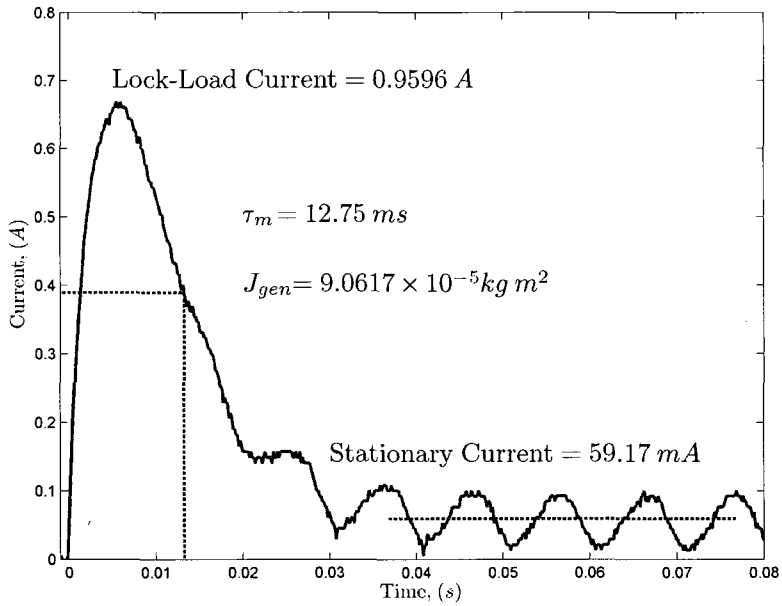

Figure 3-10: Determination of the generator mechanical time constant and inertia, (τ_m *and* J_{gen}), from no-load dynamic characterization test with $24.1395V$ applied.

as

$$R_D = \left(\frac{V}{I}\right) - (R_a + R_s) = 382.7\Omega. \tag{3.11}$$

The current at t=τ_m is calculated from Equation 3.6 as

$$i_a = V\left(\frac{1}{R_a + R_D} + \frac{R_D}{R_a(R_a + R_D}e^{-1}\right) \tag{3.12}$$

where substitutions for $e^{-t/\tau_e} \rightarrow 0$ and $e^{-t/\tau_m} \rightarrow e^{-1}$ have been made.

Determining the ratio,γ, of i_a to the lock-load current yields

$$\gamma = \frac{R_a}{R_a + R_D} + \frac{R_D}{R_a + R_D}e^{-1} = 38.8\%, \tag{3.13}$$

where 38.8% of the lock-load current is $0.372A$. Referring to the captured data in

Figure 3-10, it takes $13.2ms$ for the current to reach $0.372A$. To compensate for the resistance, R_s, τ_m is calculated as

$$\tau_m = 13.2\ ms \times \frac{R_a}{R_a + R_s} = 12.75\ ms. \tag{3.14}$$

Utilizing the mechanical time constant, the moment of inertia is calculated as

$$J_{gen} = \frac{\tau_m\ K^2}{R_a} = 9.062 \times 10^{-5}\ kg\ m^2 \tag{3.15}$$

3.3 Transmission System Characterization

Characterization of the transmission system is performed to determine the damping contribution to the system in much the same way as the PM DC Generator. Referring to the experimental setup in Figure 3-1, the transmission is driven by the generator (operating as motor) while measurements are made using setup (a). The equivalent circuit used to represent the system is the same as that shown in Figure 3-2. The principal difference compared to the generator characterization is the addition of frictional damping to the system, which is accounted for in the resistance term, R_h.

By driving the generator-transmission system with a range of input voltages and measuring that input voltage, V, the armature current, I_a, and the steady-state rotational speed, ω, a relationship is developed that allows determination of the resistance, R_h. Using Equation 3.4, and the earlier determined value of the motor constant, the damping coefficient as a function of rotational speed is determined.

As illustrated in Figure 3-11, the resulting damping coefficient is the sum of both generator and transmission effects. Therefore, the damping associated with only the transmission my be deduced by subtraction:

$$b_{trans} = b_{gen+trans} - b_{gen} \tag{3.16}$$

$$b_{trans} = .02 + (0.0236)10^{-7.68\frac{1}{\omega}} - 7.993 \times 10^{-5} \left(\frac{Kg\ m^2}{rad\ sec}\right)$$

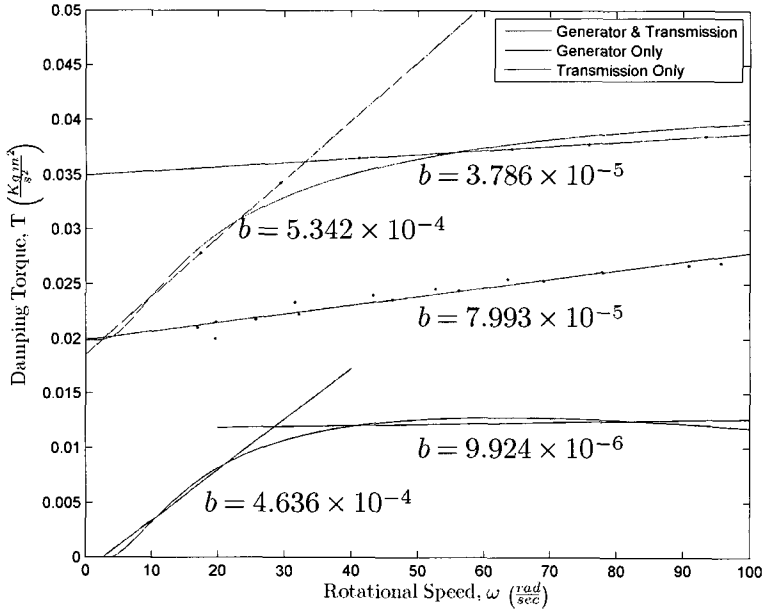

Figure 3-11: Damping parameter characterization of transmission.

The resulting transmission damping coefficient is best represented by a nonlinear function of the rotational speed

$$b_{trans} = (0.0236)\left(2.089 \times 10^{-8}\right)^{\frac{1}{\omega}} + .0199 \left(\frac{Kg\ m^2}{rad\ sec}\right) \tag{3.17}$$

3.4 Buoy Characterization

In order to describe the heave reaction of a buoy to incident wave forcing, as derived in Equation 2.14, several variables must be known. Of these, the hydrodynamic linear damping coefficient, b, and added mass, m', are readily determined experimentally. These parameters describe the viscous effects, inertia due to nearby water entrained in the buoys movement and the diffracted, radiated wave energy. Adhering to the methods presented by Berteaux (1976), these parameters are determined experimentally using the *free-release* testing method. This method consists of releasing a buoy, displaced from its still water-line, and measuring its damped heave response. Utilizing measurements of successive amplitudes and periods of oscillation, the damping coefficient and added mass are determined by employing vibration theory for a mass-spring system with damping.

The equation of motion for a single buoy heaving due to incident waves presented earlier (Equation 2.14) may be rewritten as

$$(\rho g A)\, x + b\dot{x} + (m + m')\ddot{x} = F_o \cos(\omega t + \sigma), \tag{3.18}$$

where F_o is the exciting force and σ is the phase angle between forcing and the incident wave:

$$F_o = re^{-kD}\sqrt{(c - m'\omega^2)^2 + b^2 + w^2} \tag{3.19}$$

$$\sigma = tan^{-1}\left(\frac{-b\omega}{c - m'\omega^2}\right) \tag{3.20}$$

Equation 3.18 can then be transformed into a form similar to that of a single degree

of freedom mass-spring system with linear damping:

$$\ddot{x} + 2n\dot{x} + p^2 x = \frac{F_o}{m + m'} cos(\omega t + \sigma), \tag{3.21}$$

where p is defined as the angular frequency of oscillation without damping and n is a convenient simplification given by

$$p^2 = \frac{\rho g A}{m + m'} \tag{3.22}$$

$$2n = \frac{b}{m + m'}. \tag{3.23}$$

For a buoy not forced by waves, but rather put into motion by either lifting up or pushing down and releasing, $F_o = 0$ and equation 3.21 reduces to

$$\ddot{x} + 2n\dot{x} + p^2 x = 0. \tag{3.24}$$

The solution to the resulting heave motion is

$$x = e^{-nt} \left(C_1 sin\sqrt{p^2 - n^2}\, t + C_2 cos\sqrt{p^2 - n^2}\, t \right), \tag{3.25}$$

where C_1 and C_2, the constants of integration, are determined from initial conditions. From this, the damped period of free oscillation is determined to be

$$T_d = \frac{2\pi}{\sqrt{p^2 - n^2}}. \tag{3.26}$$

Using the solution in Equation 3.25 and a positional transient response for a

free oscillating buoy, measurements can be made to determine successive amplitudes and the damped period of oscillation. Because the transient heave response of the buoy results in a logarithmic decay in oscillation amplitude (illustrated in Figure 3-12), the linear damping coefficient and added mass are determined by sequentially solving for each of the following parameters:

$$n = \frac{1}{T_d} ln \frac{A_i}{A_{i+1}} \tag{3.27}$$

$$p = \sqrt{\left(\frac{2\pi}{T_d}\right)^2 + n^2} \tag{3.28}$$

$$m' = \frac{\rho g A}{p^2} - m \tag{3.29}$$

$$b = 2n\,(m + m') \tag{3.30}$$

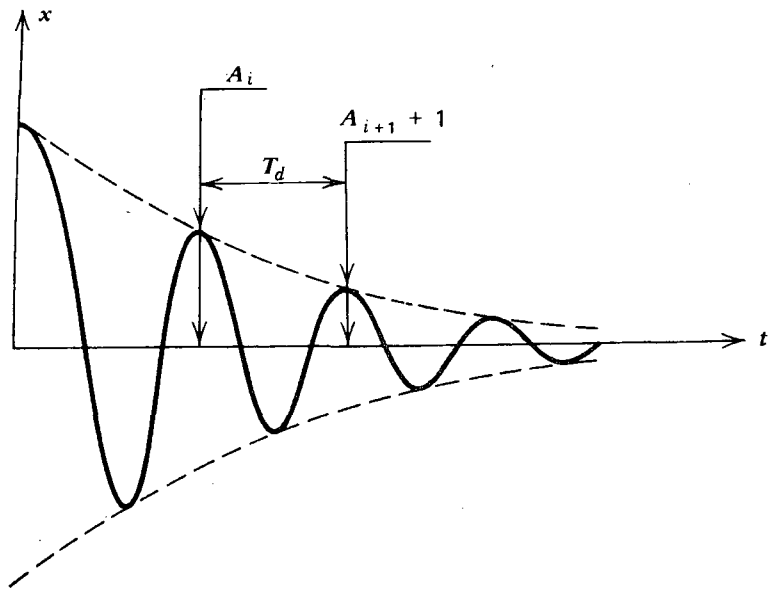

Figure 3-12: Transient response of an unforced buoy, released from an elevated position. (Berteaux, 1976)

3.4.1 Experimental Setup

The experimental free release tests were completed in the Jere A. Chase Ocean Engineering Laboratory wave tank facility located at the University of New Hampshire. This facility offers a viewing window along the wave tank for observations above and below the surface. High contrast markers, $1\,cm$ square in size, were placed on the buoys at a location that would remain above the surface during testing. The heave response of both spar and follower buoys were recorded using UNH's Optical Positioning Instrumentation and Evaluation (OPIE) equipment with customized image processing software (see Appendix). For each test, the buoy was raised above the still water surface level and released. The resulting motion was recorded and analyzed. An illustration of the experimental setup is shown in Figure 3-13

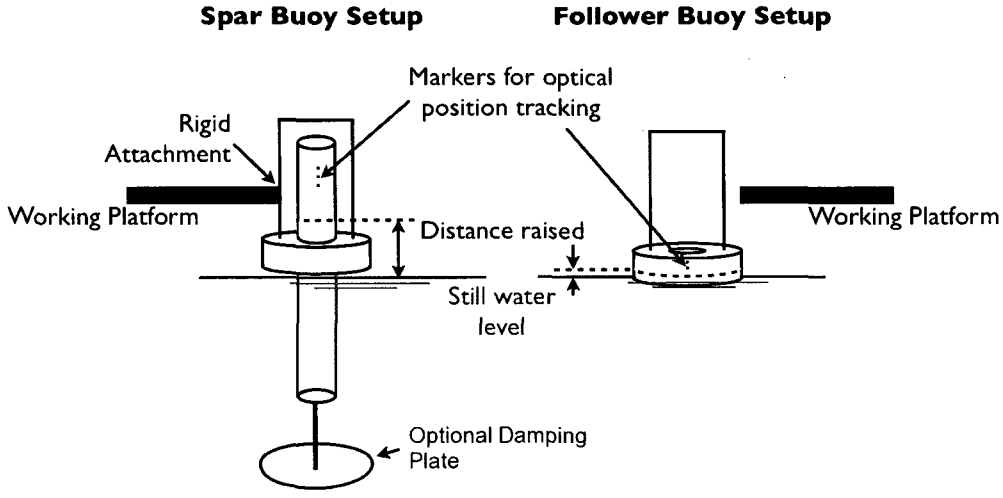

Figure 3-13: Experimental setup for the hydrodynamic characterization of the spar and follow buoys.

3.4.2 Spar Buoy Free Release Test

For the spar buoy free release tests, the spar was placed inside the follower buoy to prevent excessive pitching. The follower buoy was raised just above the surface level of the water and rigidly mounted to the wave tank carriage. The spar buoy was then raised to its drop height of about 10cm and released. Several heave responses of the spar buoy with and without the added damping plate are shown in Figure 3-14, with results for the damping coefficient and added mass tabulated in Table 3.1. For the configuration of the spar buoy without the damping plate attached, there is a large percent deviation for the calculated added mass. This deviation may be attributed to increased rolling resistance at the contact points between the spar and follower buoys (i.e., where the spar buoy is held concentric to the follower buoy by six rollers) due to surface defects which where irregularly contacted.

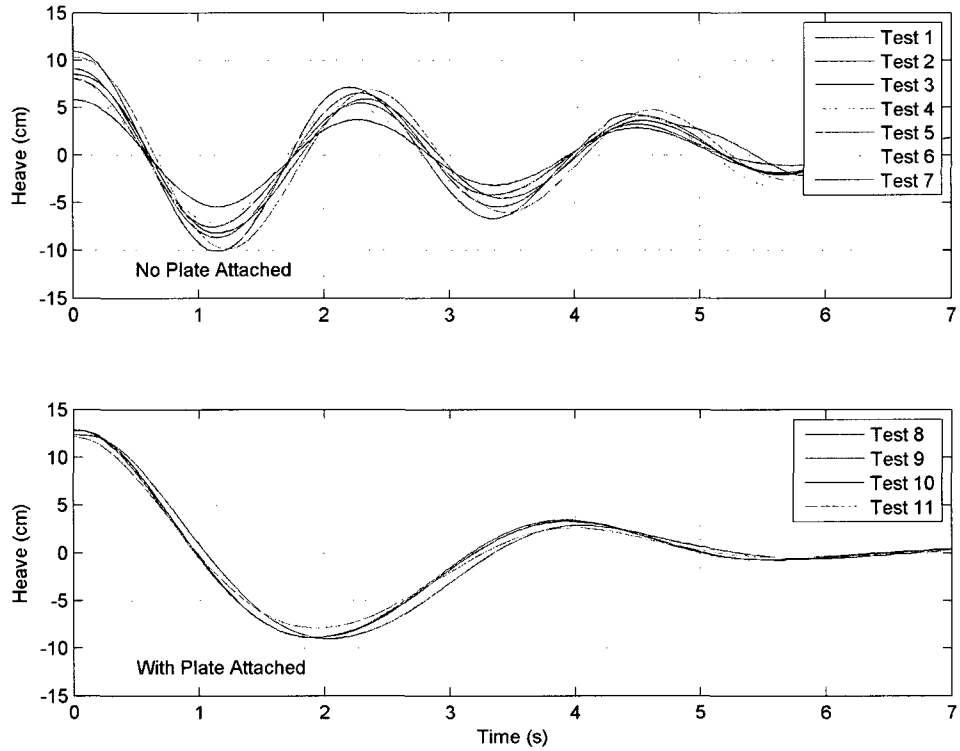

Figure 3-14: Heave response of the spar buoy during free release testing with (upper) and without (lower) the damping plate attached.

Table 3.1: Summary of spar buoy free release testing results.

Test No.	Plate Attached	Damping Coef., $b_1(\frac{kg}{s})$	Added Mass, $M_1'(kg)$	Mass, $M_1(kg)$
1	no	10.32	5.43	25.4
2	no	8.79	3.75	25.4
3	no	9.70	2.88	25.4
4	no	11.15	4.54	25.4
5	no	10.48	1.22	25.4
6	no	10.90	2.86	25.4
7	no	11.22	2.02	25.4
Mean	-	**10.37**	**3.24**	-
Standard Dev.	-	0.873	1.45	-
% Deviation	-	8.41	44.75	-
8	yes	55.74	51.73	28.6
9	yes	61.79	58.19	28.6
10	yes	52.31	47.93	28.6
11	yes	63.18	53.51	28.6
Mean	-	**58.23**	**52.84**	-
Standard Dev.	-	5.09	4.26	-
% Deviation	-	8.74	8.06	-

3.4.3 Follower Buoy Free Release Test

The follower buoy was tested without additional support to correct for pitching during its free heave motion. Additionally, because of the followers minimal draft, it was raised up to only about $2\,cm$ from the still water level and released. Both of these factors contributed to the limited amount of viable results and to the significant variation in the acceptable results. The heave response from several tests are shown in Figure 3-15, with results for the damping coefficient and added mass tabulated in Table 3.2.

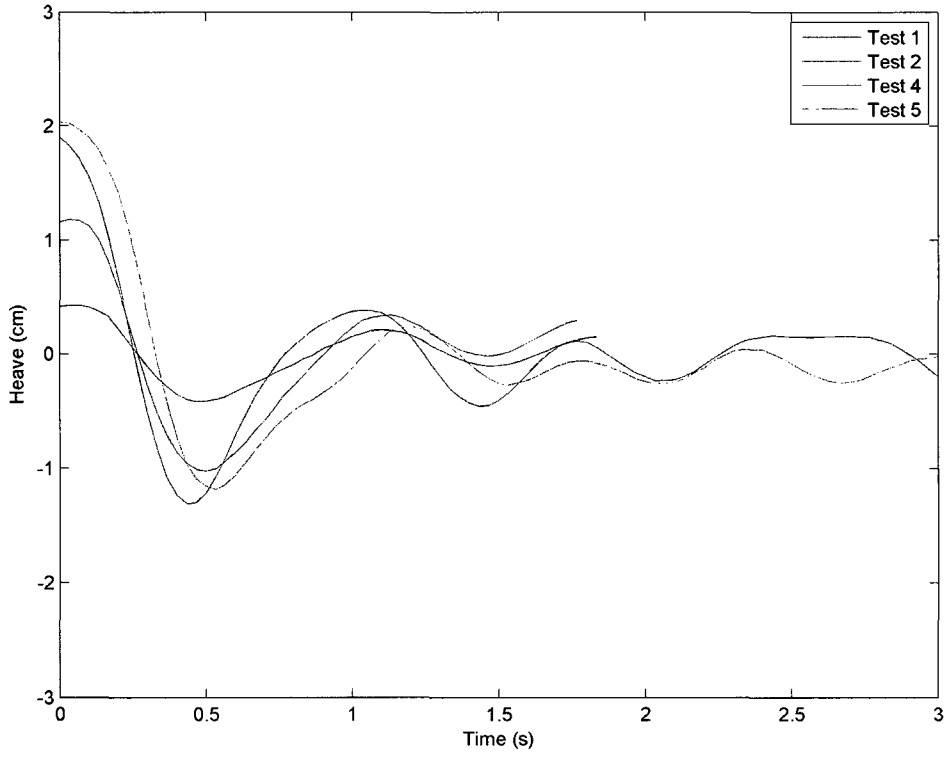

Figure 3-15: Heave response of the follower buoy during free release testing.

Table 3.2: Summary of follower buoy free release testing results.

Test No.	Damping Coefficient, $b_2(\frac{kg}{s})$	Added Mass, $M_2'(kg)$	Mass, $M_2(kg)$
1	169.5	77.37	9.3
2	212.7	77.60	9.3
3	216.6	83.41	9.3
4	252.1	64.59	9.3
5	275.0	70.98	9.3
Mean	**225.2**	**74.79**	-
Standard Dev.	40.42	7.20	-
% Deviation	17.95	9.63	-

CHAPTER 4

Experimental Validation of the WEC Model

4.1 Overview

In order to provide a thorough validation of the numerical WEC model, individual components of the system are experimentally evaluated under a range of operating conditions, and the results compared to numerical models of the same configuration. Validation of the mechanical system isolated from wave forcing, uncoupled spar and follower buoys in regular waves, and the coupled WEC system in regular and irregular waves are performed. An overview of each experimental setup is provided, along with important information regarding data acquisition. Typical results are presented and the analysis explained. A comparison is then made to numerical model predictions with the discussion of the validation results presented at the end of the chapter.

4.2 Mechanical System Validation

Validation of the WEC mechanical system is performed by utilizing a wave motion simulation device. This device allows the delivery of defined relative motion to

the coupled spar-follower buoys, isolating the transmission and generator components of the system from the incident wave forcing. In doing so, a direct comparison can be made between the measured experimental operation of the power take-off system and predictions by the numerical model of an identical system configuration.

4.2.1 Experimental Setup

The wave-like motion simulator is utilized to drive relative displacement between the spar and follower buoys. The buoys are coupled with the transmission and power generation system as they would be during normal operation. However, the WEC is oriented horizontally to avoid unbalanced gravitational forces opposing the drive motor, as would occur during vertical motions. The follower buoy is fixed to a large framework to prevent movement, while the spar buoy remains free to translate. A high-torque low-speed drive motor is connected via two lever arms to the bottom of the spar. The connection is such that rotational motion generated from the drive motor is converted to one-dimensinoal linear motion, driving the spar back and forth in a sinusoidal motion with an amplitude of $9.9\,cm$. The speed of the drive motor is controlled by maintaining a constant supply voltage during operation, resulting in an oscillation with a constant period. Relative movement of the buoys is obtained by optically tracking the position of markers on the spar buoy using UNH's OPIE system. An oscilloscope is used to monitor power generation by recording voltage at 1000Hz across load resistors attached to the generator. By varying the drive speed of the motor and load resistance, data is acquired that represents a range of operating conditions. Figure 4-1 illustrates the experimental

setup used.

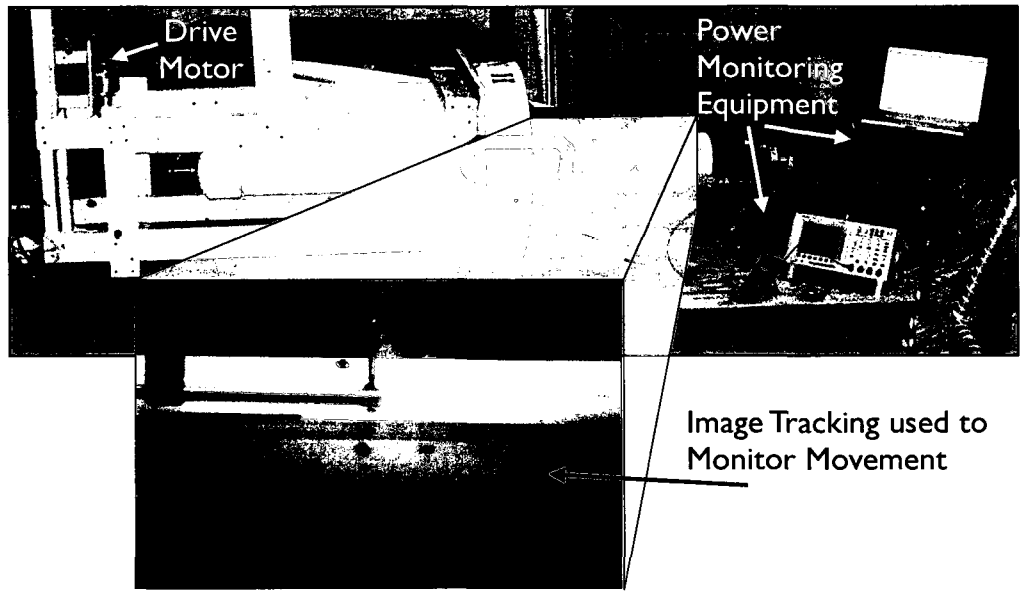

Figure 4-1: Experimental setup for the mechanical motion simulator.

4.2.2 Experimental Results

The spar buoy's relative horizontal displacement is analyzed and its excursion compared to a sinusoidal function, as shown in figure 4-2. The relative position data is then numerically differentiated to obtain the relative velocity of the buoy heave, which, as described by equation 2.16, is directly proportional to the generator's rotational velocity. As the positional and power generation data are acquired with independent hardware, the outputs are time-synchronized by aligning the peak power generation with the peak rotational velocity. The time-synchronized results provide a depiction of the device's operation which then yields a starting place for comparison to numerical results. An illustration of representative time-synchronized results for a single experimental run is shown in Figure 4-3.

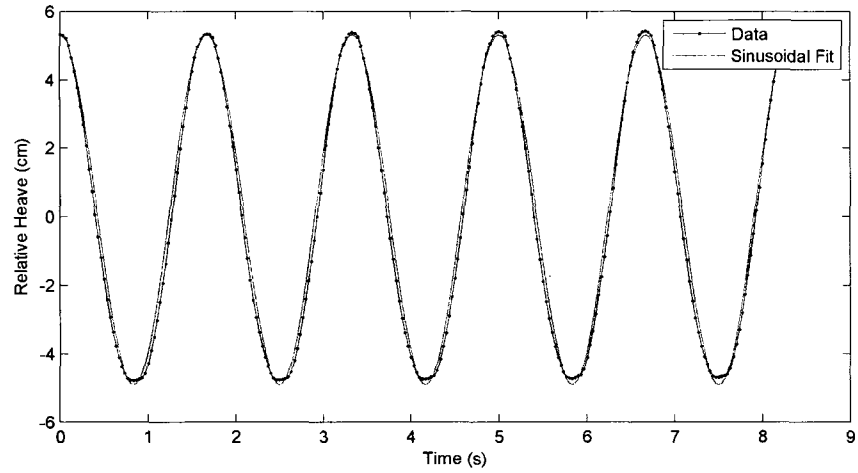

Figure 4-2: Measured experimental excursion during motion simulation tests and the analytical fit to that motion, which is used in the comparative numerical model.

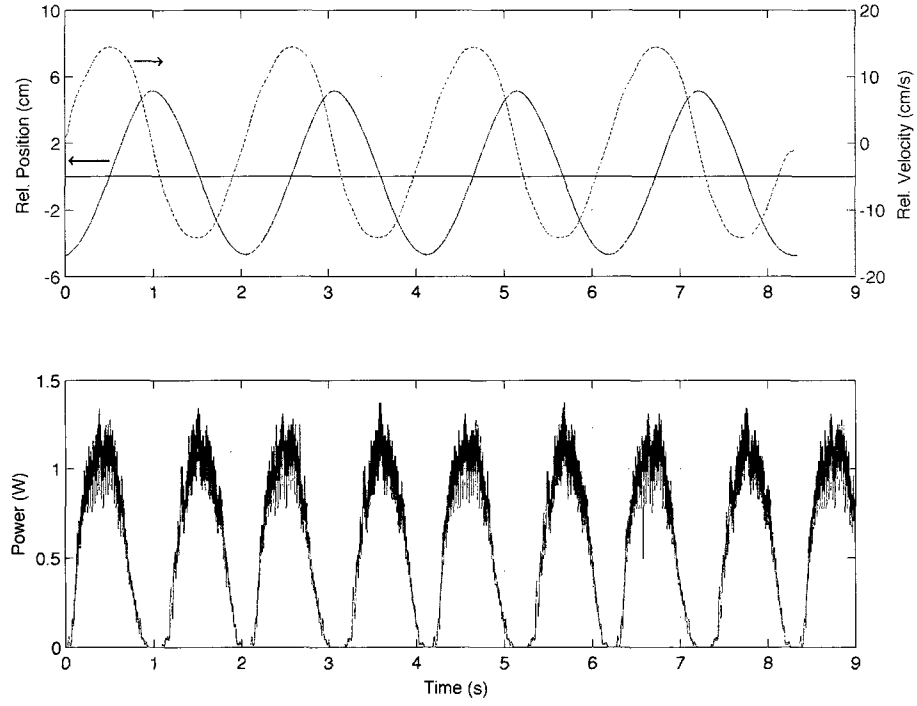

Figure 4-3: Time synchronized experimentally measured position, velocity (upper), and power generation (lower) using motion simulator.

4.2.3 Comparison to Computer Simulations

For each test the experimentally measured values for the period, relative oscilla-

tion amplitude, and resistive load are applied to the numerical model. Adjustments are made to the numerical model to prevent follower buoy motion, so as to drive the relative motion between the spar and follower with the determined sinusoidal function. A comparison between the experimentally-obtained power generation and the prediction is made by plotting the transient response of both, as shown in the lower plot in Figure 4-4. Values for the average power generation are obtained by numerically integrating the power generation over the alloted time. A summary of these results for a range of controlled relative motions are presented in Table 4.1. Plots for the transient response for each of the tabulated values is available in the Appendix for reference.

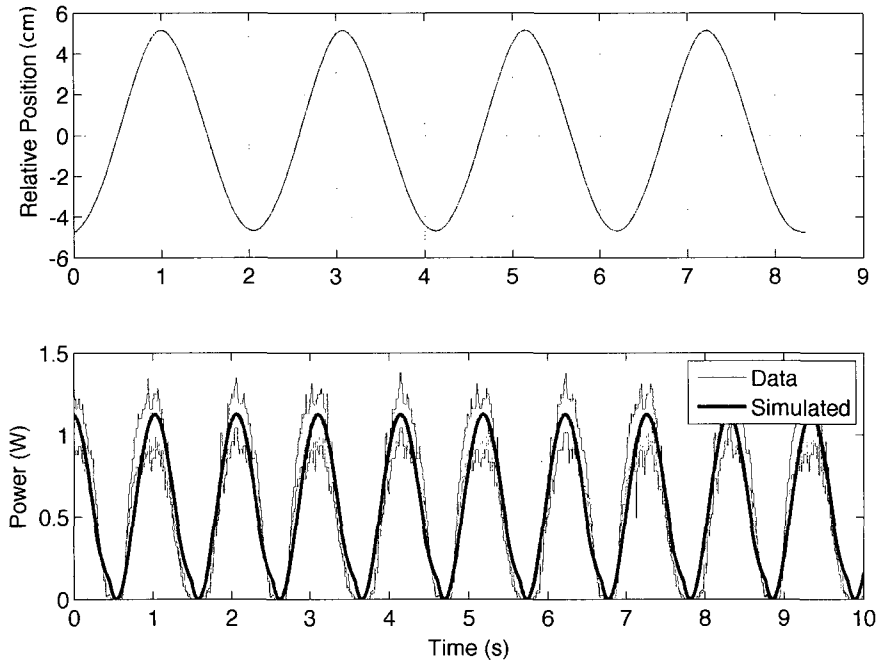

Figure 4-4: Experimental motion simulator results compared to predicted response.

Table 4.1: Comparison of experimental and predicted power generation of the isolated power take-off system.

$T\ (s)$	$R_L\ (\Omega)$	Avg. Power in $Watts$		$\%\ Error$
		Measured	Predicted	
1.87	1.1	.359	.378	5.29
2.08	1.1	.294	.299	1.70
2.59	1.1	.185	.192	3.78
3.90	1.1	.076	.078	2.63
1.83	2.2	.688	.717	4.22
2.08	2.2	.518	.549	5.98
2.67	2.2	.297	.325	9.43
3.22	2.2	.204	.212	3.92
3.93	2.2	.131	.142	8.40

4.3 Uncoupled Buoys in Regular Waves

To isolate and evaluate the numerical model's ability to accurately predict the forcing and positional response of the spar and follower buoys, wave tank testing is performed with the uncoupled WEC system. This testing allows both the spar and follower buoys to independently react to the wave forcing without the added effects of the transmission and generator coupling. As such, by tracking the positional response of each buoy in a variety of regular incident waves, a comparison to the numerical model's predicted response may be made.

4.3.1 Experimental Setup

The physical WEC system testing was performed in the Jere A. Chase Ocean Engineering Laboratory wave tank facility located at the University of New Hampshire. The wave tank is 36.5 m long, 3.05 m wide, and 2.44 m deep. It is a hydraulic-driven paddle design, capable of generating both monochromatic and random waves

that terminate at the opposite end when interacting with a passive beach. Along the length of the tank there is a viewing window which allows for observation above and below the water surface. At this location in the tank the WEC system was deployed and compliantly tethered during testing to allow optical position tracking. An illustration of the wave tank setup is shown in Figure 4-5.

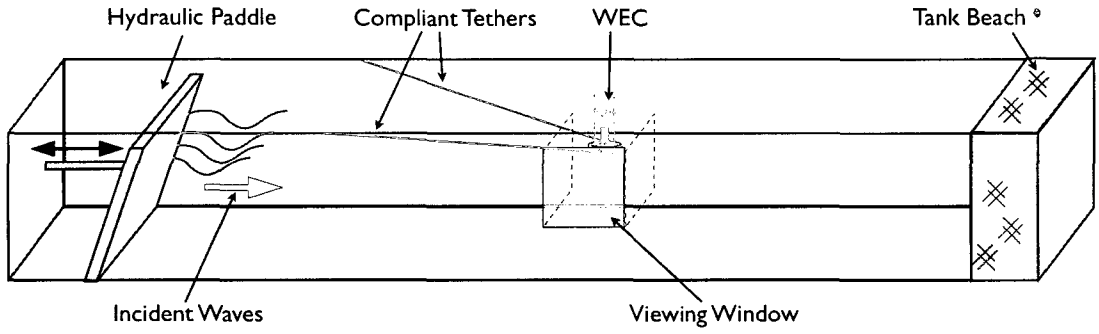

Figure 4-5: Overview of the wave tank testing setup.

During startup, the waves were initiated and allowed to reach steady-state. The WEC was allowed to drift, due to wave action at the surface, into a position in front of the wave tank view window. To maintain the WEC in the window area, long elastic tethers were attached to both sides of the follower buoy and anchored to the sides of the wave tank.

Measurement Systems

Measurements of the wave height were obtained using a wave staff, which has a resistance linearly proportional to its submerged length. The wave staff was calibrated by recording the voltage across the staff at several static submerged positions. The depth and corresponding voltage values were then linearly fit to

obtain the *calibration factor*, defined by

$$Voltage = (Calibration\ Factor) \times (Submerged\ Depth) - Offset. \tag{4.1}$$

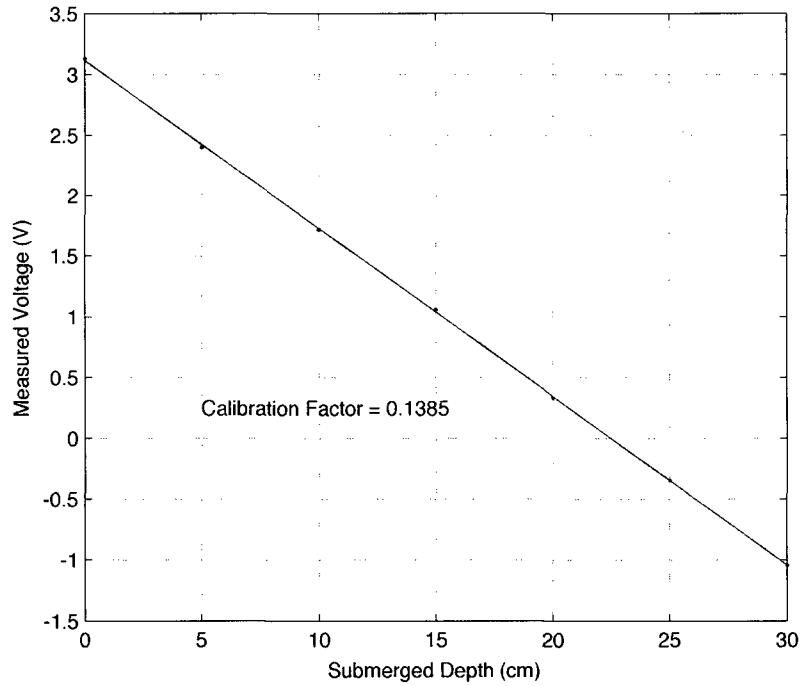

Figure 4-6: Calibration measurement used to correlate measured voltage to staff's submerged depth.

During testing, the wave staff was deployed about $1\,m$ away from the WEC on the beachward side. It was also offset to one side of the WEC, so as to not be significantly influenced by any surface wake from the WEC. An example surface profile measured using the wave staff is shown in figure 4-7, while a photograph of the experimental setup in the wave tank is shown in figure 4-8.

Positional tracking of both the spar and follower buoys was implemented using UNH's OPIE system, capable of providing planar tracking of markers positioned

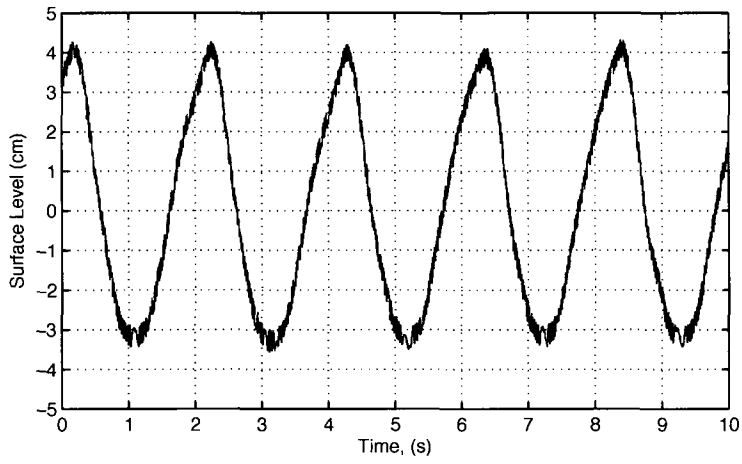

Figure 4-7: Calibrated surface profile of incident waves measured with the wave staff.

on both buoys at 30 frames per second. The OPIE camera system was positioned so as to capture movement through the wave tank viewing window, as shown in figure 4-9.

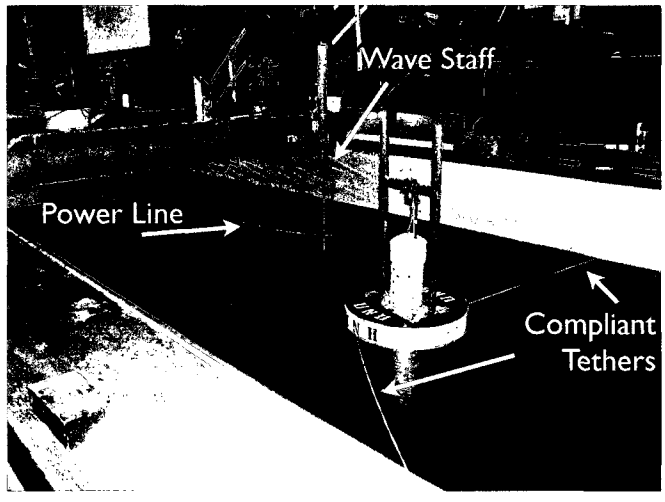

Figure 4-8: Photograph of the physical WEC deployed in the wave tank.

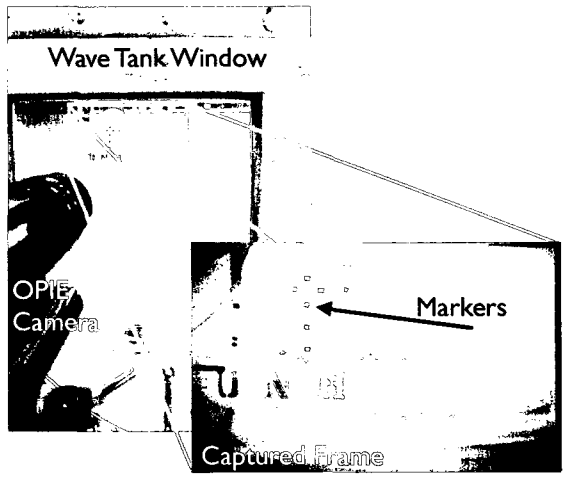

Figure 4-9: Photograph of the view through the wave tank window and corresponding OPIE imagery.

4.3.2 Experimental Results

The response of the uncoupled spar and follower buoys in regular waves was recorded in four different sea states, with and without the additional damping plate attached to the spar buoy. The raw transient heave response was adjusted by subtracting its mean value from all date points to provide oscillation about a zero reference. The difference in the spar and follower buoy position was taken as the relative position of the buoys, with its derivative equal to that of the relative velocity of both buoys. A typical analysis depicting the above manipulations is shown in figure 4-10.

For each applied sea state, the heave response of both spar and follower buoys can be characterized by dividing each buoy's heave amplitude by that of the incident wave. Defined as the heave response amplitude operator (RAO),

$$RAO = \left(\frac{Buoy\ Heave\ Amplitude}{Incident\ Wave\ Amplitude} \right), \tag{4.2}$$

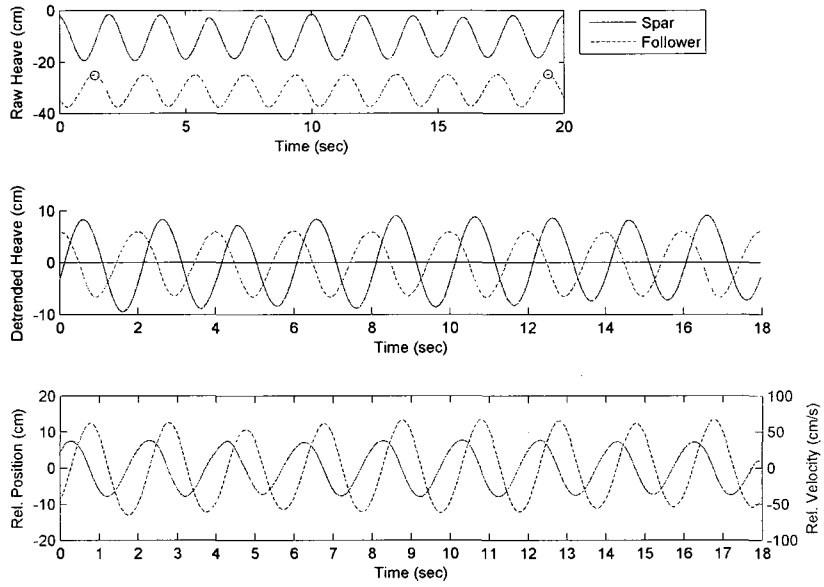

Figure 4-10: Position data acquired with OPIE system.

this value may be used to quantitatively compare the response of the uncoupled buoys. A summary of the RAO's for the examined sea states is given in Table 4.2.

Table 4.2: Experimental RAO values for the uncoupled response of spar and follower buoys in regular waves.

T (s)	H (cm)	Attached Plate	Spar Excursion (cm)	Spar RAO	Follower Excursion (cm)	Follower RAO
1.0	8	No	1.63	.204	7.46	.933
1.2	8	No	2.35	.294	8.27	1.03
1.5	10	No	6.59	.659	11.40	1.14
2.0	10	No	17.60	1.76	12.27	1.23
1.0	8	Yes	1.19	.149	7.86	.983
1.2	8	Yes	1.06	.133	7.25	.906
1.5	10	Yes	2.29	.229	11.21	1.12
2.0	10	Yes	1.95	.195	10.57	1.06

4.3.3 Comparison to Computer Simulations

The experimentally measured response of the uncouple spar and follower buoys in regular waves was compared to computer model simulations of similar forcing. In the computer model, the transmission and generator modules were removed and the spar and follower buoys were allowed to react independently to the incident wave forcing. The ensuing motion predicted by the computer model was recorded and compared to the experimental data as shown in figure 4-11. The measured follower buoy heave motion (upper plot in Figure 4-11) shows good agreement with the simulated prediction, while the measured spar buoy heave motion (lower plot) shows a slight phase lag and larger amplitude when compared to its simulated prediction.

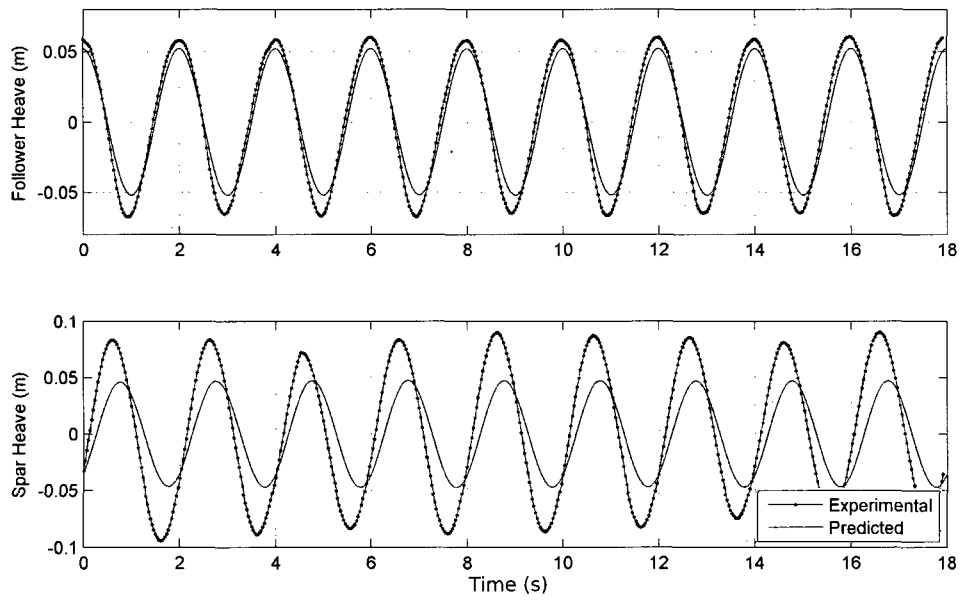

Figure 4-11: Comparison of experimental heave motion for uncoupled buoys in regular waves to simulated predictions. Top plot shows the follower buoy response and the bottom plot shows the spar buoy response.

Taking the difference of spar and follower buoy heave positions results in their

relative displacement. By then taking the derivative of the relative displacement with respect to time, the relative velocity of the buoys can also be obtained, as shown in Figure 4-12. Examination of the relative heave between spar and follower buoys (upper plot) shows a slight phase and amplitude difference between the measured and predicted values, which is then carried through to the relative velocity (lower plot). Differences in measured and predicted values are likely due to the computer model's utilization of vertical-only linear wave theory to determine forcing, which does not account for the pitching or surging motions that can occur.

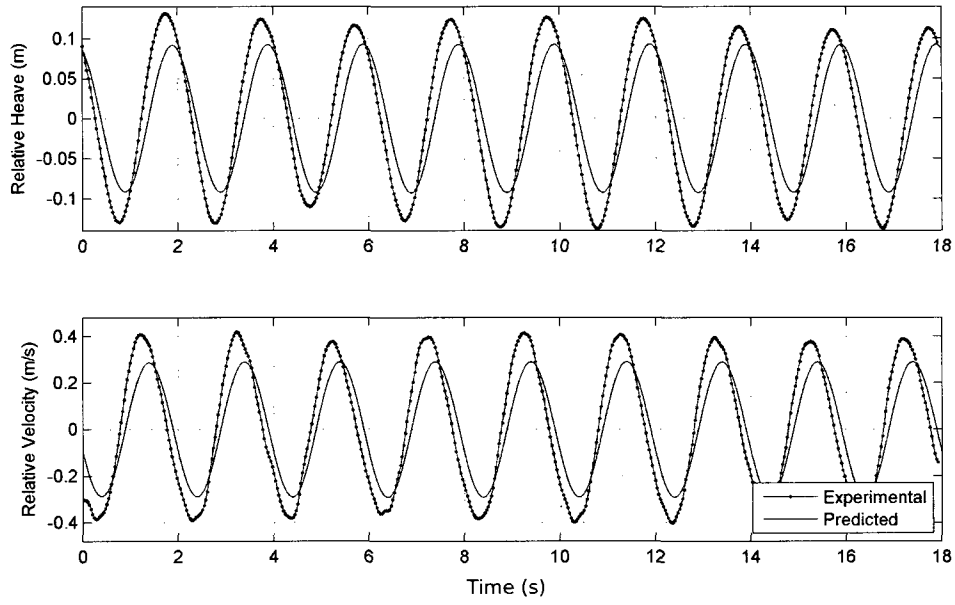

Figure 4-12: Comparison of experimental relative heave and velocity for uncoupled buoys in regular waves to simulated predictions.

The comparison plots detailing all the experimental versus predicted transient responses for the uncoupled WEC configuration are available in the appendix for further examination.

The results are quantified in Table 4.3 by extracting the average relative heave

amplitude divided by the incident wave height, which yields the RAO as shown by Equation 4.2. The measured RAO's are compared to predicted values obtained from computer simulations and the percent error is listed.

Table 4.3: Summary of experimental and predicted heave response for both spar and follower buoys in regular waves.

T (s)	H (cm)	Plate	Spar RAO	% Error	Follower RAO	% Error
1.0	8	No	**.204**/.002	99.0	**.933**/.955	2.4
1.2	8	No	**.294**/.012	95.9	**1.03**/1.098	6.8
1.5	10	No	**.659**/.097	85.3	**1.14**/1.082	5.3
2.0	10	No	**1.76**/.834	52.6	**1.23**/1.040	15.4
1.0	8	Yes	**.149**/.007	95.3	**.983**/.952	3.2
1.2	8	Yes	**.133**/.027	79.7	**.906**/1.097	21.4
1.5	10	Yes	**.229**/.085	62.9	**1.12**/1.082	3.6
2.0	10	Yes	**.195**/.198	1.5	**1.06**/1.040	1.9

(**Measured** / Predicted)

4.4 Coupled WEC System in Regular and Irregular Waves

The complete WEC system, including spar and follower buoys coupled via the transmission system to the generator, was experimentally evaluated in both regular and irregular waves. Evaluation of the WEC system in regular waves allows for direct comparison (after the system has reached a steady operation) to the computer models predictions of buoy motions and power generation. Utilizing the experimental WEC system response, the accuracy and validity of the model, as exposed to regular waves, can be quantified.

The response of WEC systems to real sea states composed of irregular waves is typically much different then their response to regular, constant frequency and amplitude, waves. Therefore, to accurately gauge the performance of WEC systems they must also be evaluated in irregular sea-states similar to those where full-scale systems will be eventually deployed. For the northeastern United States, typical sea states may be represented using the Bretschneider Spectrum (Equation 2.13) described earlier.

For both regular and irregular waves, the WEC system was experimentally evaluated in a range of sea-states in wave tank tests. During each test, the surface level, WEC motion, and power generation were recorded. The experimental data was then compared to numerical predictions for an identical configuration.

4.4.1 Experimental Setup

The experimental setup used for the coupled WEC system was similar to that of the uncoupled buoy setup explained in the previous section and illustrated in figures 4-5, 4-8, and 4-9. Additionally, a resistive power bank was utilized to both measure and dissipate the power generated by the WEC during each test. The resistive bank consisted of a number of power resistors, configured in series and parallel to provide a total resistance that ranged from 1 to 500 Ohms. The voltage across the resistive load was monitored and recorded using LabVIEW software with a National Instruments data acquisition card sampling at 500Hz. Utilizing Ohm's Law and knowledge of the resistive load being applied, the power generated by the

WEC was equal to

$$Power = Voltage \times Current = \frac{Voltage^2}{Resistance}.$$

For each given sea state, multiple load resistances were applied to the generator to examine the performance of the WEC under a variety of load conditions. The resulting WEC motion and power generation were recorded.

4.4.2 Experimental Results for Regular Waves

The motion response of the WEC was captured optically by recording the positions of both spar and follower buoys. The mean position for each buoy was then subtracted from each data set to show the heave relative to each buoys still water level, as explained previously and shown in figure 4-10. The time derivative of the difference in spar and follower positional data was also calculated as it provides the relative velocity of the two buoys. The power generation data was then combined with that of the positional response of the WEC to provide a comprehensive understanding of the devices operation, as shown in figure 4-13.

For each unique test with the controlled parameters of incident wave period, T, wave height, H, and resistive load, R_L, characteristic performance value were recorded and are listed in Table 4.4.

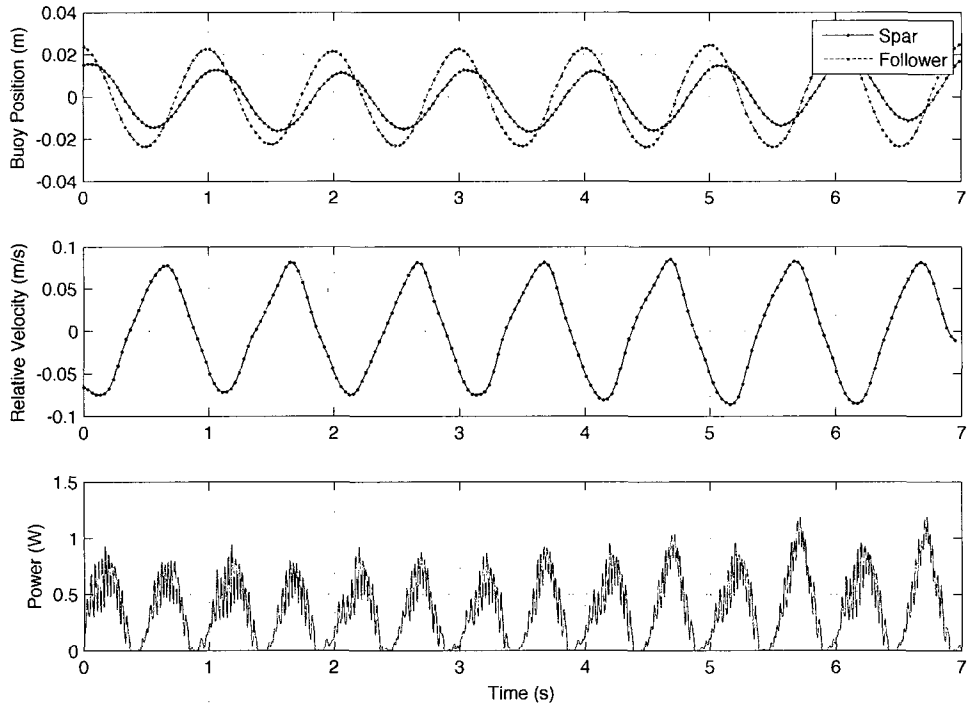

Figure 4-13: Analyzed motion and power generation for WEC system in regular waves. Buoy's position (top), relative velocity (middle), power (bottom) as a function of time.

Table 4.4: Summary of experimental data collection from the coupled WEC System in regular waves.

Control Variables				Rel. Heave	Max. Rel.	Max.Power	Avg.Power
$T\ (s)$	$H\ (cm)$	$R_L(\Omega)$	Plate	Amp.(cm)	Velocity$(\frac{cm}{s})$	(W)	(W)
1.0	8.0	50	No	1.60	4.72	.799	.212
1.0	8.0	300	No	2.22	10.6	1.85	.329
1.2	8.0	50	No	2.20	6.39	.627	.152
1.2	8.0	100	No	2.36	7.76	.774	.235
1.2	8.0	300	No	2.76	10.7	.496	.159
1.2	8.0	500	No	4.04	12.0	.592	.189
1.2	10.0	50	No	2.57	8.20	1.84	.587
1.2	10.0	300	No	3.84	11.4	.496	.159
1.2	10.0	500	No	3.33	10.6	.968	.345
1.3	8.0	300	No	1.81	5.68	.203	.041
1.3	8.0	500	No	1.70	3.95	.113	.019
1.0	8.0	55	Yes	2.52	8.16	1.39	.376
1.0	8.0	400	Yes	4.88	15.7	1.11	.326
1.2	8.0	300	Yes	5.04	12.7	1.42	.451
1.2	10.0	300	Yes	6.34	16.4	2.02	.727
1.3	8.0	300	Yes	4.26	10.8	.891	.272
1.5	10.0	300	Yes	7.26	14.7	1.62	.469

4.4.3 Comparison to Computer Simulations in Regular Waves

Computer simulations were performed utilizing the same incident regular waves (defined by period and wave height) and resistive load applied to the generator. The resulting predicted WEC motion and power generation were then compared to the experimentally collected data in the time-domain. Figure 4-14 shows the time-synchronized experimental response of the WEC system overlaid with the computer model predicted response. For each comparative analysis, the individual buoy heave motion was isolated and compared (Figure 4-14 a-b). This allows determination of significant differences in amplitude and phase of each buoys heave response, compared to the predicted. Additionally, the relative motion of the buoys was also determined and plotted (Figure 4-14 c-d), thereby providing insight to the driving speed of the power take-off system. Finally, a comparison between the instantaneous power generated and the predicted is shown along with its integrated value (Figure 4-14 e-f), illustrating the cumulative energy generated over the test period.

The effect of a phase or amplitude differences in the buoy's heave motion to the predicted motion carries through to differences in relative motion and ultimately power generation. While the phase and amplitude difference may be small, their cumulative result is visible when the energy produced over time is compared (Figure 4-14 f). Plots depicting the complete collection of comparative responses for the WEC system over the range of evaluated regular waves can be found in the appendix. A comparison summarizing the experimentally measured performance values in regular waves to predictions using the computer model are shown in Table 4.5.

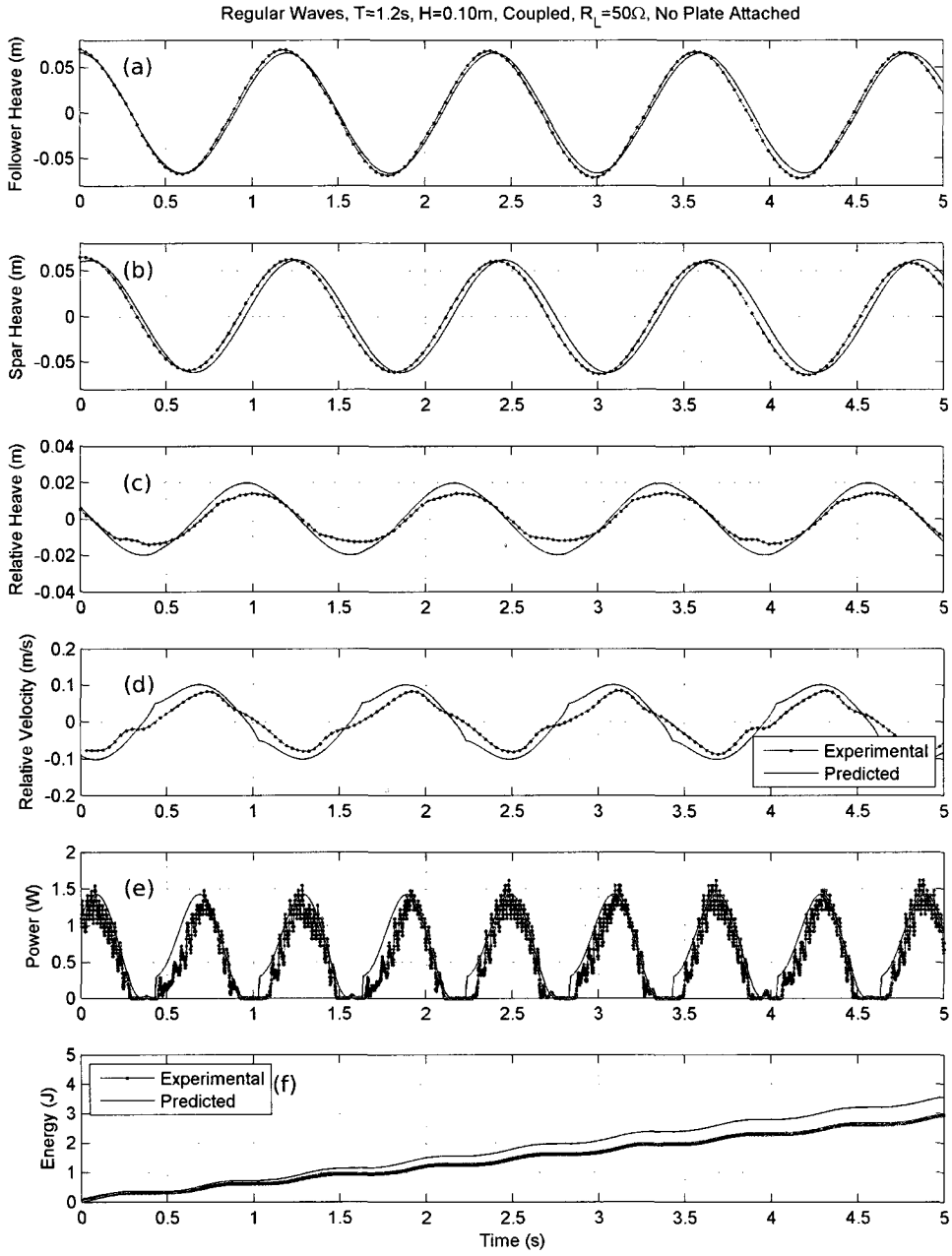

Figure 4-14: Comparison of experimental and predicted transient heave and power generation for WEC system in regular waves.

Table 4.5: Performance comparison of experimental WEC operation versus predicted in regular waves.

Control Variables				Rel. Heave	%	Avg.Power	%
T (s)	H (cm)	$R_L(\Omega)$	Plate	Amp.(cm)	Error	(W)	Error
1.0	8.0	50	No	**1.60**/2.05	28.1	**.212**/.237	11.8
1.0	8.0	300	No	**2.22**/3.35	50.9	**.329**/.230	30.1
1.2	8.0	50	No	**2.20**/2.44	10.9	**.152**/.234	53.9
1.2	8.0	100	No	**2.36**/3.04	28.8	**.235**/.279	18.7
1.2	8.0	300	No	**2.76**/4.00	44.9	**.159**/.230	44.7
1.2	8.0	500	No	**4.04**/4.36	7.9	**.189**/.178	5.8
1.2	10.0	50	No	**2.57**/3.11	21.0	**.587**/.407	30.7
1.2	10.0	300	No	**3.84**/5.26	37.0	**.159**/.418	162.9
1.2	10.0	500	No	**3.33**/5.74	72.4	**.345**/.322	6.7
1.3	8.0	300	No	**1.81**/3.93	117.1	**.041**/.183	346.3
1.3	8.0	500	No	**1.70**/4.31	153.4	**.019**/.143	652.6
1.0	8.0	55	Yes	**2.52**/2.90	15.1	**.376**/.515	37.0
1.0	8.0	400	Yes	**4.88**/4.45	8.8	**.326**/.337	3.4
1.2	8.0	300	Yes	**5.04**/5.38	6.7	**.451**/.447	0.9
1.2	10.0	300	Yes	**6.34**/6.98	10.1	**.727**/.775	6.6
1.3	8.0	300	Yes	**4.26**/5.84	37.1	**.272**/.434	59.6
1.5	10.0	300	Yes	**7.26**/7.57	4.3	**.469**/.556	18.6

(**Measured** / Predicted)

4.4.4 Experimental Results for Irregular Waves

The data acquired during testing of the coupled WEC system in irregular waves provides insight into the devices transient response to a wide range of loading conditions that prevail in a random sea environment. The focus in this analysis is on the overall performance of the device, measured as its average power generation. Additionally, the WEC system's maximum relative velocity and peak power generation are also of interest, as there could be design limitations dependent upon these values.

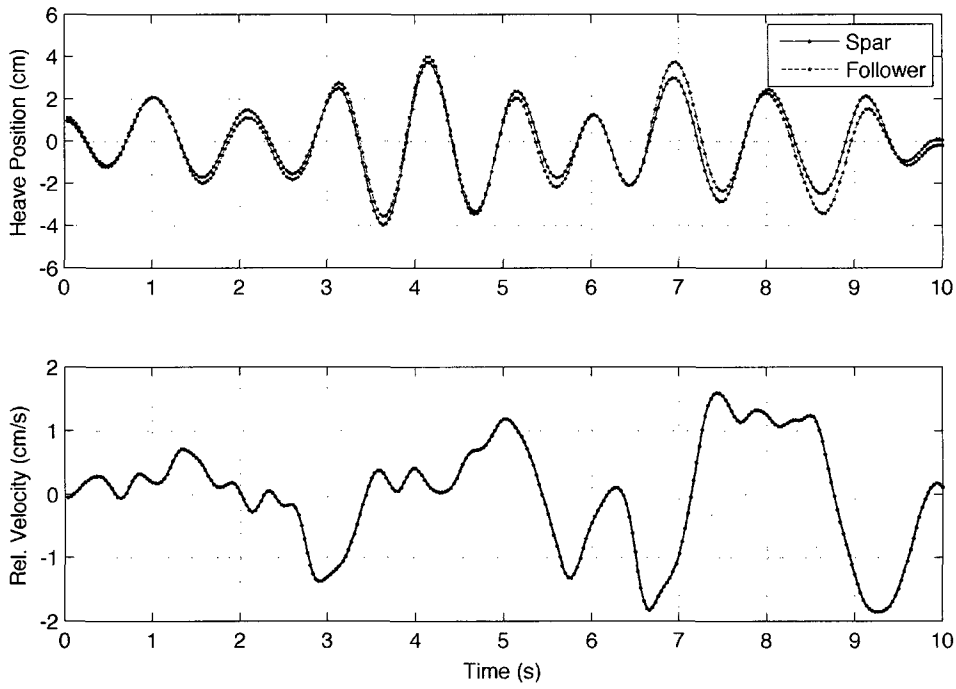

Figure 4-15: Motion response of the WEC system in irregular waves. Buoy position (top), relative velocity (bottom) as a function of time.

A 10 second snapshot of the WEC heave movement in an irregular sea is shown in Figure 4-15. The positions of both spar and follower buoys are illustrated in the upper plot, while their relative velocity over the same time span is shown on the

lower plot. The irregularity of the WEC's motion is clearly visible in this figure and results in an equally non-uniform power generation.

Examining the power generated during the test, but extending the analysis to 300 seconds, Figure 4-16 shows the instantaneous power produced by the generator as well as the cumulative energy produced over that time frame. The power generated appears as intermittent sharp peaks, denoting generation for only a short time. The accumulation of these bursts of energy can be averaged over time, equal in value to the total *Energy* produced divided by the total *Time* analyzed. For the case illustrated in Figure 4-16, the average power generated is

$$P_{Avg.} = \frac{Total\ Energy}{Total\ Time} = \frac{136.5}{300}\left(\frac{J}{s}\right) = 0.445\ W. \tag{4.3}$$

A summary of the characteristic performance values for the WEC in irregular waves is shown in Table 4.6.

Table 4.6: Values of experimentally measured performance characteristics of WEC in irregular seas

Control Variables			Plate	Max.	Avg.
T_{modal} (s)	$H_{1/3}$ (cm)	$R_L(\Omega)$	Attached	Power (W)	Power (W)
1.0	10	300	No	3.89	.033
1.3	10	300	No	4.86	.047
1.5	15	300	No	4.52	.128
2.0	15	300	No	2.16	.021
1.0	10	300	Yes	2.70	.116
1.3	10	300	Yes	5.36	.243
1.5	15	300	Yes	9.55	.445
2.0	15	300	Yes	5.63	.263

(Power data analyzed for 320s of runtime)

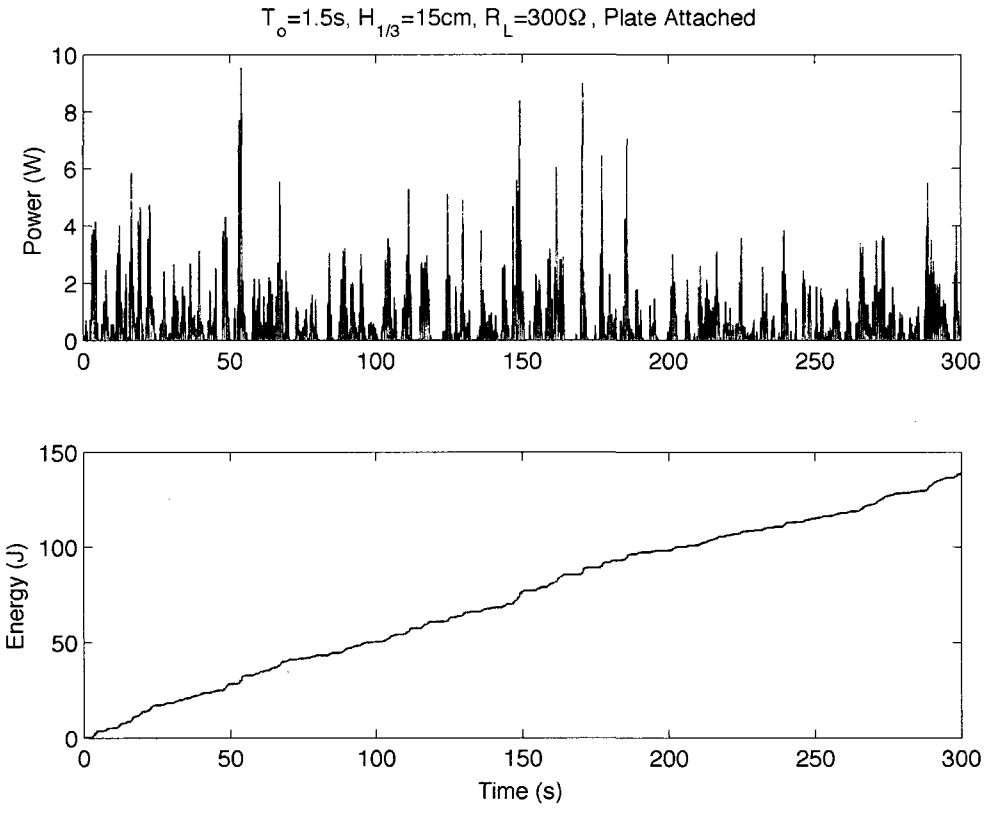

Figure 4-16: Power generation of the WEC system in irregular waves.

4.4.5 Comparison to Computer Simulations in Irregular Waves

For each unique experimental setup, a simulation utilizing a computer model with identical WEC configuration and sea state was performed. However, while the defining parameters of the sea state (model wave period and significant wave height) are identical, the surface profiles generated independently in the wave tank and computer model utilizing those parameters are not the same. The variations between wave tank and computer simulation surface profiles occur due to the independent randomization of the phase associated with each regular wave profile (of a specific amplitude and frequency), which are combined using superposition to generate an irregular sea. Therefore, a significant amount of time must be evaluated, so

as to capture the statistical majority of waves defined by the wave specturm. As the experimental optical tracking system, OPIE, is limited to 20 seconds of video capture, comparisons between experimental and simulated motion of the WEC can not be accurately made. However, the power generation in irregular seas was recorded for over 5 minutes and is therefore sufficient for comparison to simulations.

Of the experimental and simulated data, the transient power generation, depicting maximum values, and the average power generated were compared. An example plot illustrating both measured and predicted values for power and energy generation for a specific sea-state is shown in Figure 4-17.

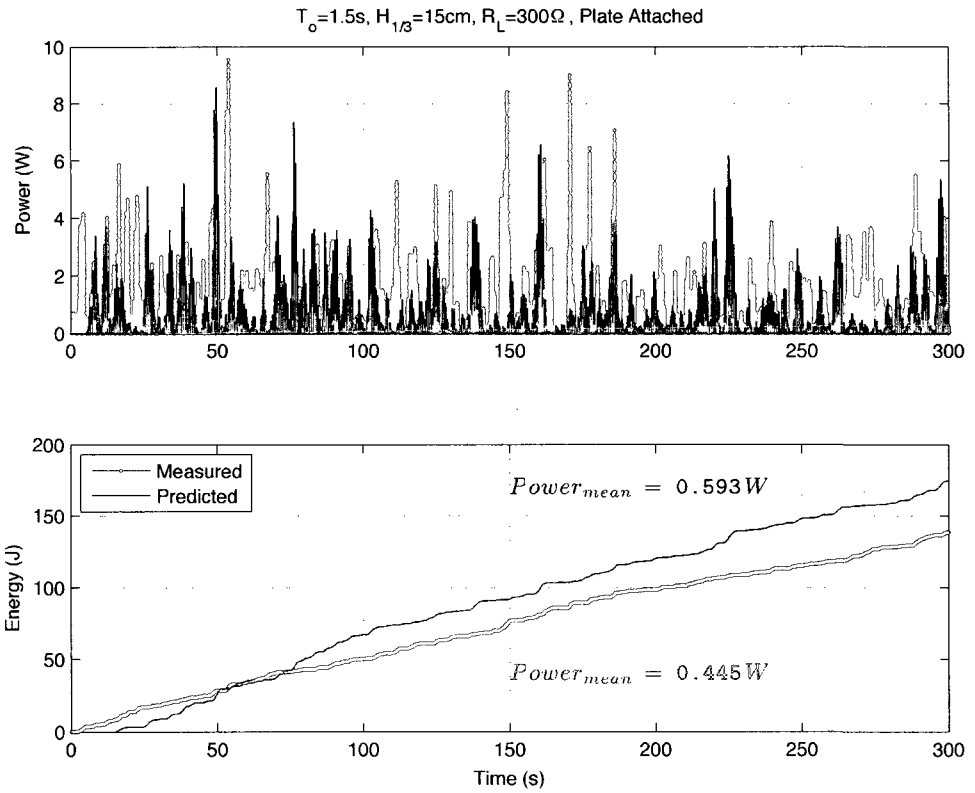

Figure 4-17: Comparison of experimental power generation in irregular waves to simulated power generation.

For each of the evaluated configurations of the WEC's performance in irregular

waves, the maximum and average power generated are compared in Table 4.7.

Table 4.7: Values of experimentally measured performance characteristics of WEC in irregular seas

Control Variables			Plate	Max.	%	Avg.	%
T_{modal} (s)	$H_{1/3}$ (cm)	$R_L(\Omega)$	Attached	Power (W)	Error	Power (W)	Error
1.0	10	300	No	**3.89**/.975	74.9	**.033**/.051	54.5
1.3	10	300	No	**4.86**/2.07	57.4	**.047**/.095	102.1
1.5	15	300	No	**4.52**/5.18	14.6	**.128**/.289	125.8
2.0	15	300	No	**2.16**/2.80	29.7	**.021**/.128	509.5
1.0	10	300	Yes	**2.70**/1.63	39.6	**.116**/.091	21.6
1.3	10	300	Yes	**5.36**/3.94	26.5	**.243**/.213	12.3
1.5	15	300	Yes	**9.55**/8.59	10.1	**.445**/.593	33.3
2.0	15	300	Yes	**5.63**/4.48	20.4	**.263**/.307	16.7

(**Measured** / Predicted)

4.5 Discussion of Validation Results

Mechanical System

The predicted average power generation of the WEC system, performed by driving controlled relative displacement in an oscillatory motion, was 5% larger than the measured value, on average. This small error illustrates the ability of the model to accurately predict the generators performance. However, as seen in the time-series power generation plots, the model predicts a smooth power curve, while the measured response is noisy and oscillates about the predicted values. The lack of variance in the output of the model is due to first-order assumptions made during the representation of the generator with an equivalent circuit, and provides

a valid response for dynamics the generator undergoes during operation for the WEC system.

Uncoupled Buoy Forcing

Comparison of the measured uncoupled response of the spar and follower buoys to their predicted response provides validation data to quantify the validity of the modeling approach. For the follower buoy, the model's predictions for the RAO values were within ± 7.5 % of the measured values. This represents good correlation and instills confidence in the models ability to predict the dynamic response of the uncoupled follower buoy.

However, the model's prediction of the spar buoys response shows large errors when compared to the measured values. For the cases when no damping plate is attached to the spar, the measured heave response of the spar buoy at wave periods of $1.0s$ and $1.2s$ showed maximum displacements of $1.6cm$ and $2.3cm$, corresponding to RAO values of 0.20 and 0.29, respectively. Small heave displacements such as these, are subject to varied sources of error attributed to both the measurement system and the experimental setup. It is likely that the experimentally measured heave motion was effected by buoy pitching, thereby altering its fixed reference vertical position. Additionally, frictional interaction between the spar and follower buoys during testing could have induced spar buoy motion, as the follower buoy was moving with a large displacement almost equivalent to the wave height (RAO$\approx$ 1).

For test cases when a damping plate was attached to the spar buoy, any frictional interaction between follower and spar would have had less of an effect on the spar's heave dynamics, as the plate adds significant resistance to spar movement. In

these cases, it is likely that experimentally measured values were more influenced by any pitching the spar experienced and error associated with the measurement system, which could account for up to $2cm$ of displacement error. For large buoy displacements, such as the spar buoy's $17.6cm$ displacement at a period of $2.0s$, the $2cm$ displacement error would equate to a maximum of about 11% error. However, for small buoy displacements of about $2cm$, as discussed above, the maximum error would equate to 100%.

While the spar buoys measured RAO values showed large errors compared to predicted RAO values, there is evidence to suggest the error was largely attributed to the inability of the model to compensate for the influence of pitching combined with experimental optical position tracking error. The results are, therefore, inconclusive in providing support for or against the models ability to correctly predict the dynamic influence of regular wave forcing on the spar buoy.

Coupled Buoy Forcing in Regular Waves

In regular waves the WEC generally maintained cyclical performance, repeating its heave dynamics and power generation over each wave period. For cases when no damping plate was attached to the spar, the model predicted average power generation typically within 25% of the measured value. Two major outliers, which showed very high percent errors, were the tests performed with wave periods of $1.3s$. In these cases, significant pitching motion prevented the WEC from heaving, resulting in very little power generation and poor correlation to the model's predictions.

The accuracy of the model's predictions showed an overall improvement for cases that included the damping plate attached to the spar. Half of these tests had

predictions of power generation within ±0.9-6.6% of the measured values, while for the other half of the tests, the model over-predicted the power generation by 18.6-59.6%. The major source of error in these tests included observed pitching at longer wave periods, however, the damping plate did have the effect of minimizing the amount of pitching when compared to tests at the same period without a plate attached.

Coupled Buoy Forcing in Irregular Waves

The WEC's power generation in irregular waves was significantly less than in regular waves. The power generation was fairly random and quickly fluctuated from large power outputs to no generation. The models prediction of the WEC system response overestimated the power generation typically by a factor of two in cases where no damping plate was attached to the spar. Additionally, in those same cases, the model under predicted maximum power generation values by 57.4-74.9% for shorter modal wave periods of 1.0s and 1.3s and over predicted maximum power generation by 14.6-29.7% for the longer modal wave periods of 1.5s and 2.0s.

In cases where the spar buoy did have the damping plate attached, average power generation predicted by the model closely matched that measured in experiments, differing by ±12.3-33.3%. The model prediction of the maximum power generated in those tests also improved slightly, resulting in an underestimation of 10.1-39.6%.

It is likely that the improved accuracy of predictions for cases when the damping plate was attached to the spar, is the result of spar buoy generally being less responsive to incident wave forcing thereby limiting its motion, and making the system respond with only a single degree of freedom (i.e., the follower buoy motion).

CHAPTER 5

Scaled Modeling Predictions

5.1 Overview

Utilizing measurements of a correctly scaled model allows for quantification of how a real world (i.e., full-scale) device might perform under similar conditions. Physical modeling relies on the small-scale model behaving in a similar way to the large-scale device, allowing evaluation of expected performance and reduction or elimination of costly mistakes. To ensure accurate scaling, dimensional similitude must be satisfied, that is, the two items must share geometric similarity, kinematic similarity and dynamic similarity, correctly representing length, mass and time, respectively.

Several dimensional scale ratios exist for modeling gravity waves. Of these, the core criterion for the present modeling is similarity of the Froude number, defined as the ratio of the inertial forces extant to the gravitational force

$$Fr = \sqrt{\frac{Inertia\ Force}{Gravity\ Force}} = \frac{V}{\sqrt{gL}}, \tag{5.1}$$

where V is the mean fluid velocity, g is the gravitational constant, and L is the characteristic length. Other dimensional scale ratios are not adopted in this study

as the model is built to a scale at which effects arising from surface tension and viscosity can be assumed negligible (Ipsen, 1960; White, 1994; Kelly, 2007), and it is the inertial and gravitational forces which dominate and proscribe the WEC system dynamics.

Utilizing Froude number scaling, the defining wave parameters are calculated to have the following Froude scaling factors, λ, as explained by Berteaux (1991),

$$\begin{aligned} Wave\ Height\ \ (m),\ \ H_{Full\ Scale} &= \lambda \times H_{Model\ Scale} \\ Wave\ Period\ \ (s),\ \ T_{Full\ Scale} &= \sqrt{\lambda} \times T_{Model\ Scale} \\ Wave\ Length\ \ (m),\ \ L_{Full\ Scale} &= \lambda \times L_{Model\ Scale}. \end{aligned} \tag{5.2}$$

In this analysis, the sea states and WEC performance will be scaled to $\lambda = 25$, representing a physical WEC size 25 times larger than the current prototype.

The scaling of the WEC average power generation is accomplished with the assumption that the percentage of energy extracted during prototype scale wave tank trials in a particular wave environment is the same percentage that would be extracted by a larger WEC defined by Froude scaling. The scaling factor for power generation is

$$Average\ Power\ \ (W),\ \ \overline{P}_{Full\ Scale} = \lambda^{7/2} \times \overline{P}_{Model\ Scale}. \tag{5.3}$$

Using these scaling factors, the power generation predictions from simulations of the WEC are translated to full-scale power generation predictions in a wave environment corresponding to the scaled wave parameters of the simulation.

5.2 Scaled Performance Predictions in Regular Waves

Model simulations for the 1:25 scale WEC in regular waves were performed for a range of wave periods and wave heights similar to those used in the experimental validation wave tank tests. The system was modeled with the damping plate attached to the spar and utilizing a 300 Ω resistive load across the generator. The predicted power generation for the WEC system in each sea state is listed in Table 5.1. These prototype-scale power generation predictions were translated into full-scale (x25) predictions for corresponding wave environments using Equations 5.2 and 5.3, yielding the values presented in Table 5.2.

Table 5.1: Simulated average power generation for the prototype-scale WEC system in regular waves, configured with the damping plate attached and utilizing a 300Ω resistive load.

Wave Period (s)	**Wave Height** (cm)			
	8	**10**	**15**	**20**
1.0	.424	.721	1.84	3.48
1.2	.453	.780	2.02	3.86
1.5	.343	.577	1.44	2.72
2.0	.091	.160	.431	.851

Watts

Table 5.2: Scaled power generation for the full-scale WEC system in corresponding regular wave environments.

Wave Period (s)	**Wave Height** (m)			
	2.0	**2.5**	**3.75**	**5.0**
5.0	33.1	56.3	143	272
6.0	35.4	60.9	158	302
7.5	26.8	45.1	113	212
10.0	7.11	12.5	33.7	66.5

Kilowatts

5.3 Scaled Performance Predictions in Irregular Waves

Model simulations for the WEC in irregular waves defined by the Bretschneider spectrum were performed over a range of modal wave periods and significant wave heights, including several wave conditions supported by experimentally validated wave tank tests. The system was modeled with the damping plate attached to the spar buoy and utilizing a 300 Ω resistive load across the generator. The predicted power generation for the WEC system in each sea state is listed in Table 5.3. These prototype-scale power generation predictions were translated into full-scale (x25) predictions for corresponding wave environments, yielding the values presented in Table 5.4.

Table 5.3: Simulated power generation for the prototype-scale WEC system in irregular waves defined by the Bretschneider spectrum, configured with the damping plate attached and utilizing a 300Ω resistive load.

Modal Wave Period (s)	**Significant Wave Height** (cm)			
	8	**10**	**15**	**20**
1.0	.0516	.0913	.260	.655
1.2	.0945	.175	.558	.782
1.5	.120	.251	.593	1.09
2.0	.0908	.145	.307	.722

$Watts$

Table 5.4: Scaled power generation for the full-scale WEC system in corresponding irregular wave environments.

Modal Wave Period (s)	**Significant Wave Height** (m)			
	2.0	**2.5**	**3.75**	**5.0**
5.0	4.03	7.11	20.3	51.2
6.0	7.38	13.7	43.6	61.1
7.5	9.38	19.6	46.3	85.2
10.0	7.09	11.3	24.0	56.4

Kilowatts

CHAPTER 6

Conclusion

A computer model of the dynamics and power output of a point-absorber-type wave energy converter was developed and evaluated against a 1:25 scale prototype in wave tank tests. Modeling of the system was successfully performed in the Simulink/MATLAB environment using linear wave theory to determine the response of the floating buoys to ocean wave excitation, while the coupled dynamics of the internal components of the power take-off system were derived from first principals and characterized experimentally.

Model simulation was performed in the time domain and results were compared to experimentally measured values for validation. As such, the system was validated by way of both mechanical bench testing and in an independent series of wave tank experiments. Evaluation in regular waves without the damping plate attached to the spar buoy predicted average power generation within 6-54% of the measured value, dismissing outliers due to excessive pitching motion. In irregular waves defined by the Bretscheider spectrum, with no damping plate attached to the spar buoy, the predicted average power generation was within 55-510% of the measured value, varying considerably.

The addition of the damping plate attached to the spar buoy improved model prediction accuracy. In regular waves where the damping plate was used, predic-

tions for the average power generation were within 0.9-37% of the measured value, with half of those predictions being within $\pm 7\%$ of the measured value. In irregular waves with the damping plate attached, predictions of average power generation improved to within 12-33% of the measured value.

Forecasts for full-scale average power generation were made for a range of regular and irregular waves, utilizing the attached damping plate configuration. Power generation in sea states at the University of New Hampshire's wave energy evaluation site is predicted to be $24kW$, where conditions are characterized by irregular waves defined by the Bretschneider spectrum with a significant wave height of $3.75m$ and modal wave period of $10s$.

APPENDIX A

WEC System Specifications

A.1 Summary of WEC System Parameters

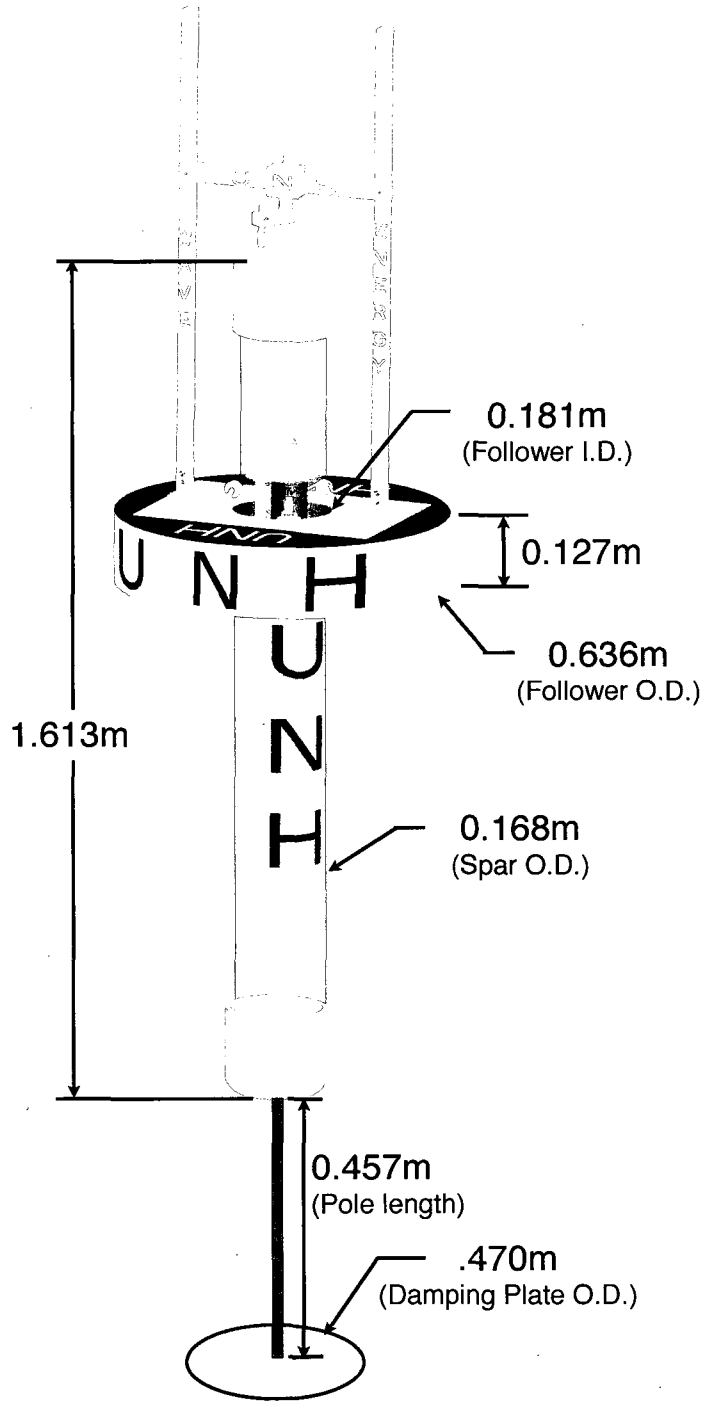

Figure A-1: Overview of the WEC system design and dimensions.

Table A.1: Summary of Simulink Model System Parameters

Global Parameters	
(g) Gravity	$9.81\ m\ s^{-2}$
(ρ) Water Density	$1000\ kg\ m^{-3}$
Spar Buoy	
(A) X-Sectional Area	$0.02224\ m^2$
(D) Draft	$1.145\ m$
(b) Hydrodynamic Damping Coef.	$10.37\ kg\ s^{-1}$
(m) Mass	$25.4\ kg$
(m_{add}) Added Mass	$3.24\ kg$
Spar Buoy with Plate Attached	
(A) X-Sectional Area	$0.02224\ m^2$
(D) Draft	$1.145\ m$
(b) Hydrodynamic Damping Coef.	$58.23\ kg\ s^{-1}$
(m) Mass	$28.6\ kg$
(m_{add}) Added Mass	$52.84\ kg$
Follower Buoy	
(A) X-Sectional Area	$0.2910\ m^2$
(D) Draft	$0.03192\ m$
(b) Hydrodynamic Damping Coef.	$225.2\ kg\ s^{-1}$
(m) Mass	$9.3\ kg$
(m_{add}) Added Mass	$74.79\ kg$
Transmission	
(r_1) Radius of gear 1	$0.01270\ m$
(r_2) Radius of gear 2	$0.03048\ m$
(r_3) Radius of gear 3	$0.00762\ m$
(J_{eq}) Equivalent Inertia	$6.20046 \times 10^{-5}\ kg\ m^2$
(b_{eq}) Non-linear Damping Func.	$(0.0236)\,(2.089 \times 10^{-8})^{\frac{1}{\omega}} + .0199\ \ kg\ m^2\ rad^{-1}\ s^{-1}$
PM DC GENERATOR	
(K_t) Torque constant	$0.425\ N\ m\ A^{-1}$
(K_e) Back e.m.f. constant	$0.425\ V\ rad^{-1}\ sec^{-1}$
(L_a) Inductance	$40 \times 10^{-3}\ H$
(R_a) Armature Resistance	$24.6\ \Omega$
(R_L) Resistive Load	$50\text{-}500\ \Omega$
(V_B) Voltage Drop Across Brushes	$0.76\ V$
(J_{gen}) Inertia	$9.0617 \times 10^{-5}\ kg\ m^2$
(b_{gen}) Damping Coef.	$7.993 \times 10^{-5}\ kg\ m^2\ rad^{-1}\ sec^{-1}$
(τ_m) Mechanical time constant	$12.75\ ms$
(τ_e) Electrical time constant	$2.916\ ms$

A.2 Generator

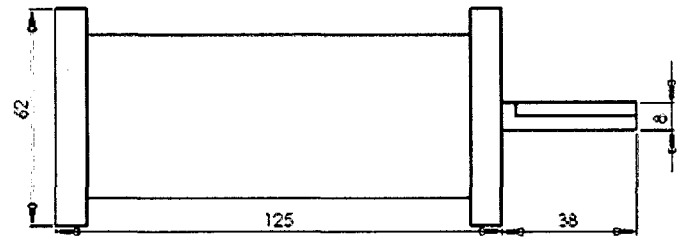

Figure A-2: Permanent Magnet DC Generator Dimensions (mm)

Table A.2: Permanent Magnet DC Generator Details

Magnets	Two high-energy saturated C8 ceramic magnets.
Shaft	Steel 8mm (5/16") diameter, 38mm length, with 1mm full-length flat.
Armature	16-slot armature 52mm diameter would with AWG25 magnet wire (fusing current:24 amps).
Brushes	Extra-long 8x14mm brush assemblies including spring, pigtail, and cap
Bearings	Two double-sealed 32mm OD ball bearings.
Rotation	Either direction.
Speed	Zero to 5,000 rpm - generates at all speeds
Mounting	Four 6mm holes on the front or rear end caps.
Weight	1.5Kg (3.3lb)
Dimensions	150x150x300mm (6x6x12in).
Resistance	21 ohms
Inductance	40 mH

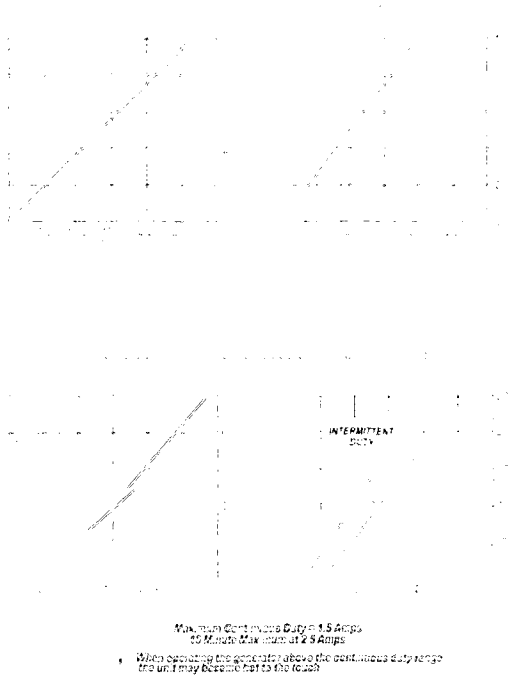

Figure A-3: Permanent Magnet DC Generator Performance Plots

Appendix B

Validation Analysis Plots

B.1 Mechanical Motion Simulator

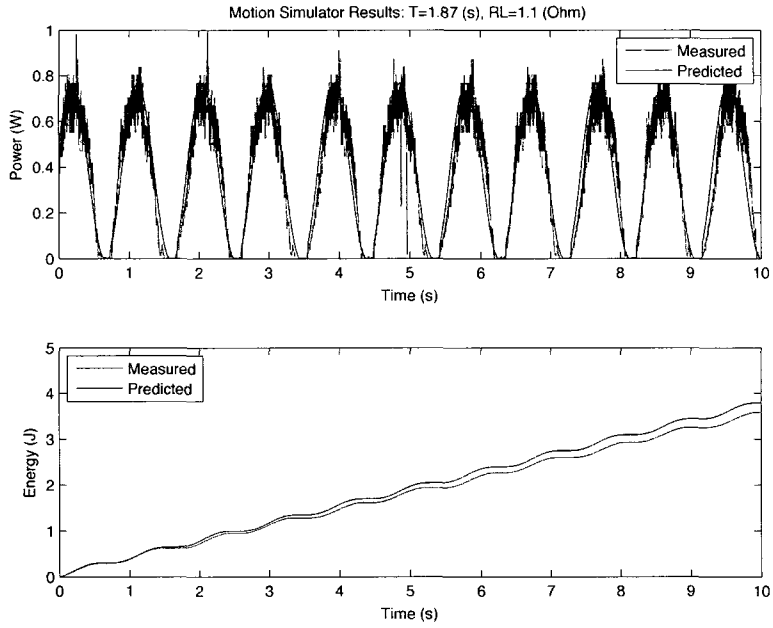

Figure B-1: Validation comparisons of the mechanically driven WEC utilizing an oscillating amplitude of $H = 9.9cm$, a period of $T = 1.87s$, and a resistive load of $R_L = 1.1\Omega$.

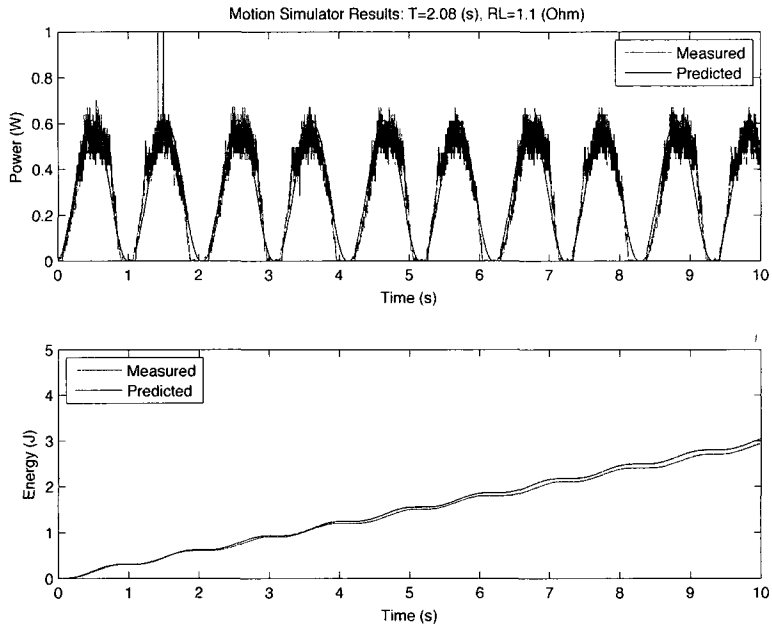

Figure B-2: Validation comparisons of the mechanically driven WEC utilizing an oscillating amplitude of $H = 9.9cm$, a period of $T = 2.08s$, and a resistive load of $R_L = 1.1\Omega$.

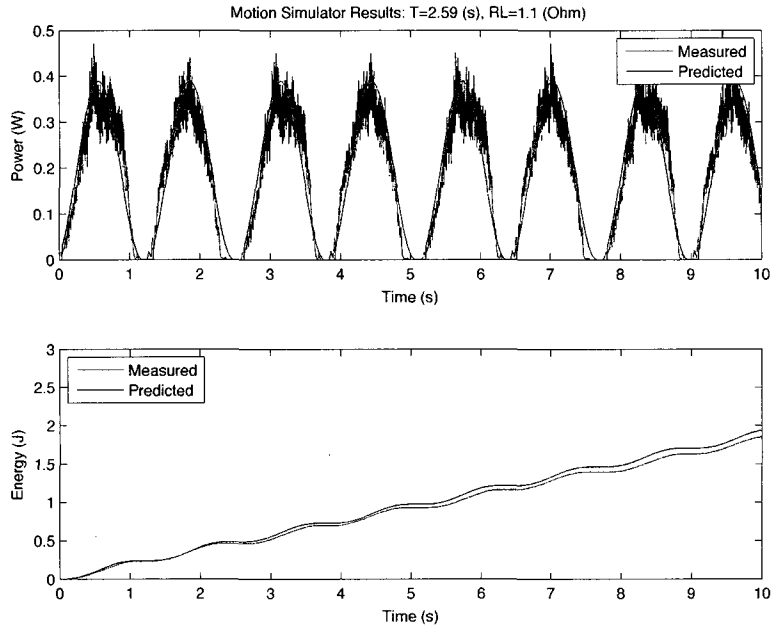

Figure B-3: Validation comparisons of the mechanically driven WEC utilizing an oscillating amplitude of $H = 9.9cm$, a period of $T = 2.59s$, and a resistive load of $R_L = 1.1\Omega$.

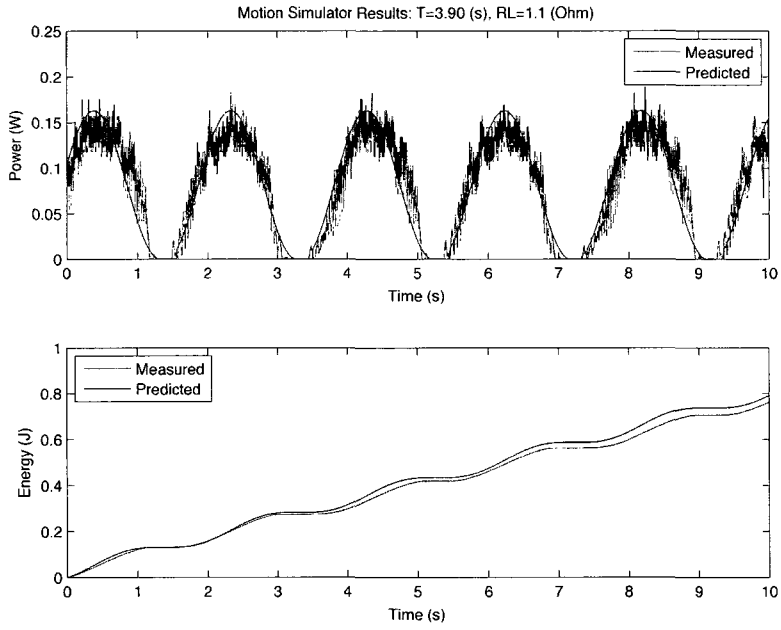

Figure B-4: Validation comparisons of the mechanically driven WEC utilizing an oscillating amplitude of $H = 9.9cm$, a period of $T = 3.90s$, and a resistive load of $R_L = 1.1\Omega$.

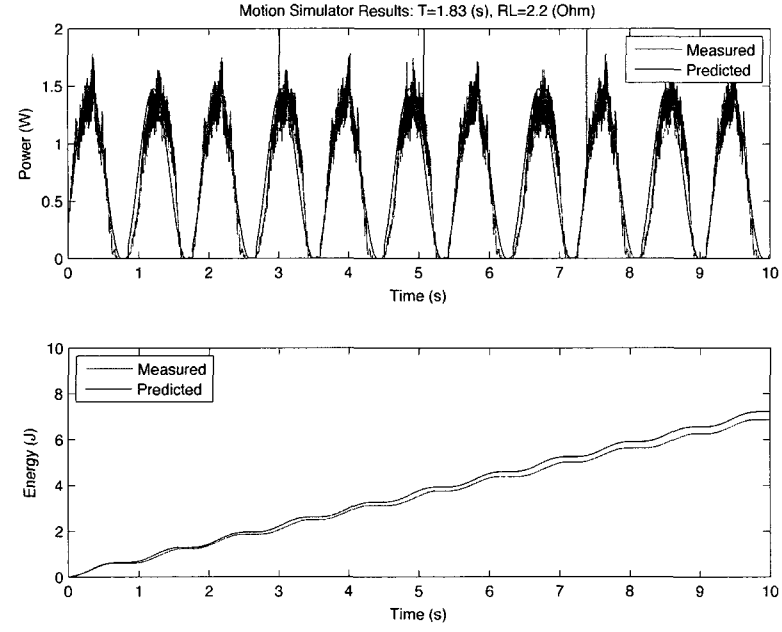

Figure B-5: Validation comparisons of the mechanically driven WEC utilizing an oscillating amplitude of $H = 9.9cm$, a period of $T = 1.83s$, and a resistive load of $R_L = 2.2\Omega$.

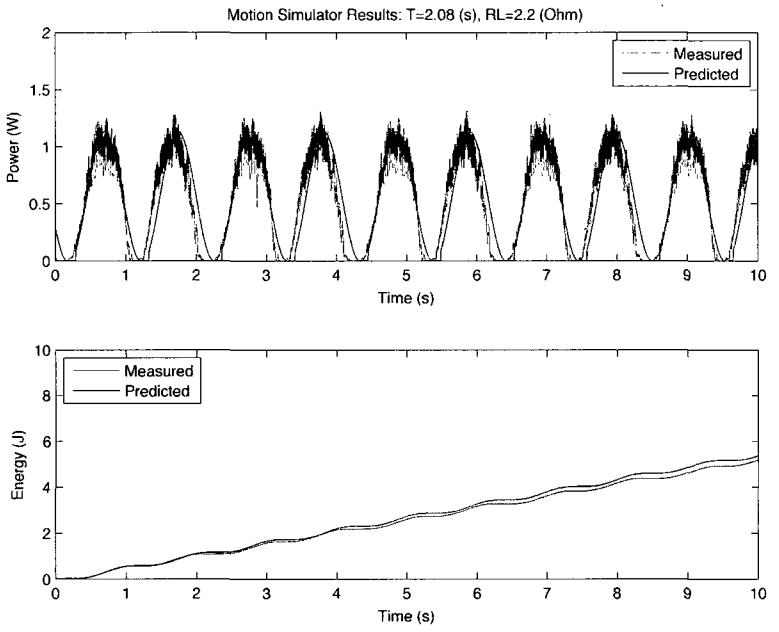

Figure B-6: Validation comparisons of the mechanically driven WEC utilizing an oscillating amplitude of $H = 9.9cm$, a period of $T = 2.08s$, and a resistive load of $R_L = 2.2\Omega$.

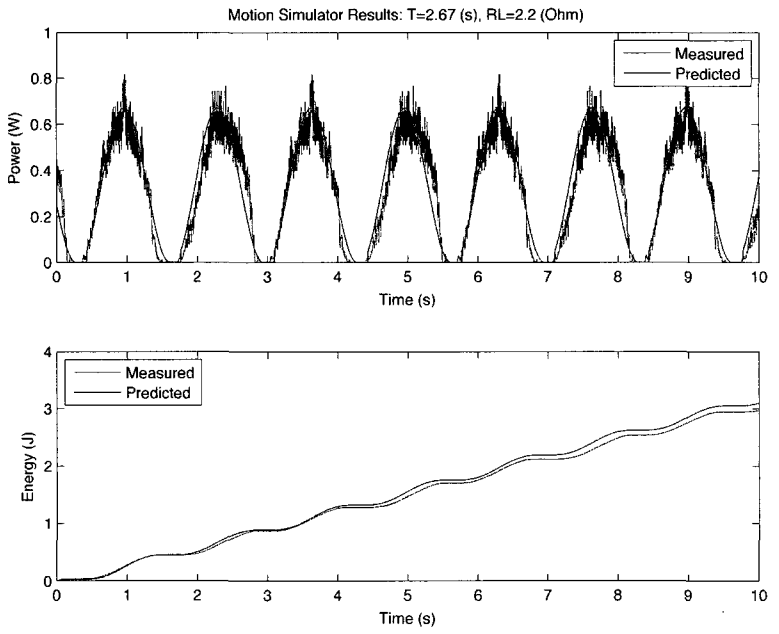

Figure B-7: Validation comparisons of the mechanically driven WEC utilizing an oscillating amplitude of $H = 9.9cm$, a period of $T = 2.67s$, and a resistive load of $R_L = 2.2\Omega$.

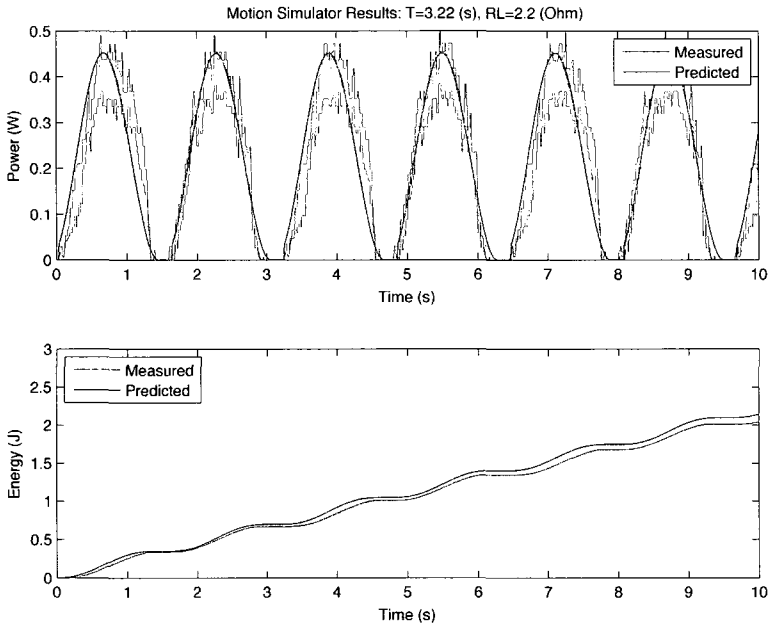

Figure B-8: Validation comparisons of the mechanically driven WEC utilizing an oscillating amplitude of $H = 9.9cm$, a period of $T = 3.22s$, and a resistive load of $R_L = 2.2\Omega$.

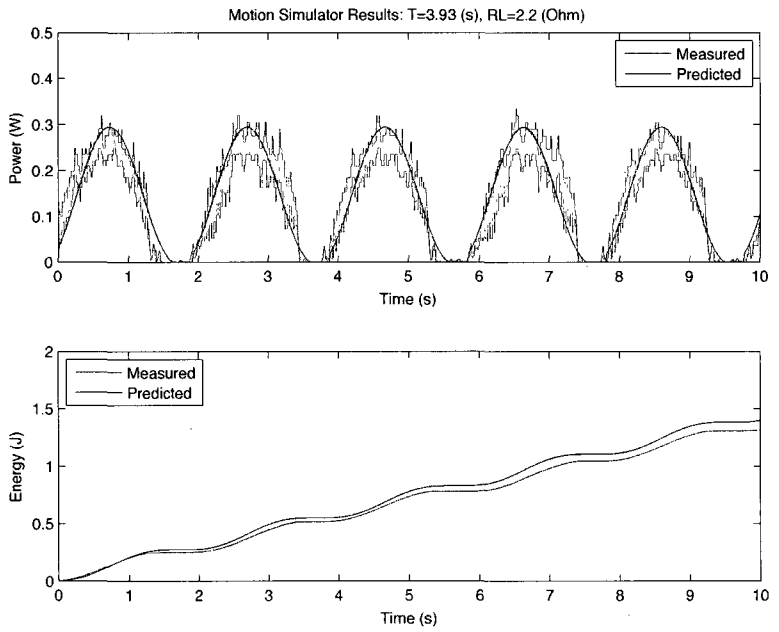

Figure B-9: Validation comparisons of the mechanically driven WEC utilizing an oscillating amplitude of $H = 9.9cm$, a period of $T = 3.93s$, and a resistive load of $R_L = 2.2\Omega$.

B.2 Uncoupled Buoys in Regular Waves

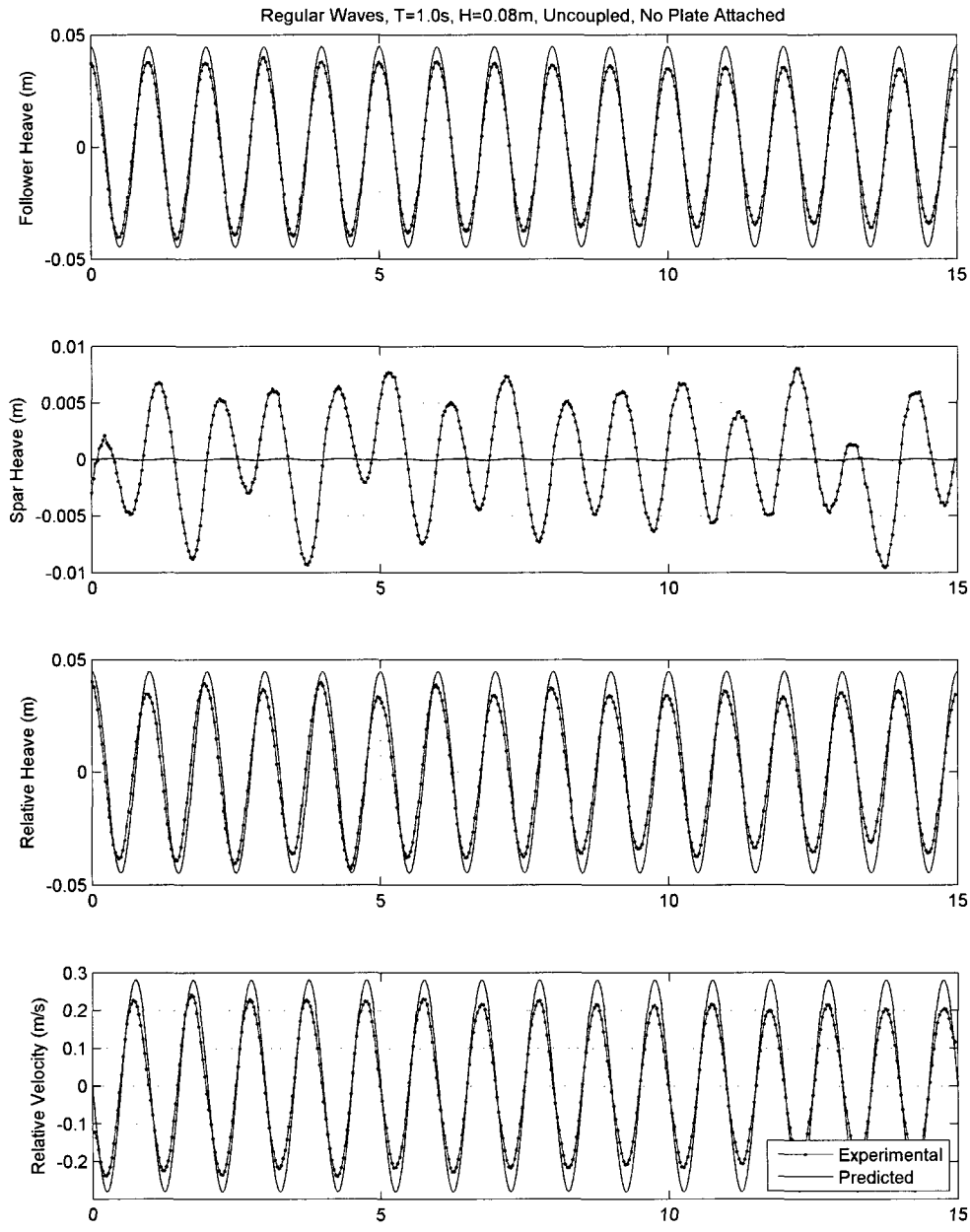

Figure B-10: Validation comparisons for uncoupled WEC System with no submerged plate. ($T = 1.0s$ *and* $H = 0.08m$)

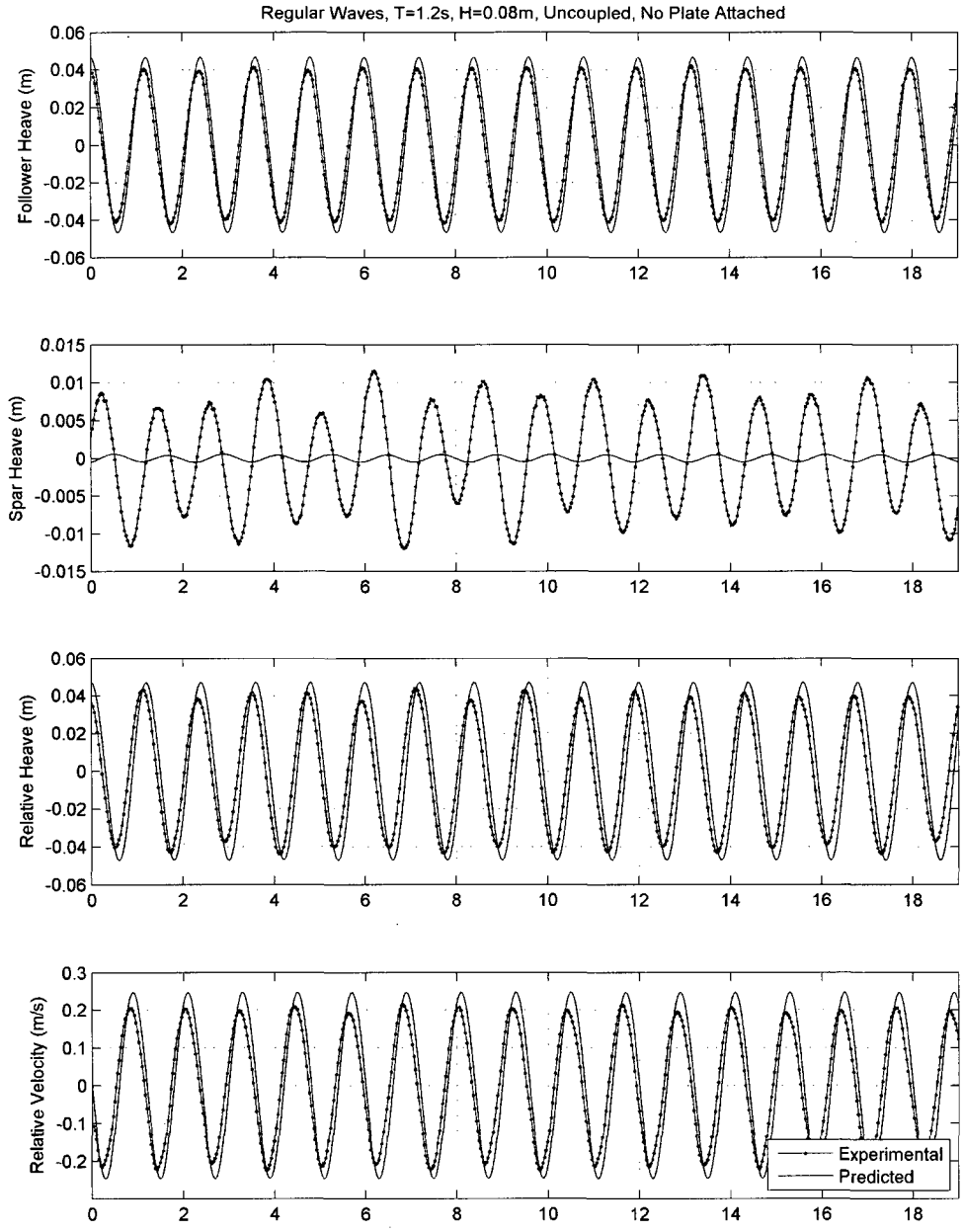

Figure B-11: Validation comparisons for uncoupled WEC System with no submerged plate. ($T = 1.2s$ *and* $H = 0.08m$)

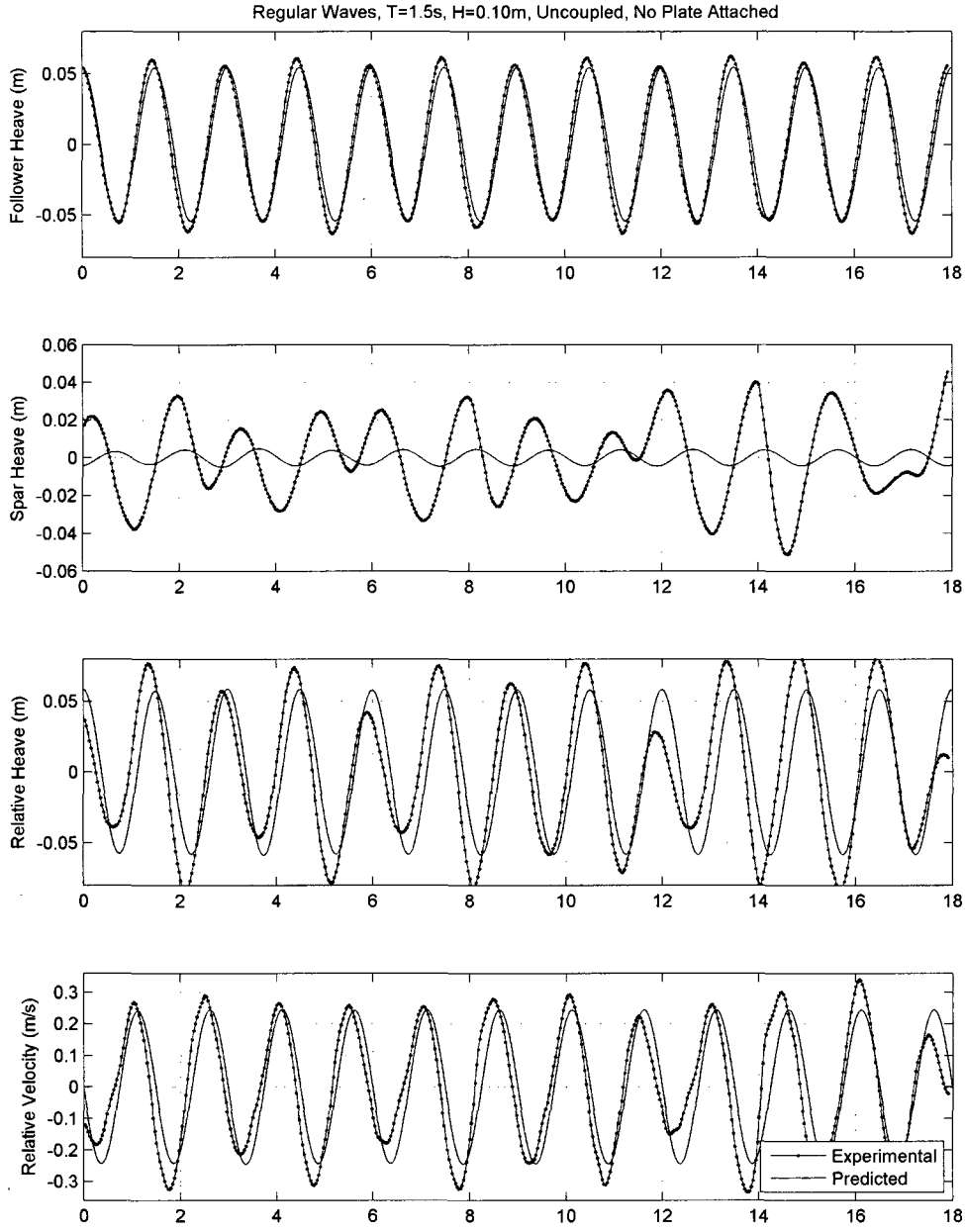

Figure B-12: Validation comparisons for uncoupled WEC System with no submerged plate. ($T = 1.5s$ *and* $H = 0.10m$)

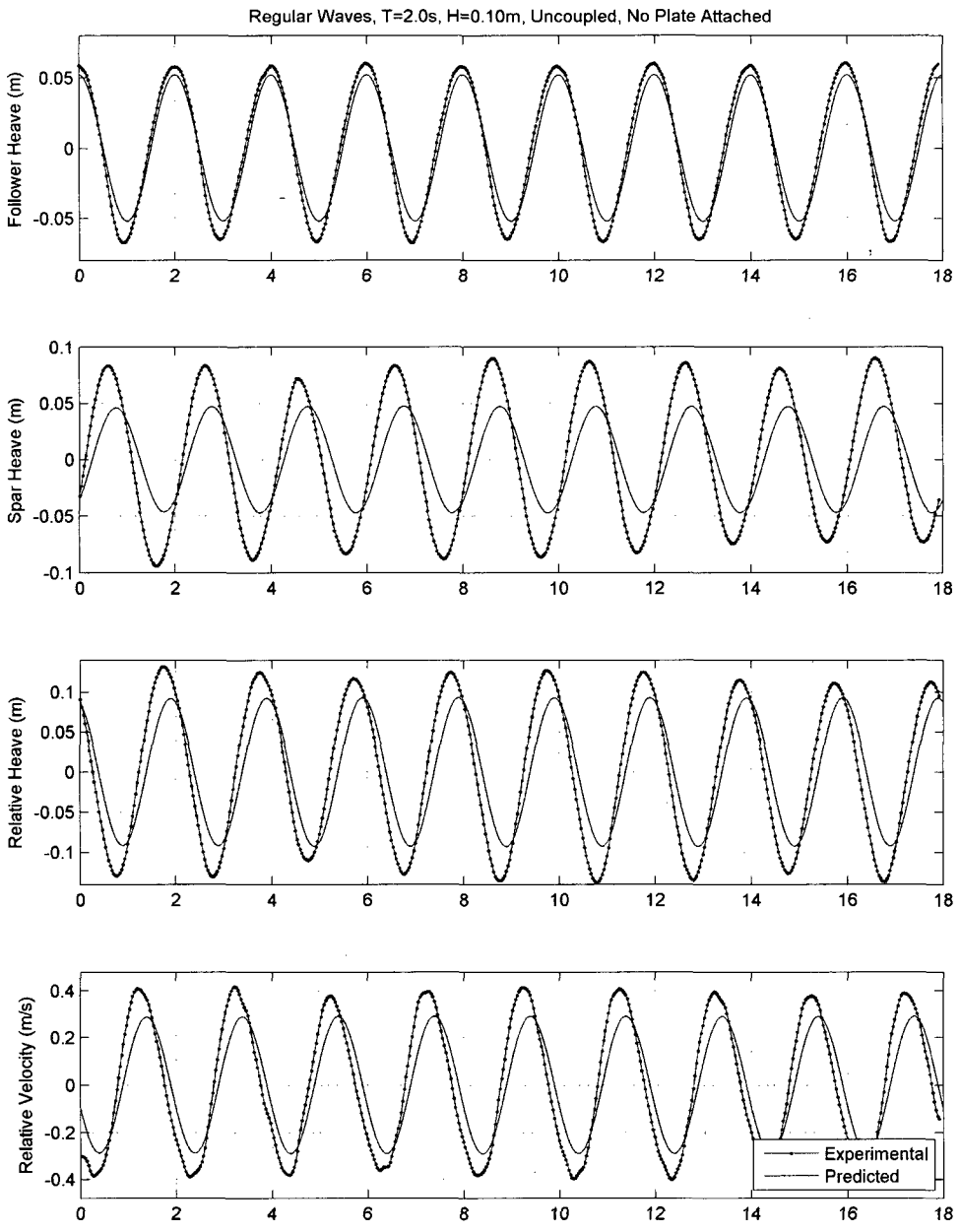

Figure B-13: Validation comparisons for uncoupled WEC System with no submerged plate. ($T = 2.0s$ *and* $H = 0.10m$)

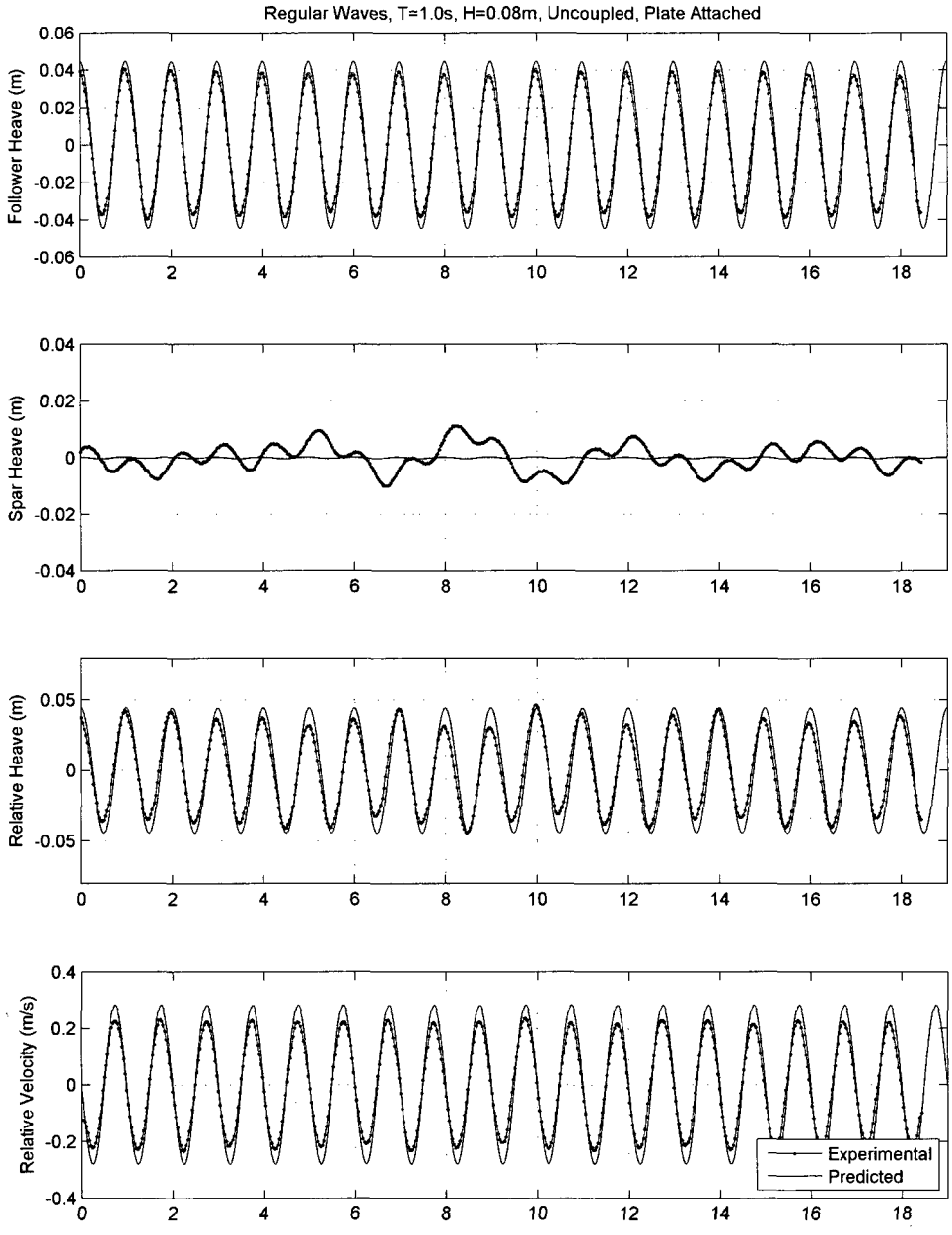

Figure B-14: Validation comparisons for uncoupled WEC System with submerged plate. ($T = 1.0s$ *and* $H = 0.08m$)

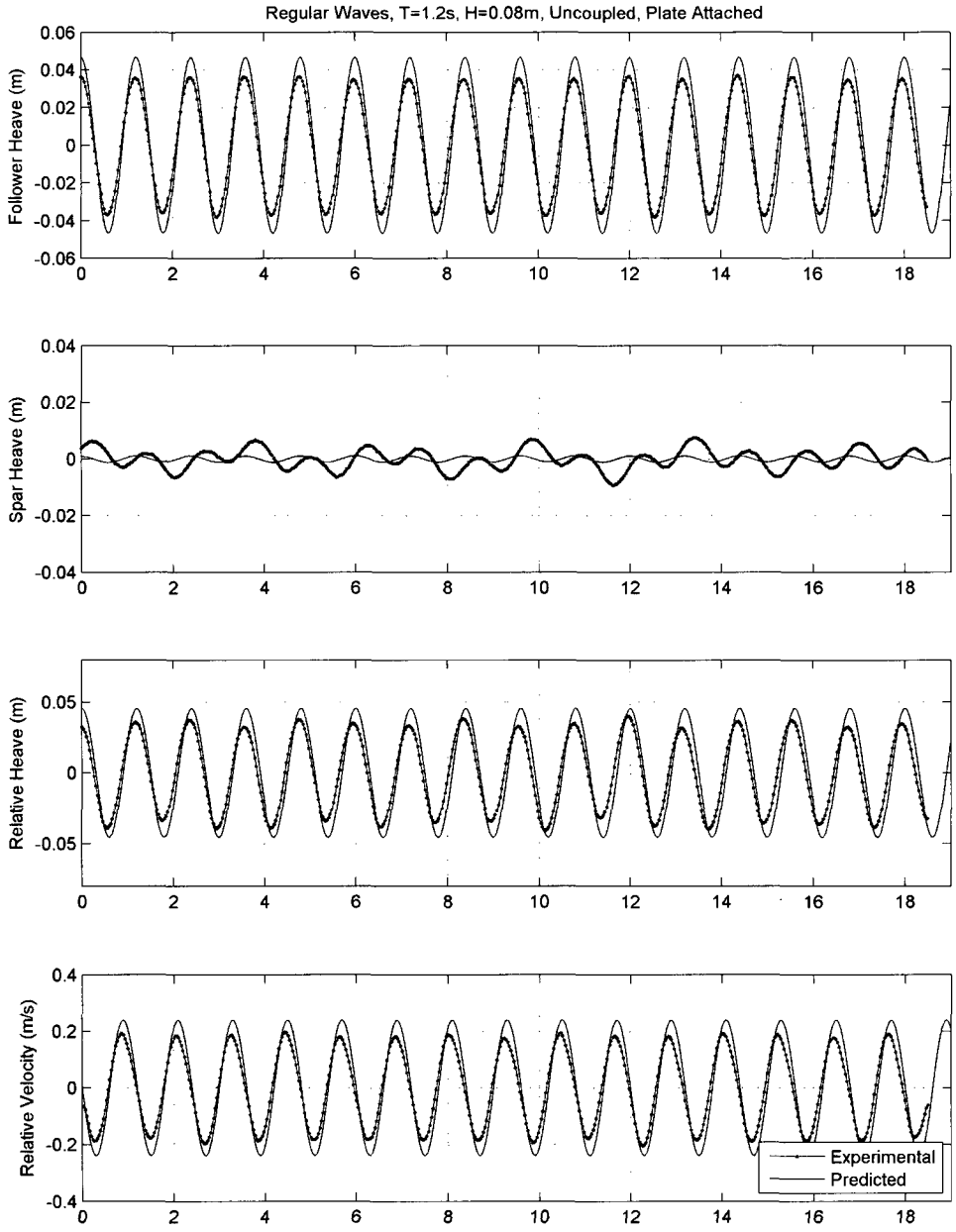

Figure B-15: Validation comparisons for uncoupled WEC System with submerged plate. ($T = 1.2s$ *and* $H = 0.08m$)

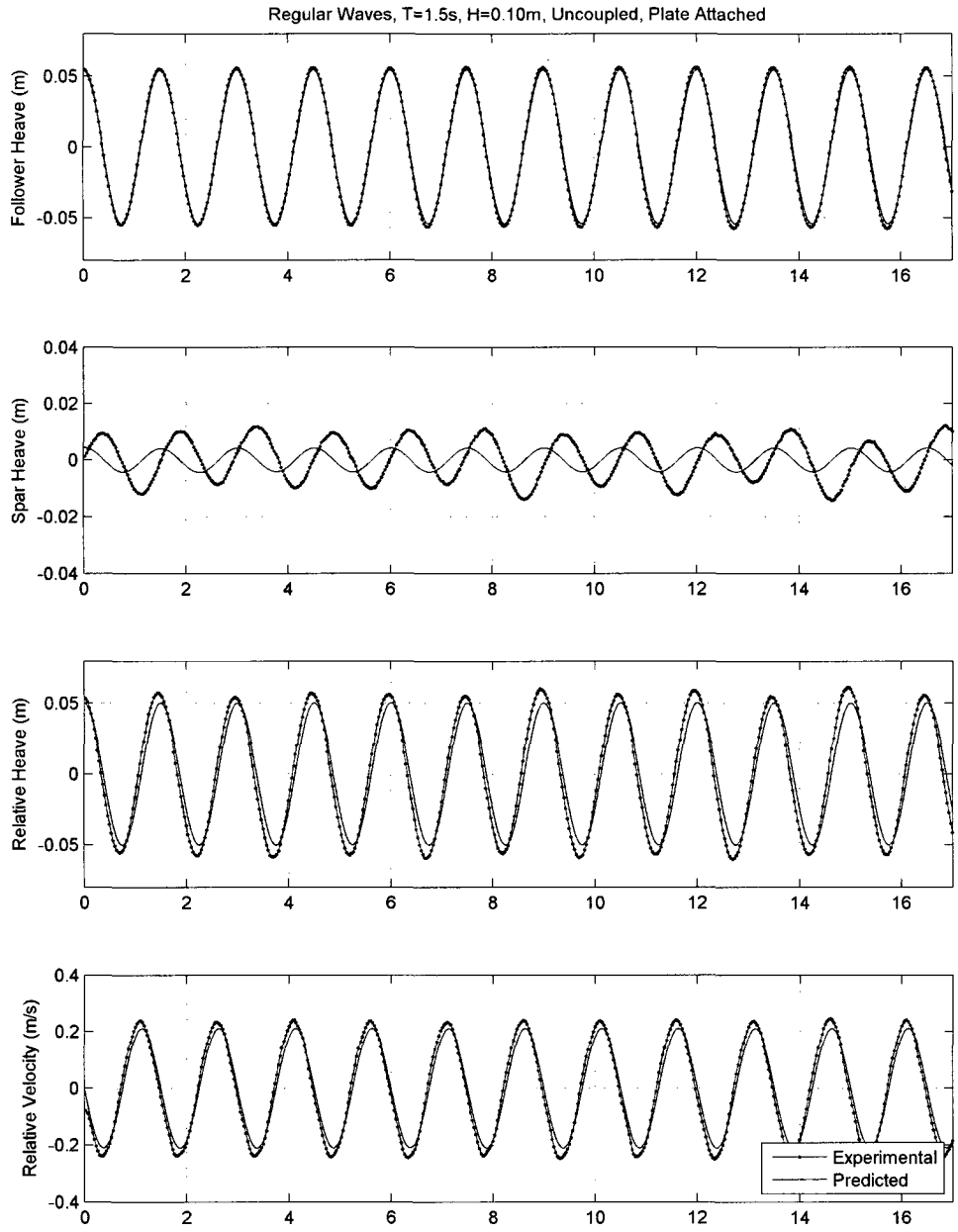

Figure B-16: Validation comparisons for uncoupled WEC System with submerged plate. ($T = 1.5s$ *and* $H = 0.10m$)

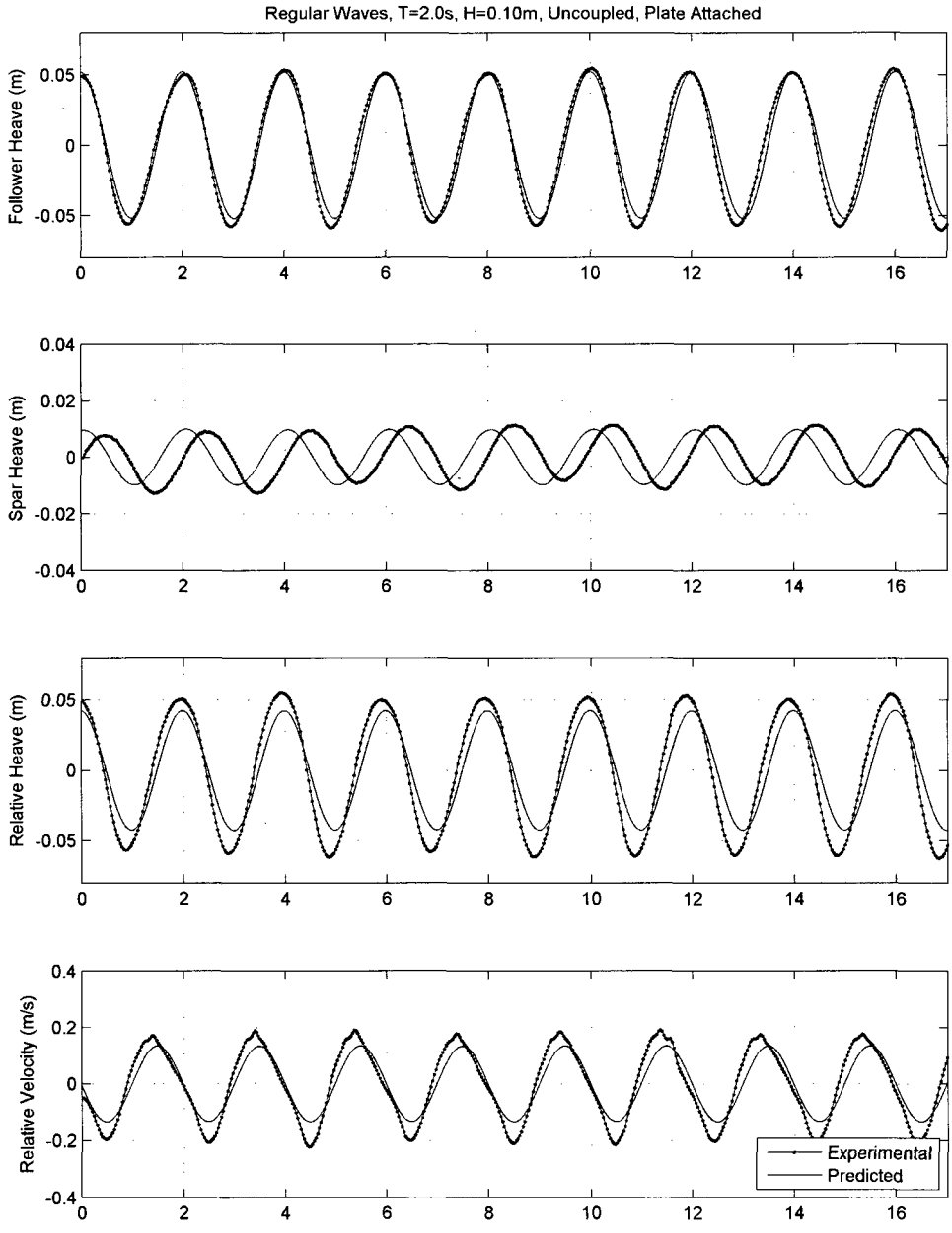

Figure B-17: Validation comparisons for uncoupled WEC System with submerged plate. ($T = 2.0s$ *and* $H = 0.10m$)

B.3 Coupled WEC System in Regular Waves

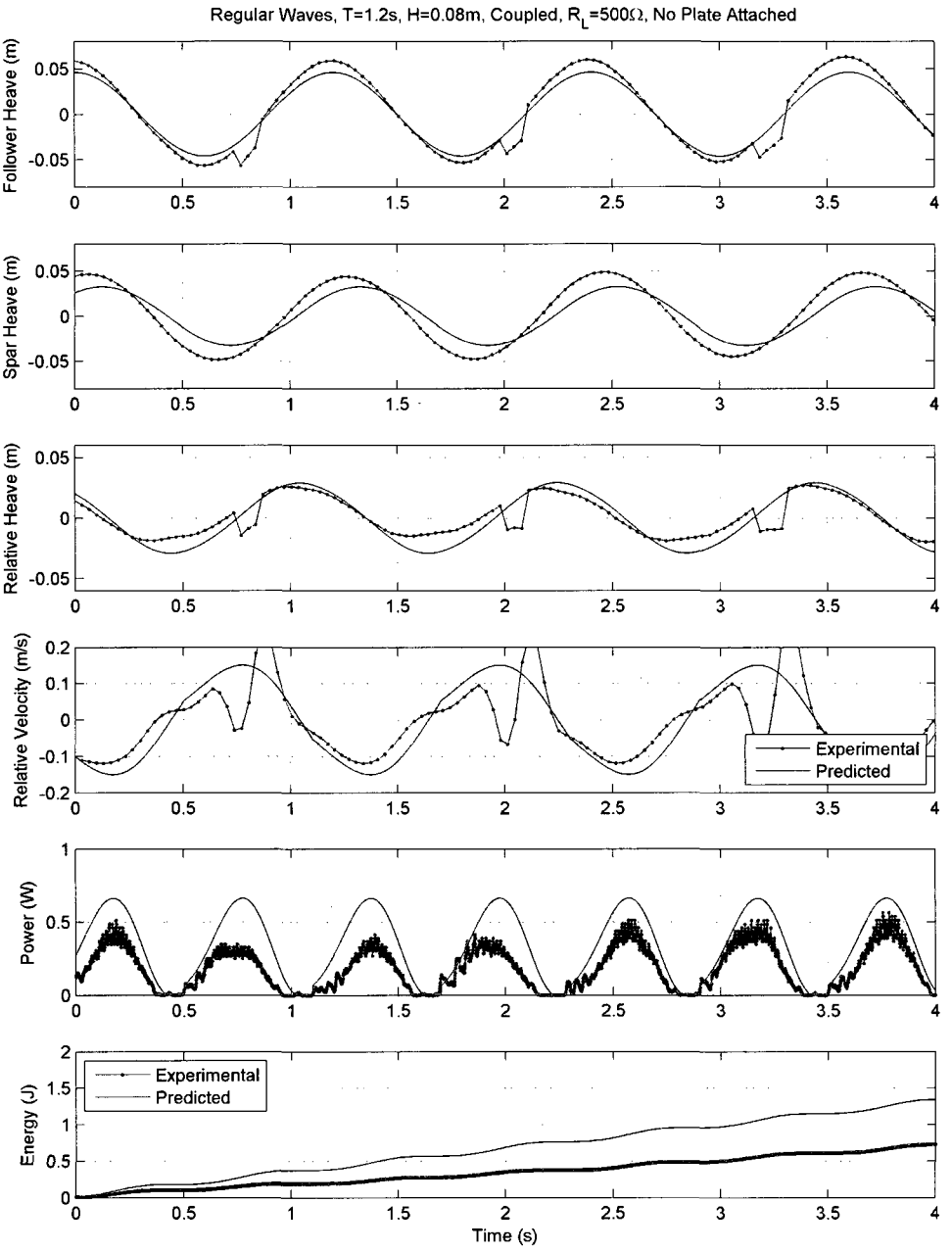

Figure B-18: Validation comparisons for coupled WEC System with no submerged plate. ($T = 1.2s,\ H = 0.08m,\ and\ R_L = 500\Omega$)

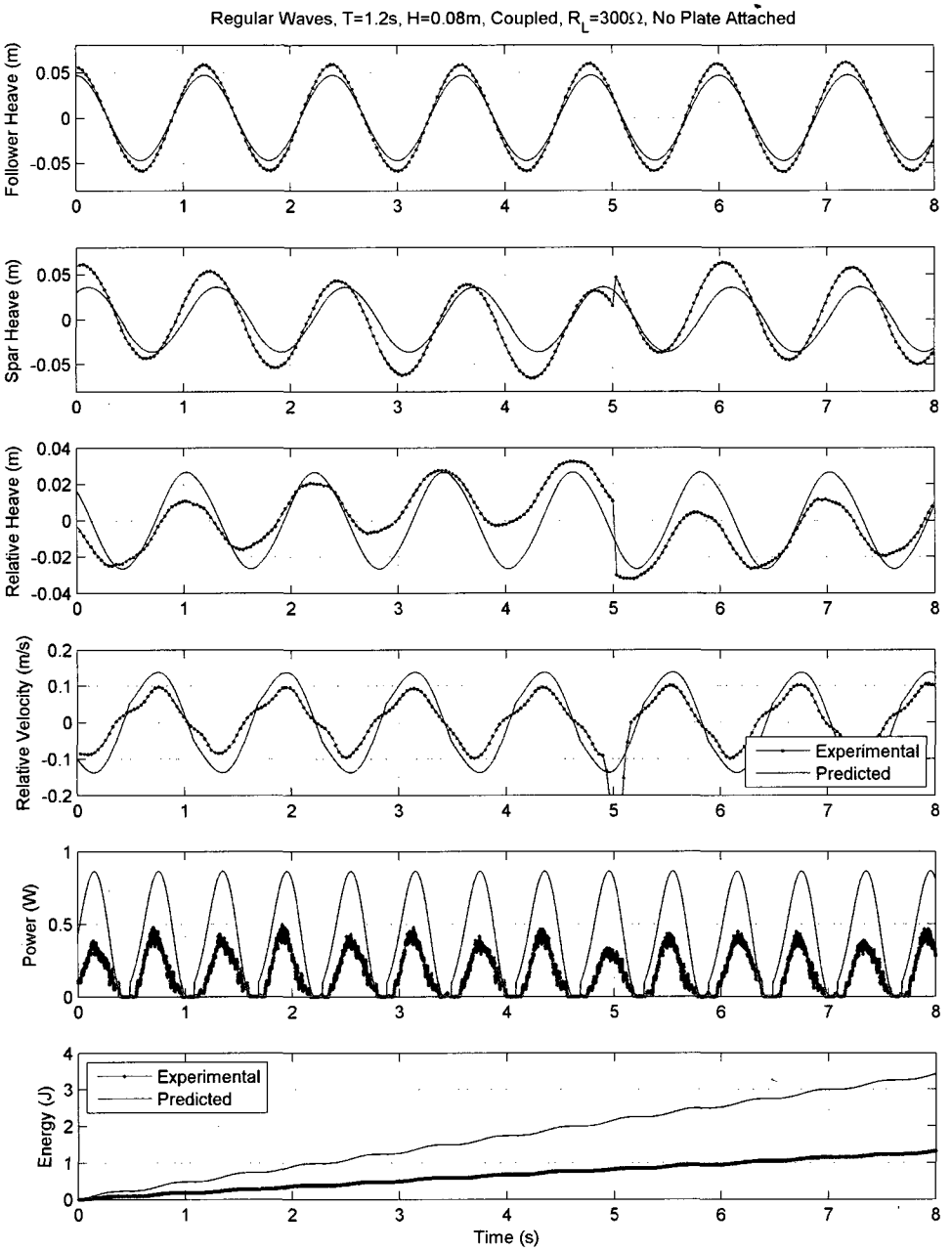

Figure B-19: Validation comparisons for coupled WEC System with no submerged plate. ($T = 1.2s$, $H = 0.08m$, *and* $R_L = 300\Omega$)

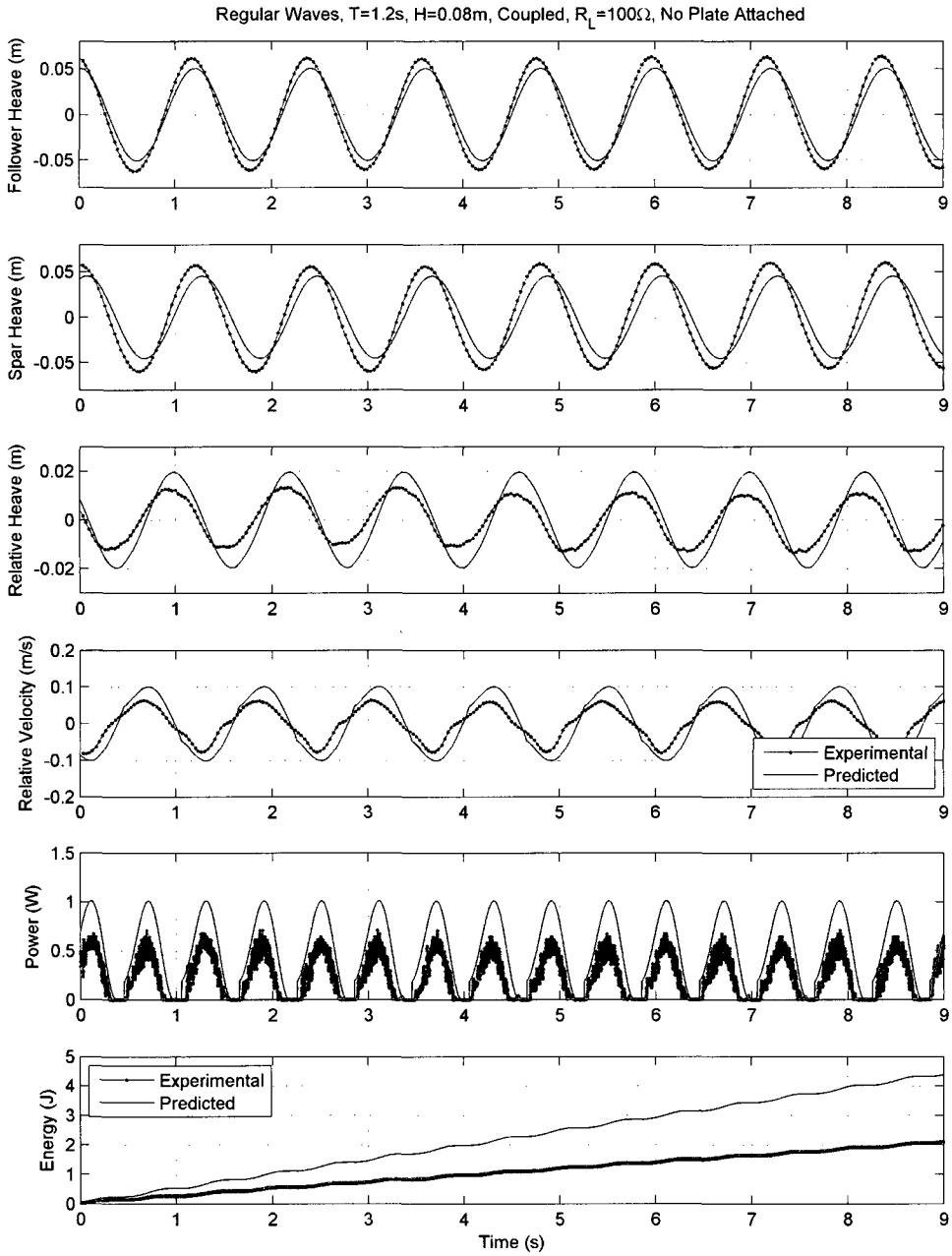

Figure B-20: Validation comparisons for coupled WEC System with no submerged plate. ($T = 1.2s$, $H = 0.08m$, *and* $R_L = 100\Omega$)

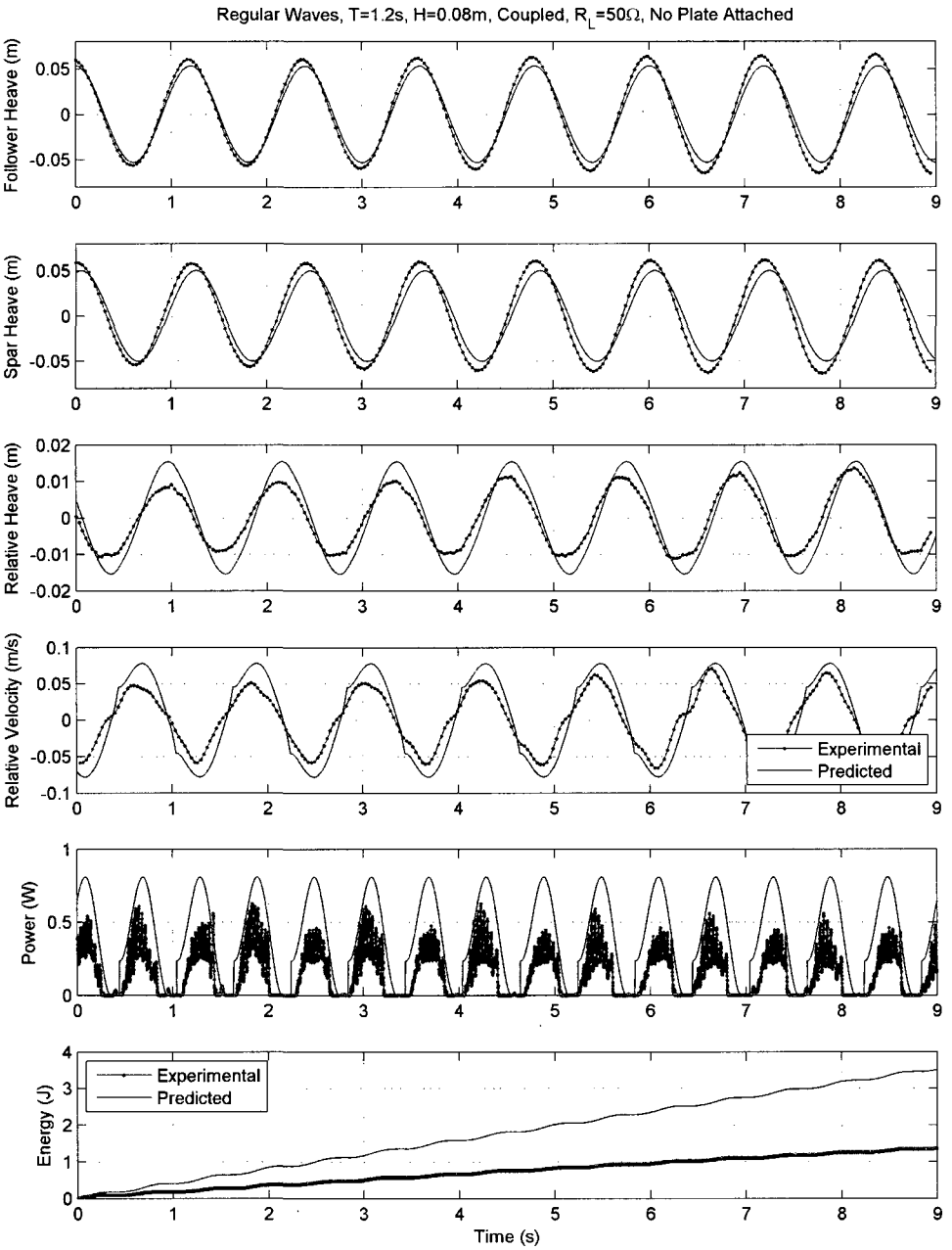

Figure B-21: Validation comparisons for coupled WEC System with no submerged plate. ($T = 1.2s$, $H = 0.08m$, *and* $R_L = 50\Omega$)

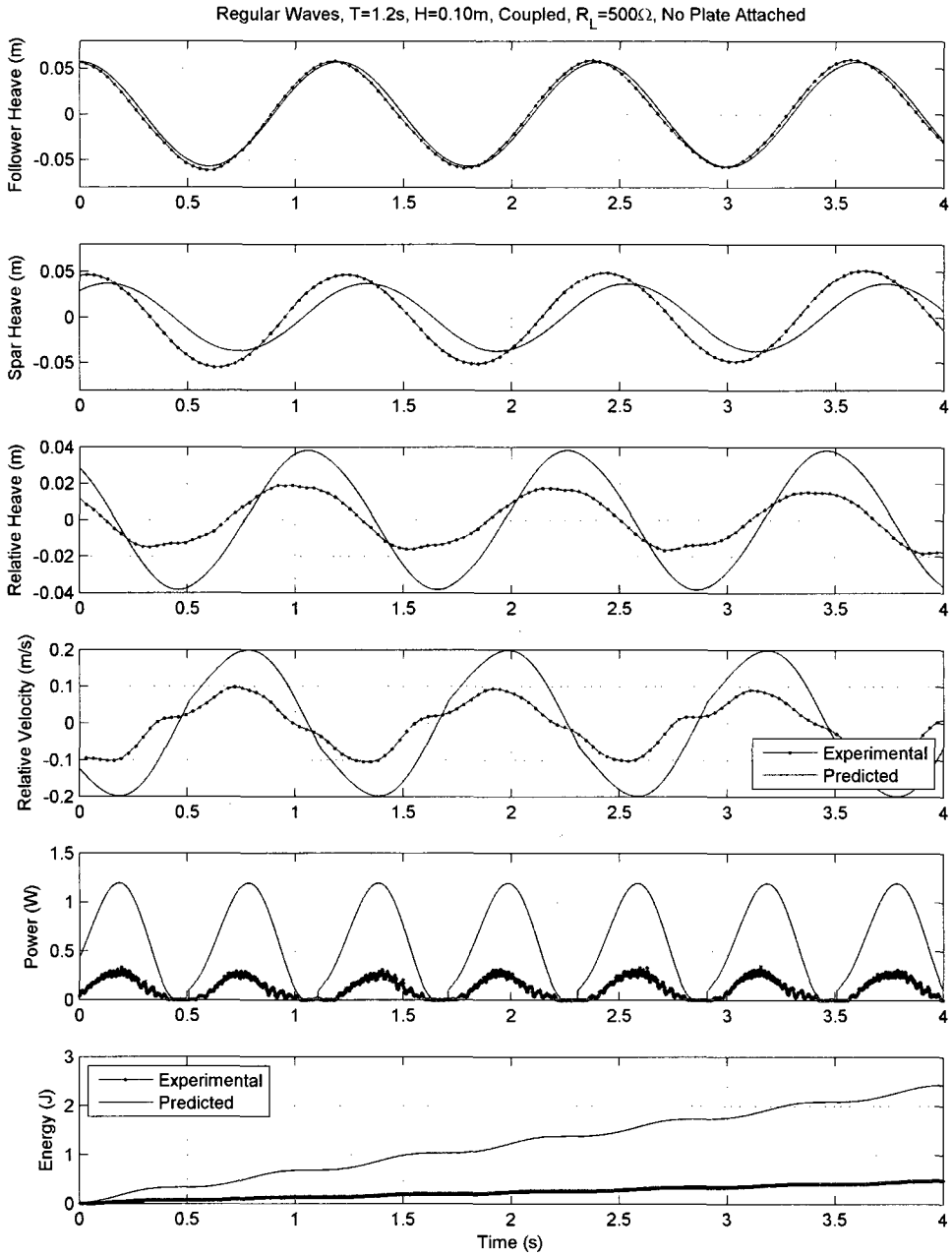

Figure B-22: Validation comparisons for coupled WEC System with no submerged plate. ($T = 1.2s$, $H = 0.10m$, *and* $R_L = 500\Omega$)

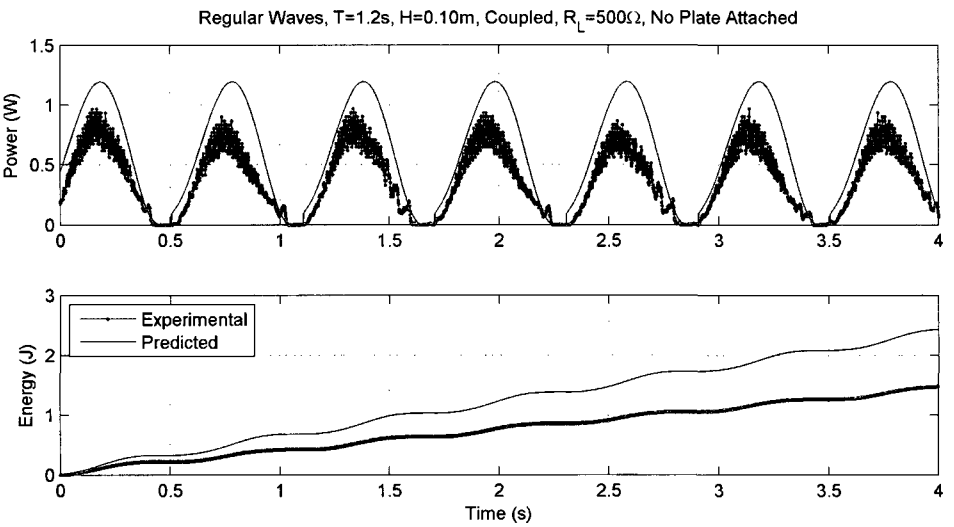

Figure B-23: Validation comparisons for coupled WEC System with no submerged plate. ($T = 1.2s,\ H = 0.10m,\ and\ R_L = 500\Omega$)

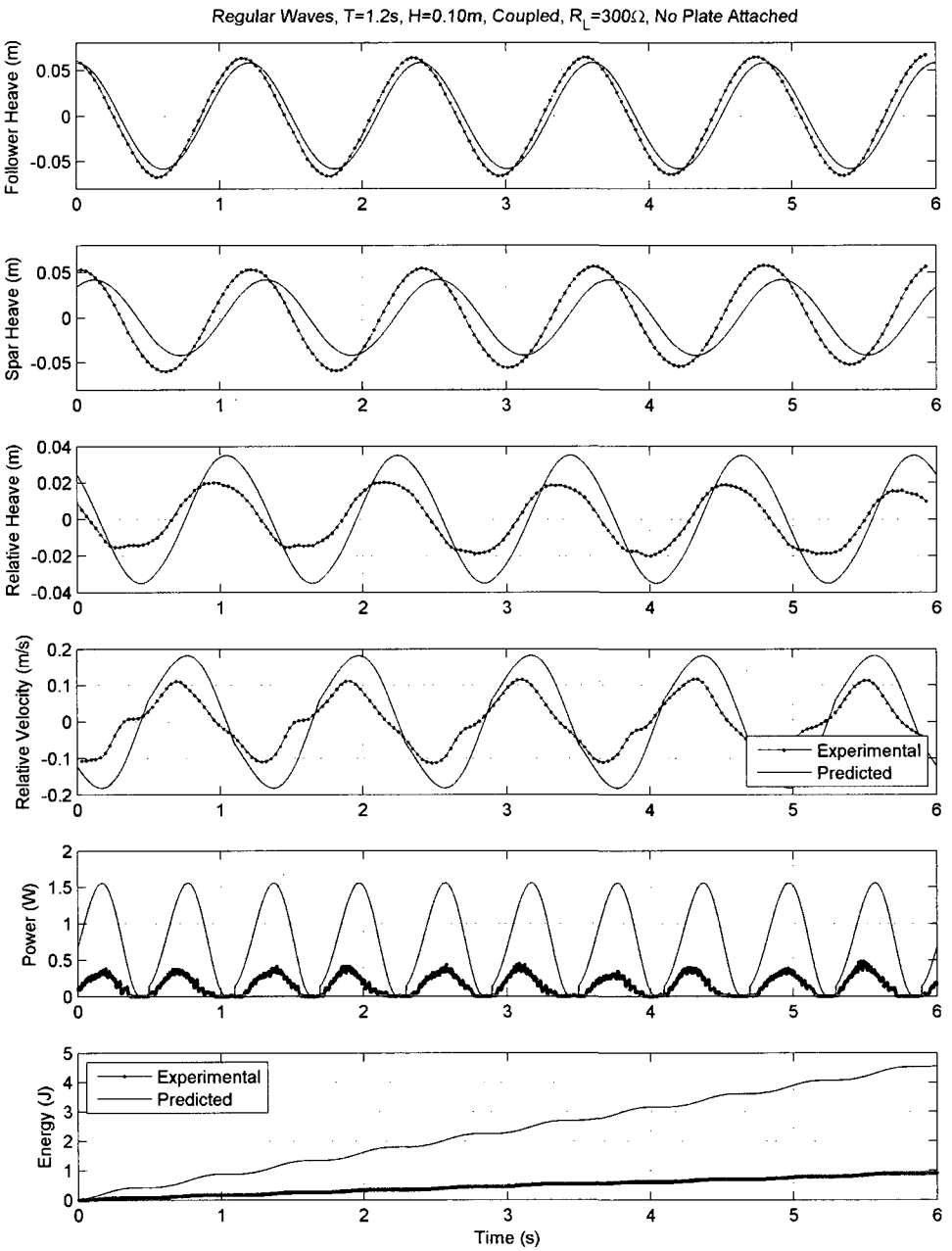

Figure B-24: Validation comparisons for coupled WEC System with no submerged plate. ($T = 1.2s,\ H = 0.10m,\ and\ R_L = 300\Omega$)

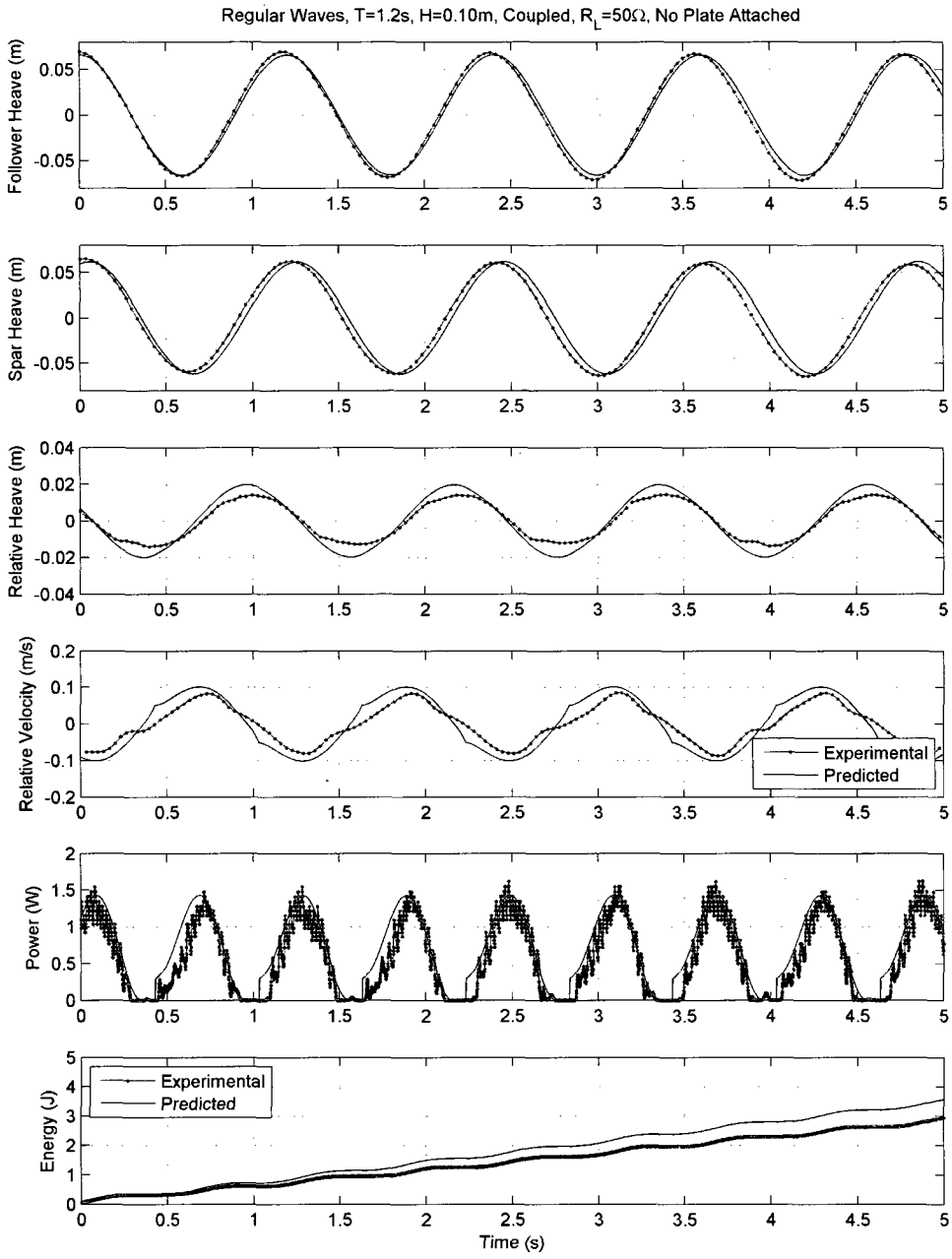

Figure B-25: Validation comparisons for coupled WEC System with no submerged plate. ($T = 1.2s$, $H = 0.10m$, *and* $R_L = 50\Omega$)

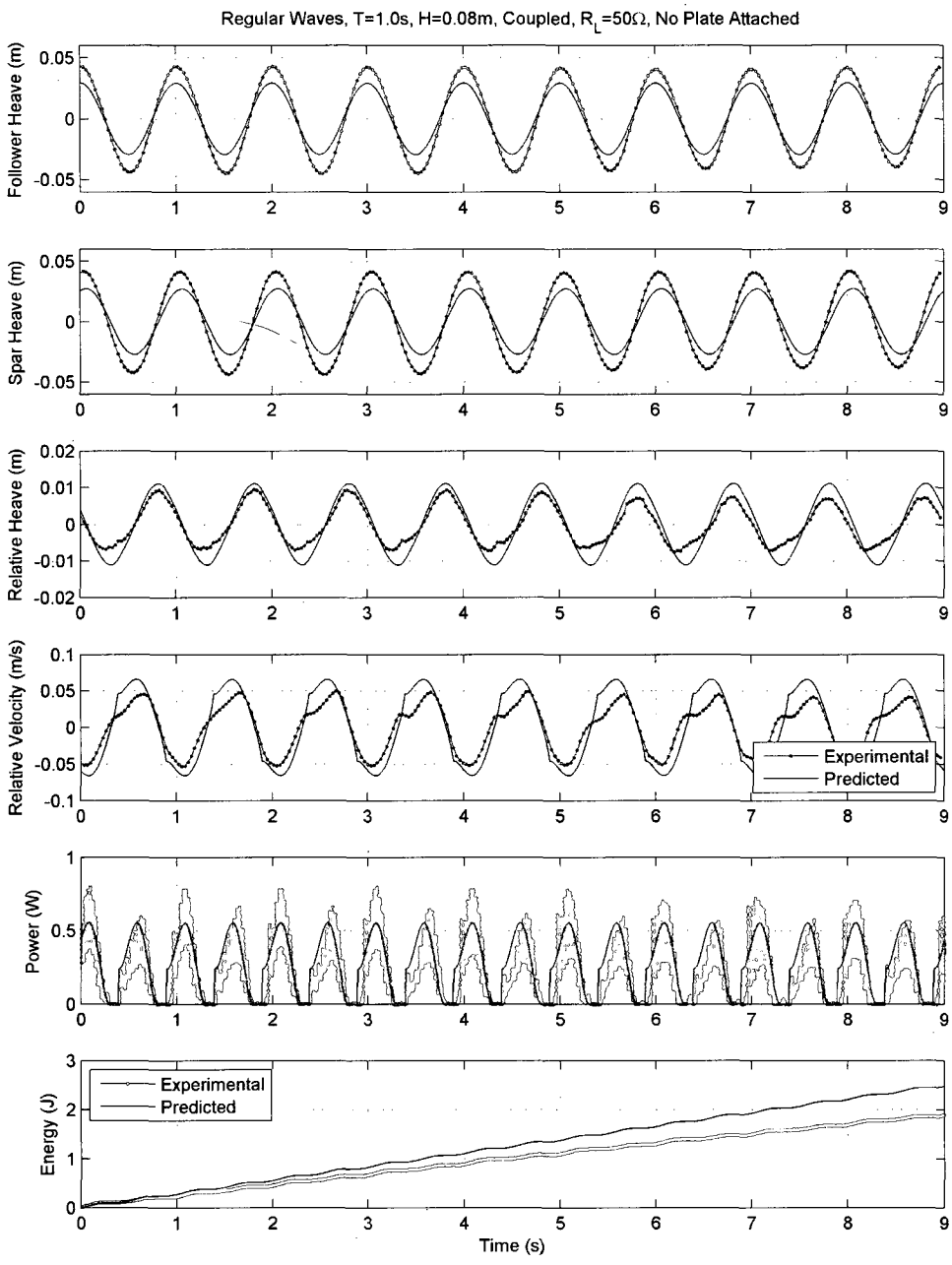

Figure B-26: Validation comparisons for coupled WEC System with no submerged plate. ($T = 1.0s$, $H = 0.08m$, *and* $R_L = 50\Omega$)

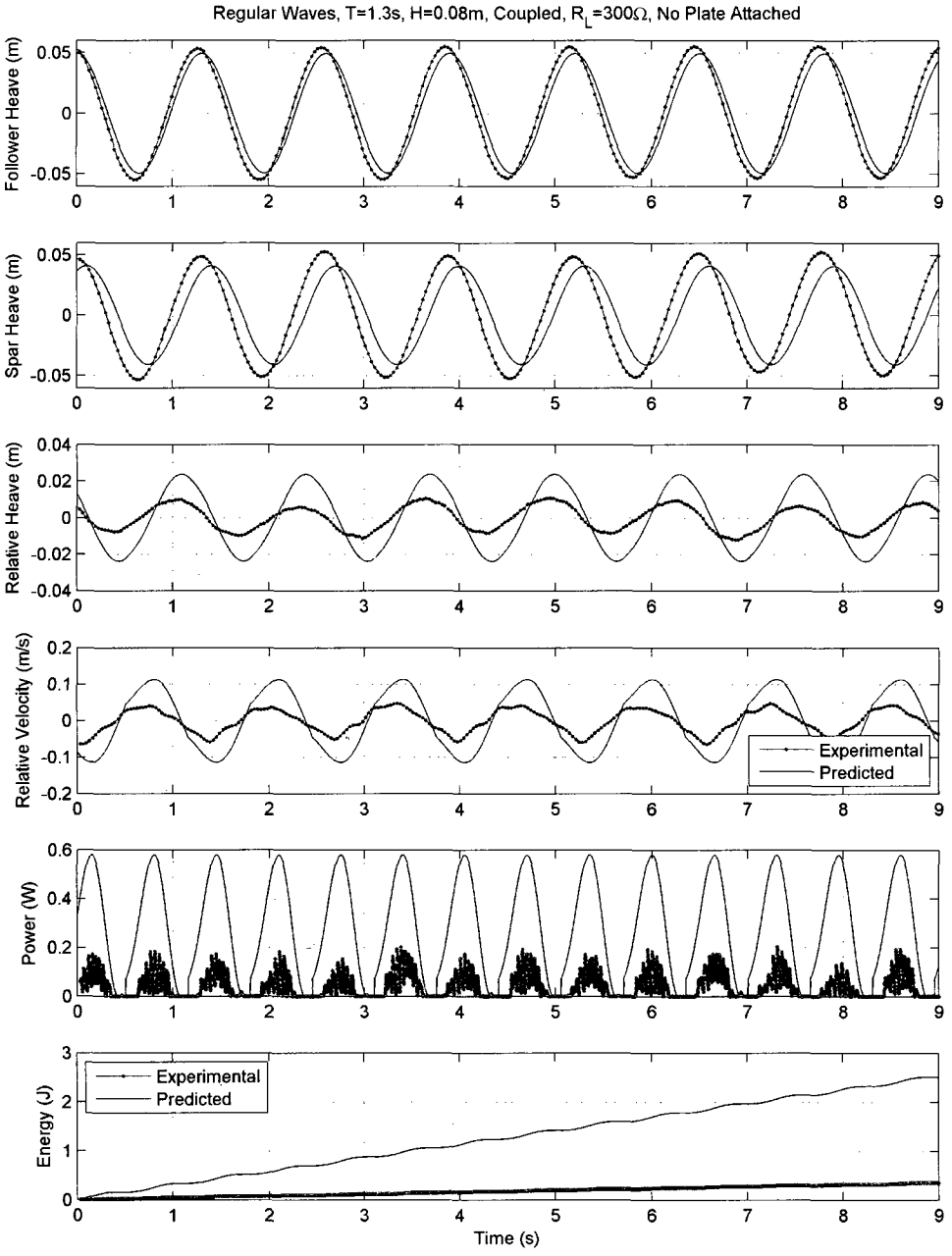

Figure B-27: Validation comparisons for coupled WEC System with no submerged plate. ($T = 1.3s$, $H = 0.08m$, *and* $R_L = 300\Omega$)

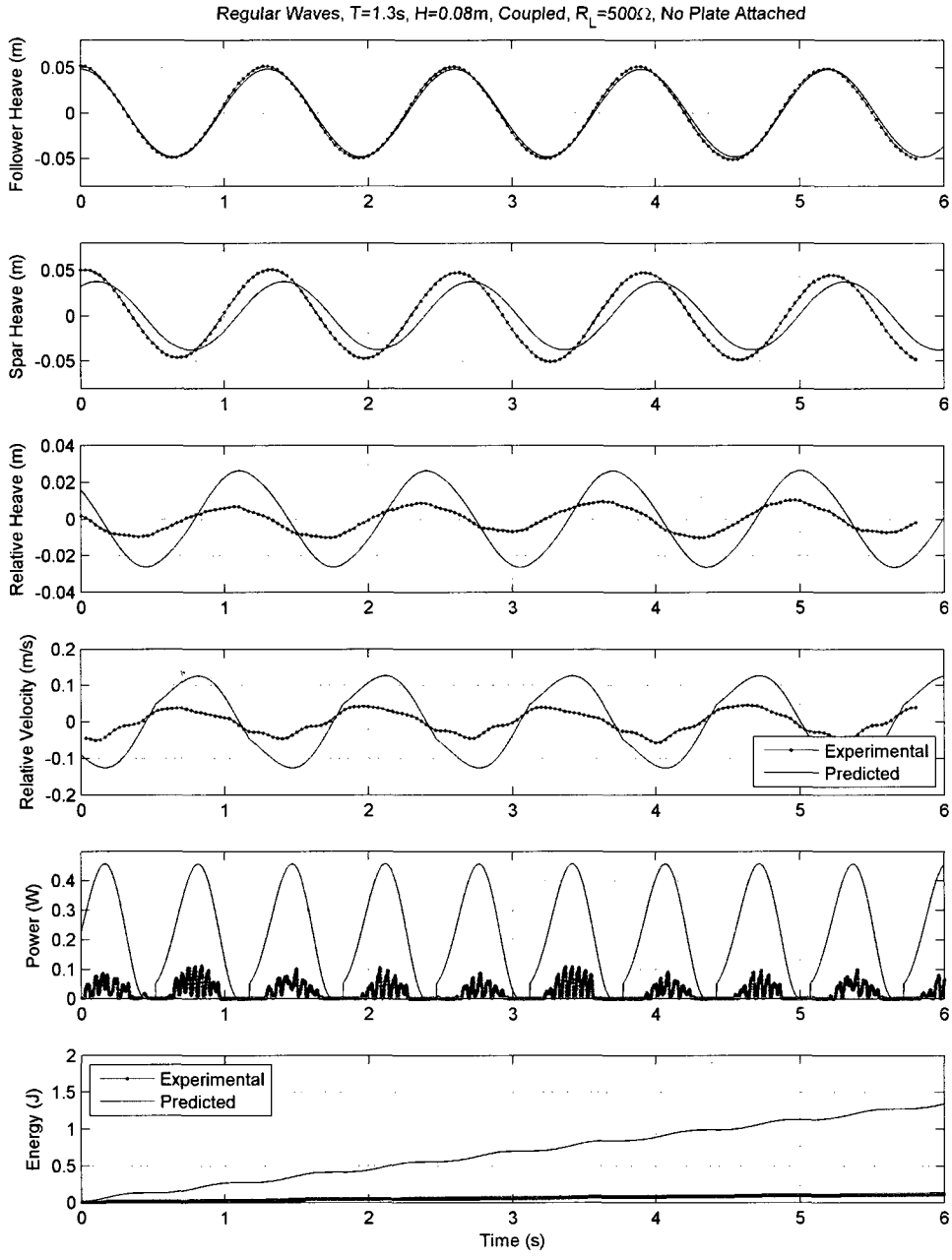

Figure B-28: Validation comparisons for coupled WEC System with no submerged plate. ($T = 1.3s$, $H = 0.08m$, *and* $R_L = 500\Omega$)

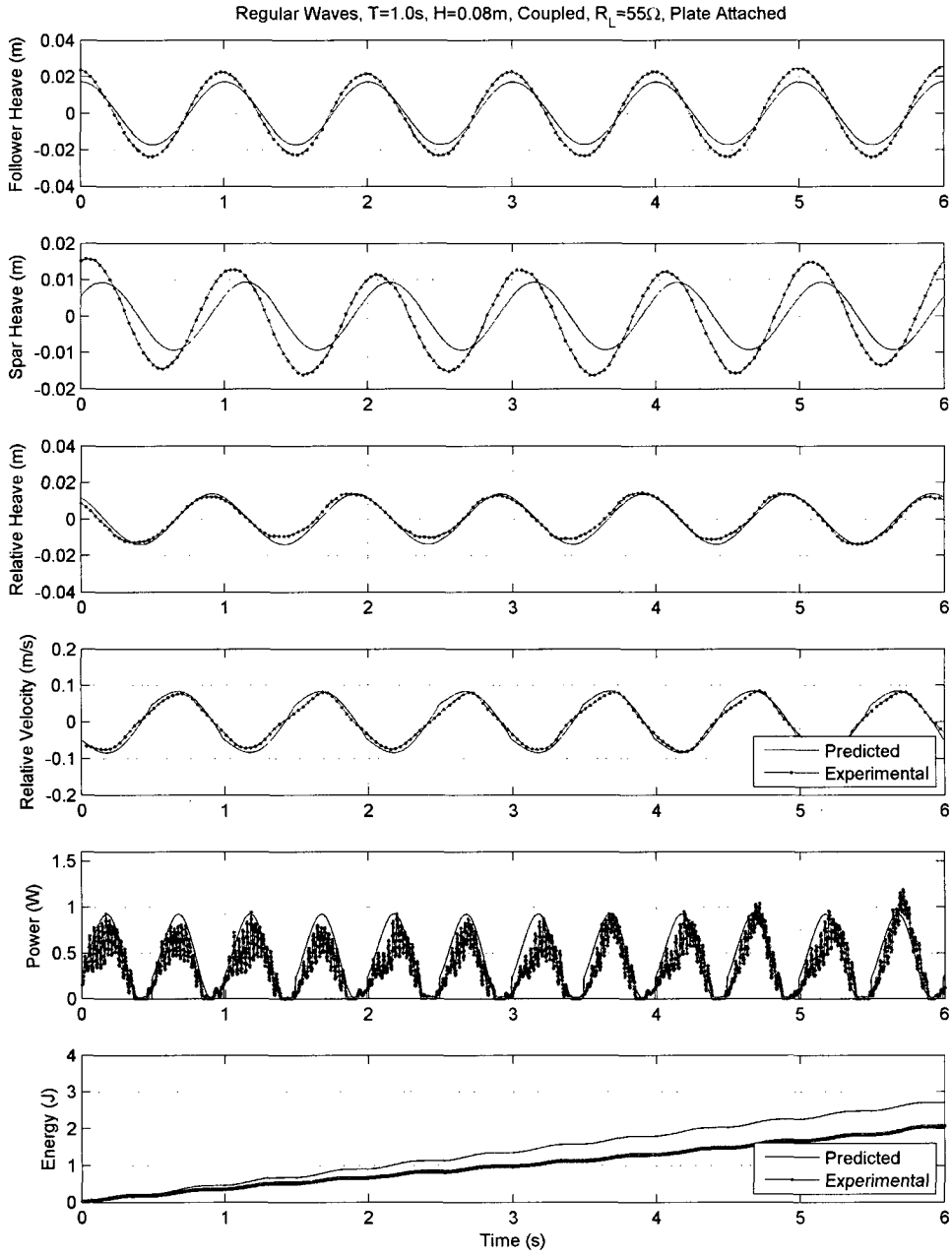

Figure B-29: Validation comparisons for coupled WEC System with submerged plate. ($T = 1s$, $H = 0.08m$, *and* $R_L = 55\Omega$)

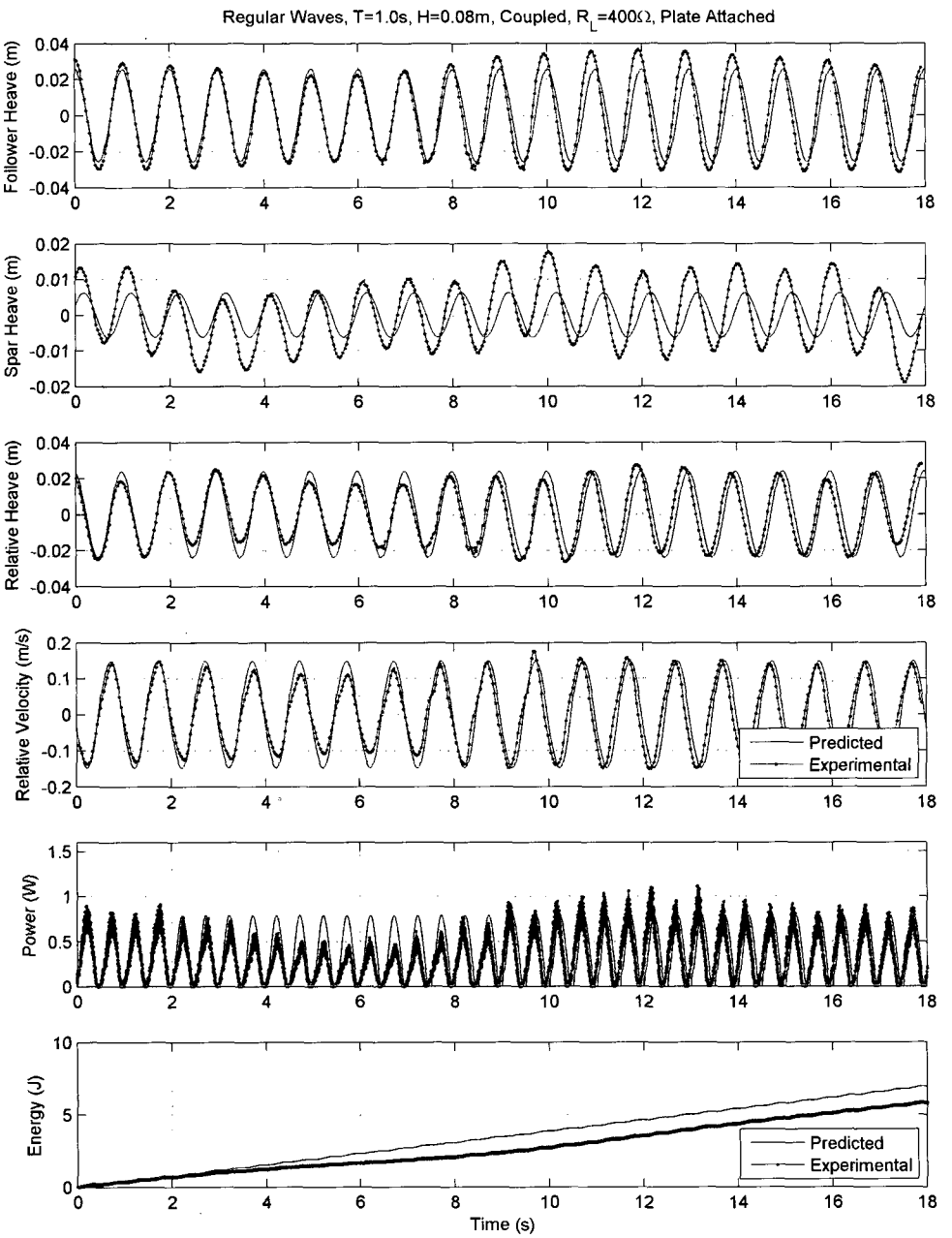

Figure B-30: Validation comparisons for coupled WEC System with submerged plate. ($T = 1s$, $H = 0.08m$, *and* $R_L = 400\Omega$)

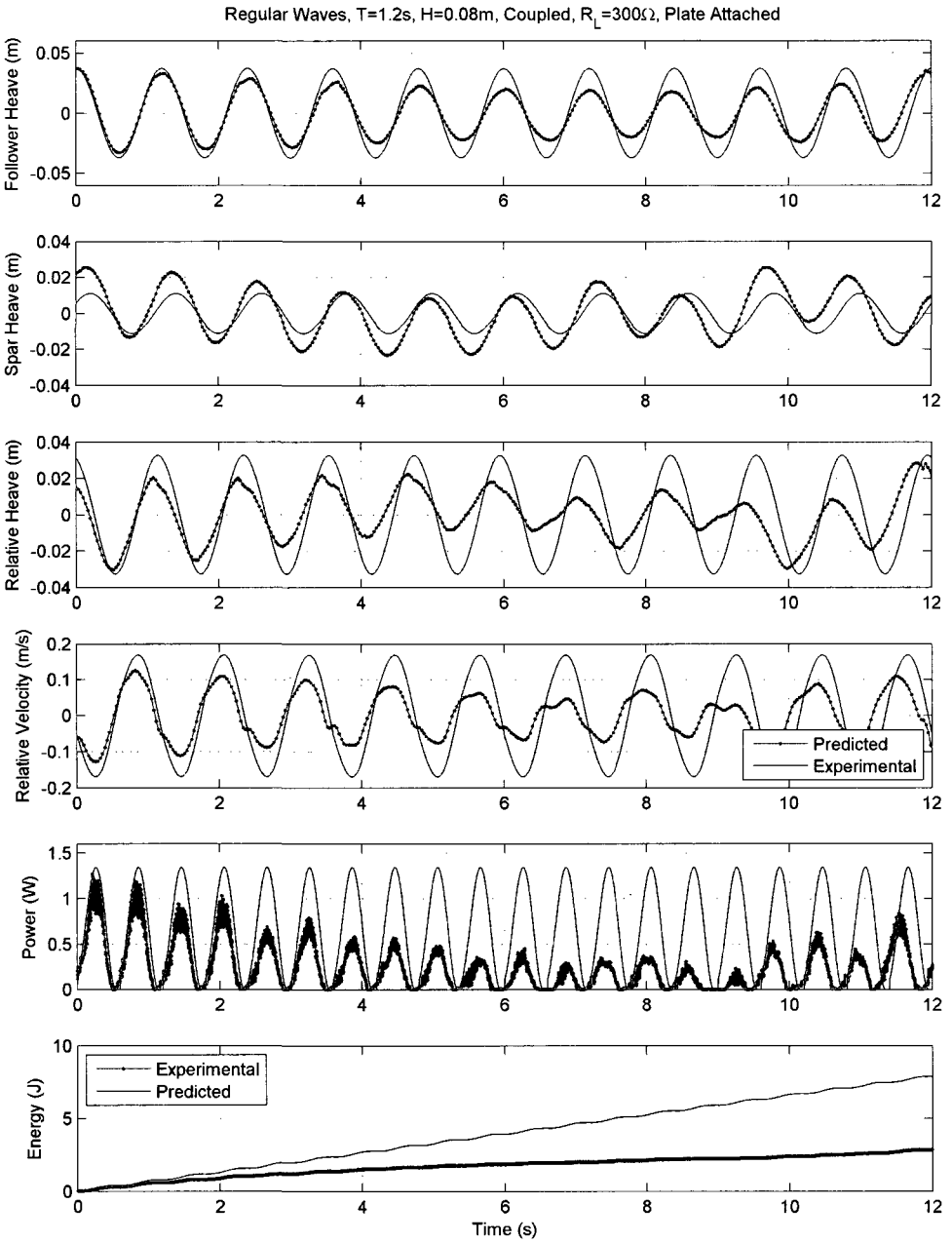

Figure B-31: Validation comparisons for coupled WEC System with submerged plate. ($T = 1.2s$, $H = 0.08m$, *and* $R_L = 300\Omega$)

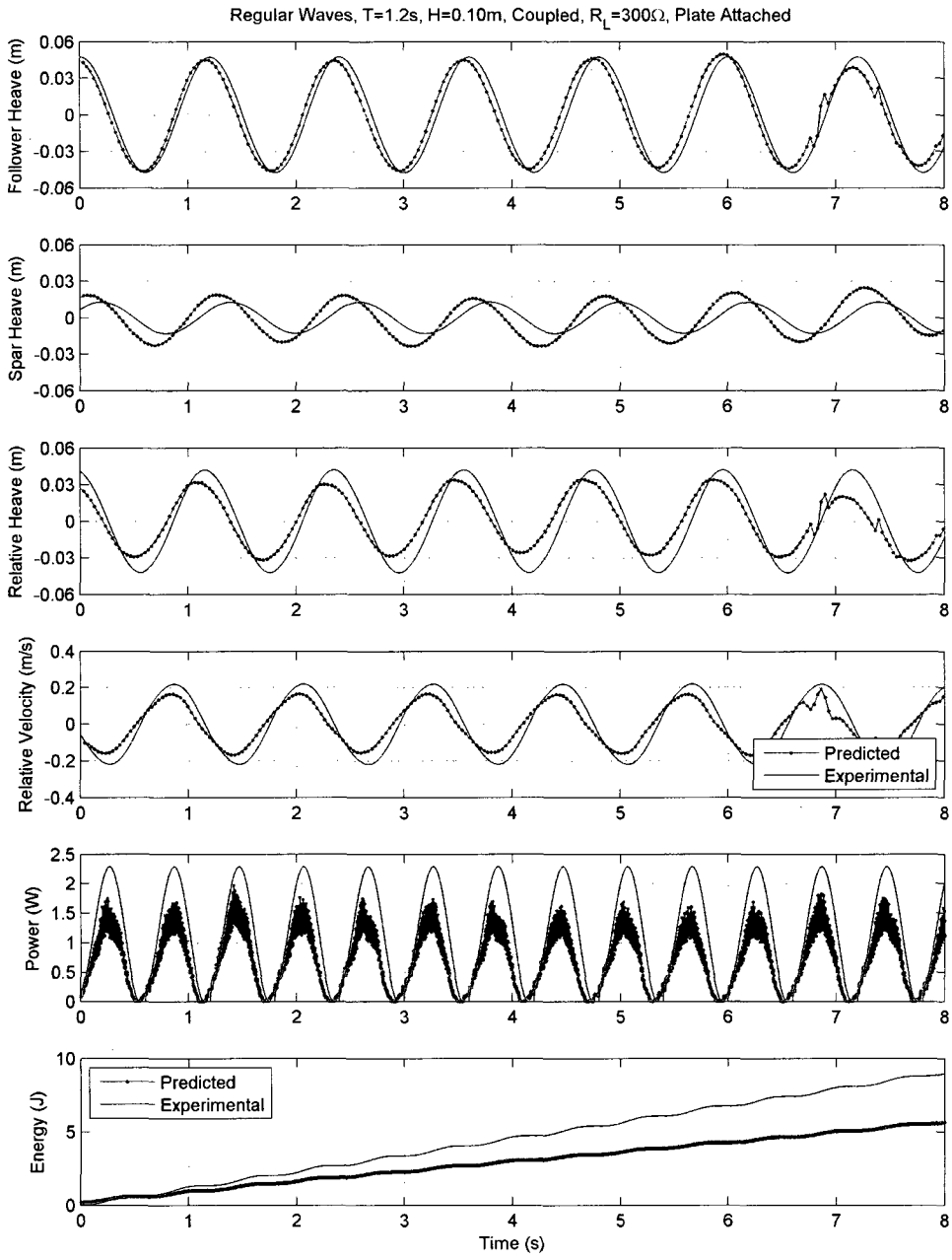

Figure B-32: Validation comparisons for coupled WEC System with submerged plate. ($T = 1.2s$, $H = 0.10m$, *and* $R_L = 300\Omega$)

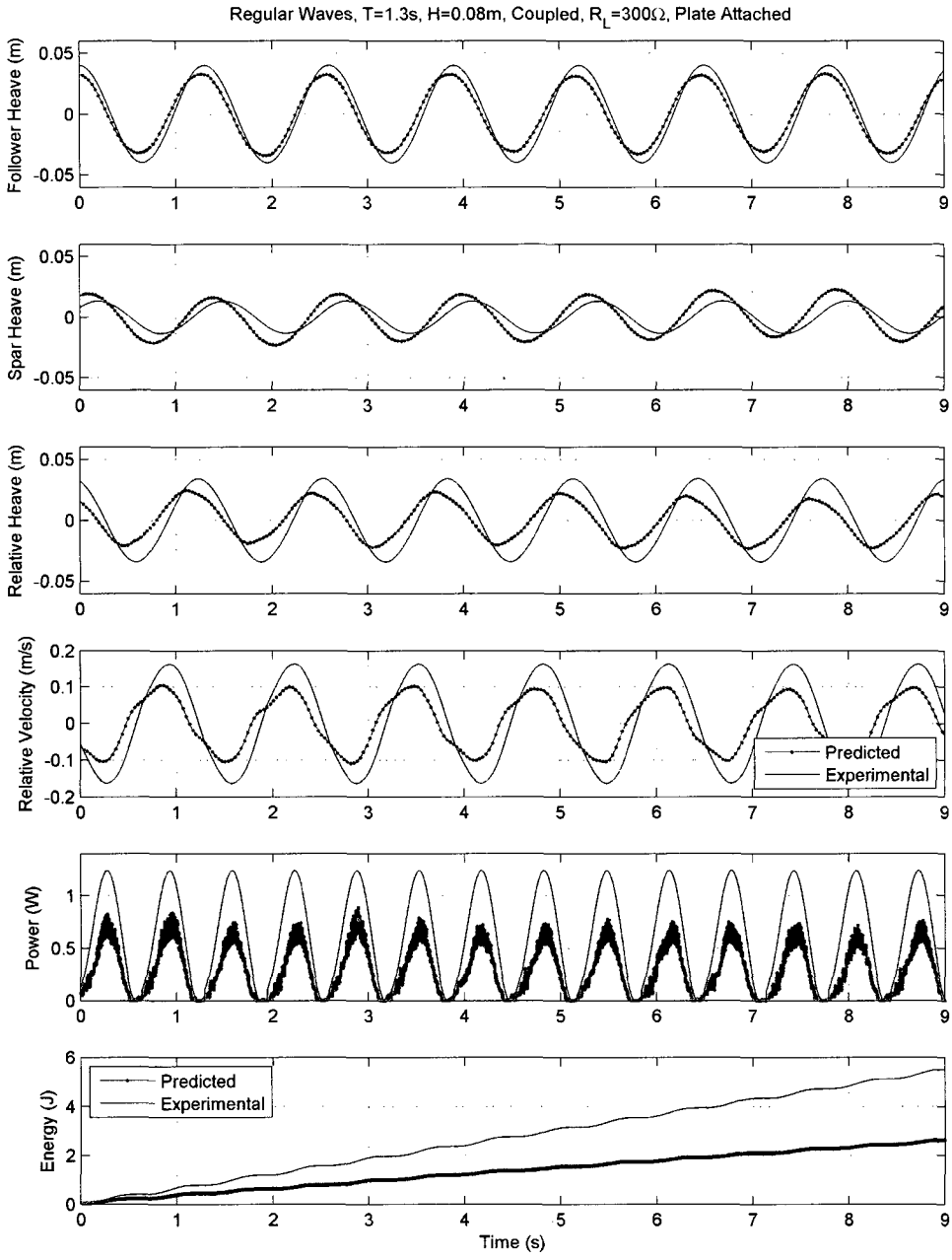

Figure B-33: Validation comparisons for coupled WEC System with submerged plate. ($T = 1.3s$, $H = 0.08m$, *and* $R_L = 300\Omega$)

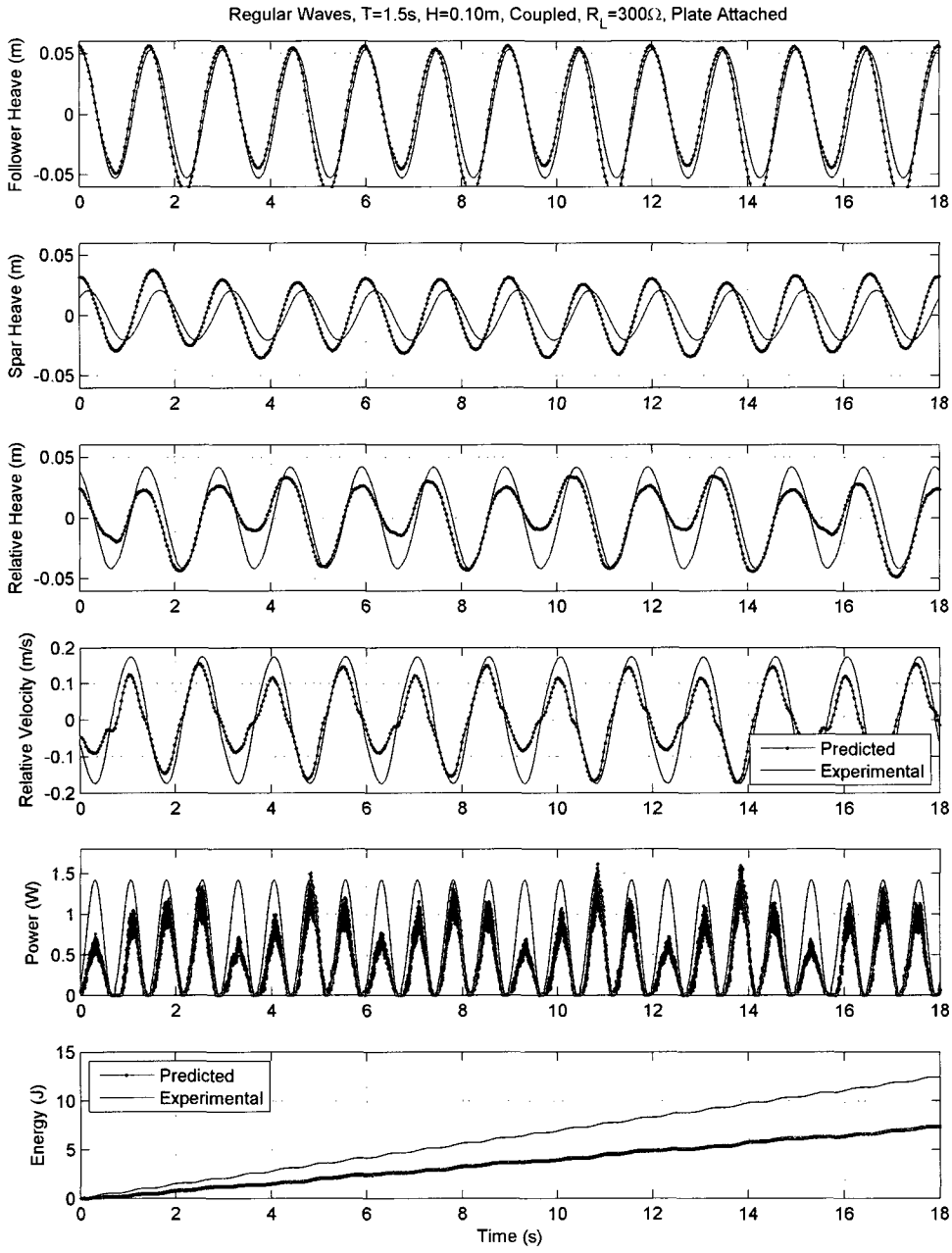

Figure B-34: Validation comparisons for coupled WEC System with submerged plate. ($T = 1.5s$, $H = 0.10m$, *and* $R_L = 300\Omega$)

B.4 Coupled WEC System in Irregular Waves

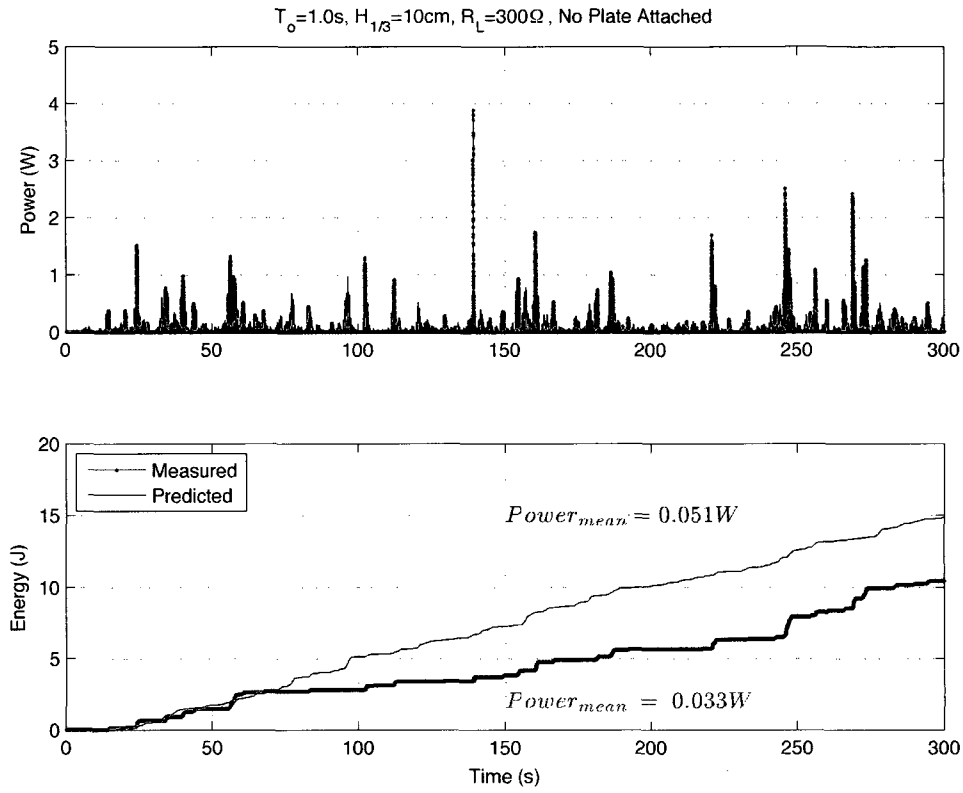

Figure B-35: Validation comparisons for coupled WEC System with no submerged damping plate in irregular waves. ($T_o = 1.0s$, $H_{1/3} = 0.10m$, *and* $R_L = 300\Omega$)

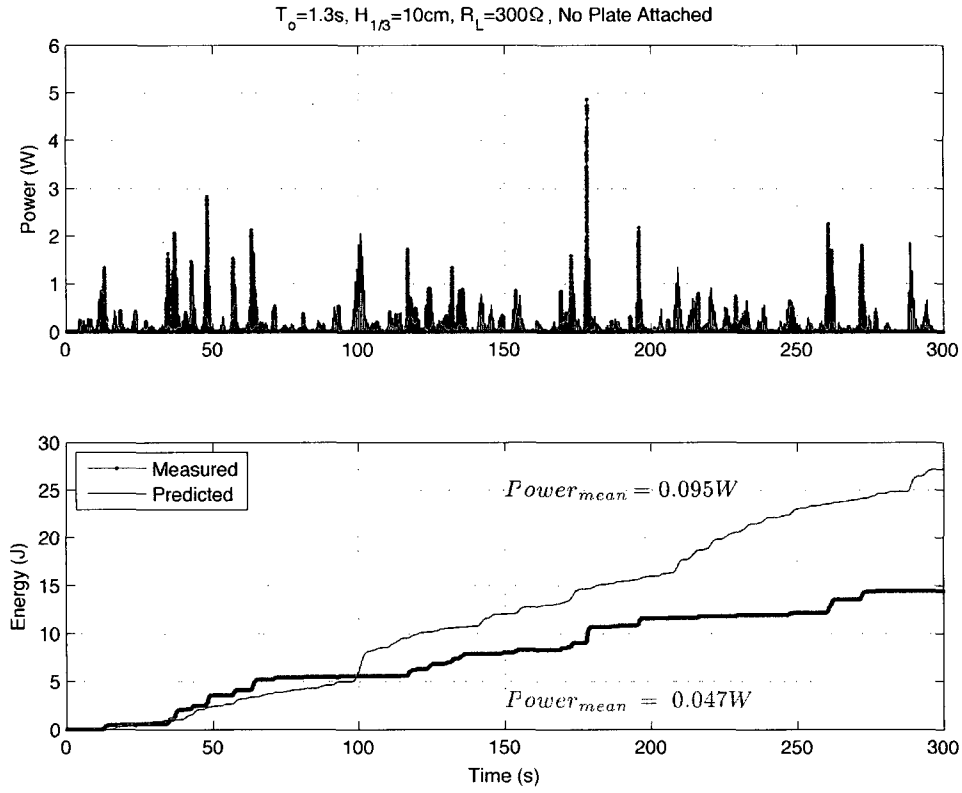

Figure B-36: Validation comparisons for coupled WEC System with no submerged damping plate in irregular waves. ($T_o = 1.3s,\ H_{1/3} = 0.10m,\ and\ R_L = 300\Omega$)

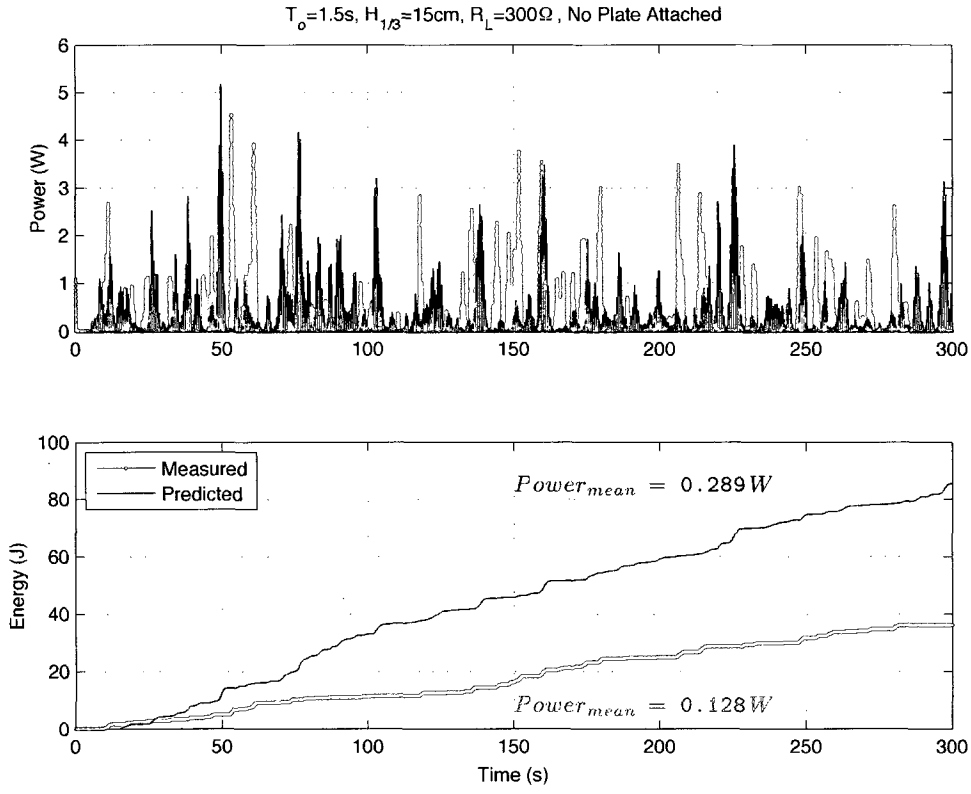

Figure B-37: Validation comparisons for coupled WEC System with no submerged damping plate in irregular waves. ($T_o = 1.5s,\ H_{1/3} = 0.15m,\ and\ R_L = 300\Omega$)

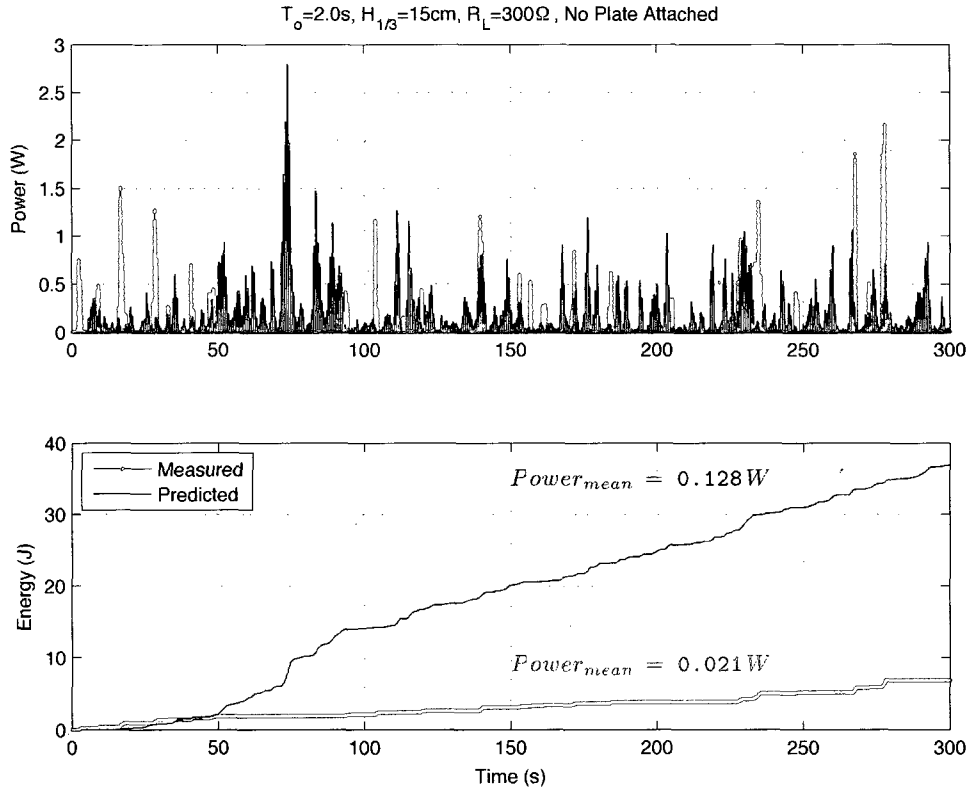

Figure B-38: Validation comparisons for coupled WEC System with no submerged damping plate in irregular waves. ($T_o = 2.0s,\ H_{1/3} = 0.15m,\ and\ R_L = 300\Omega$)

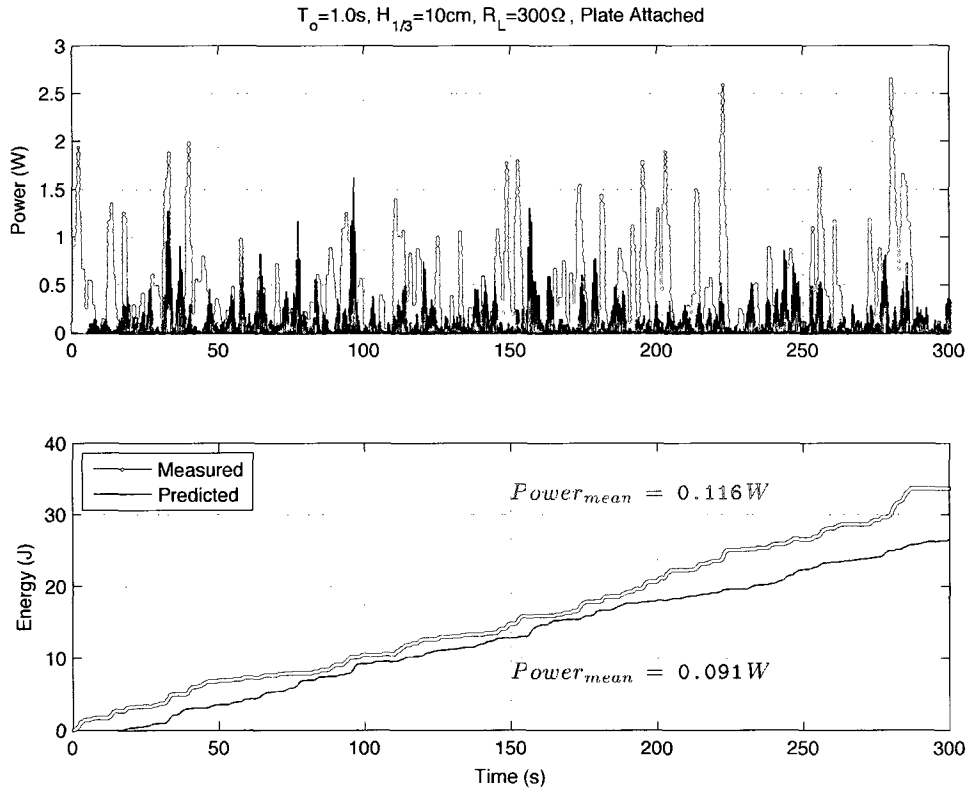

Figure B-39: Validation comparisons for coupled WEC System with a submerged damping plate in irregular waves. ($T_o = 1.0s,\ H_{1/3} = 0.10m,\ and\ R_L = 300\Omega$)

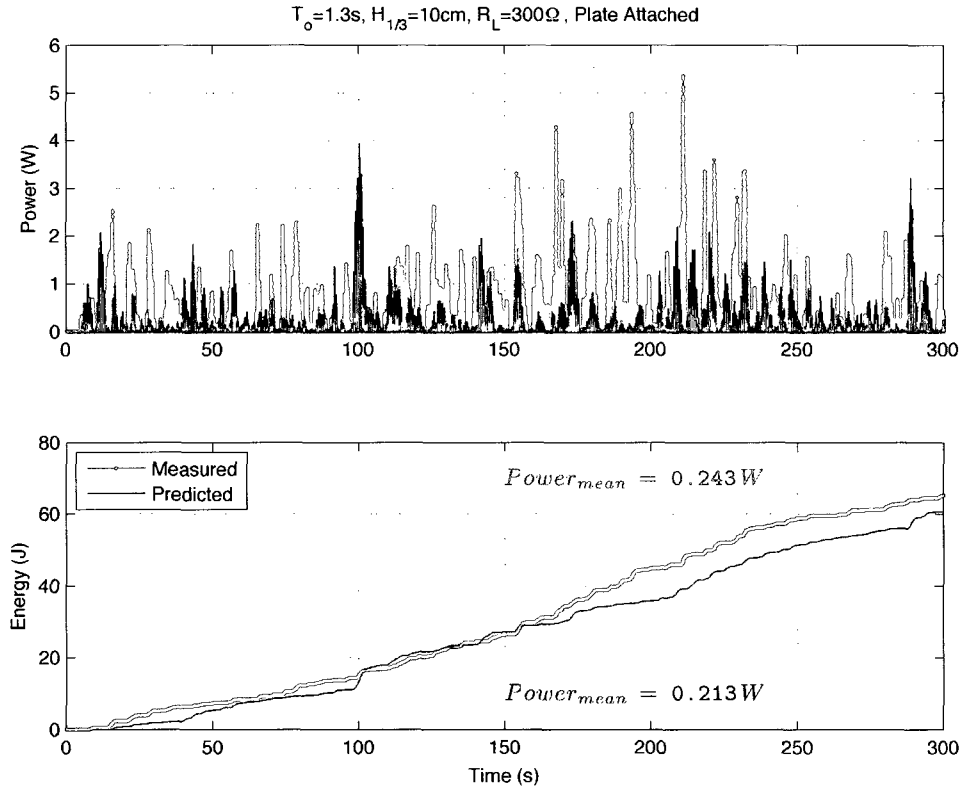

Figure B-40: Validation comparisons for coupled WEC System with a submerged damping plate in irregular waves. ($T_o = 1.3s,\ H_{1/3} = 0.10m,\ and\ R_L = 300\Omega$)

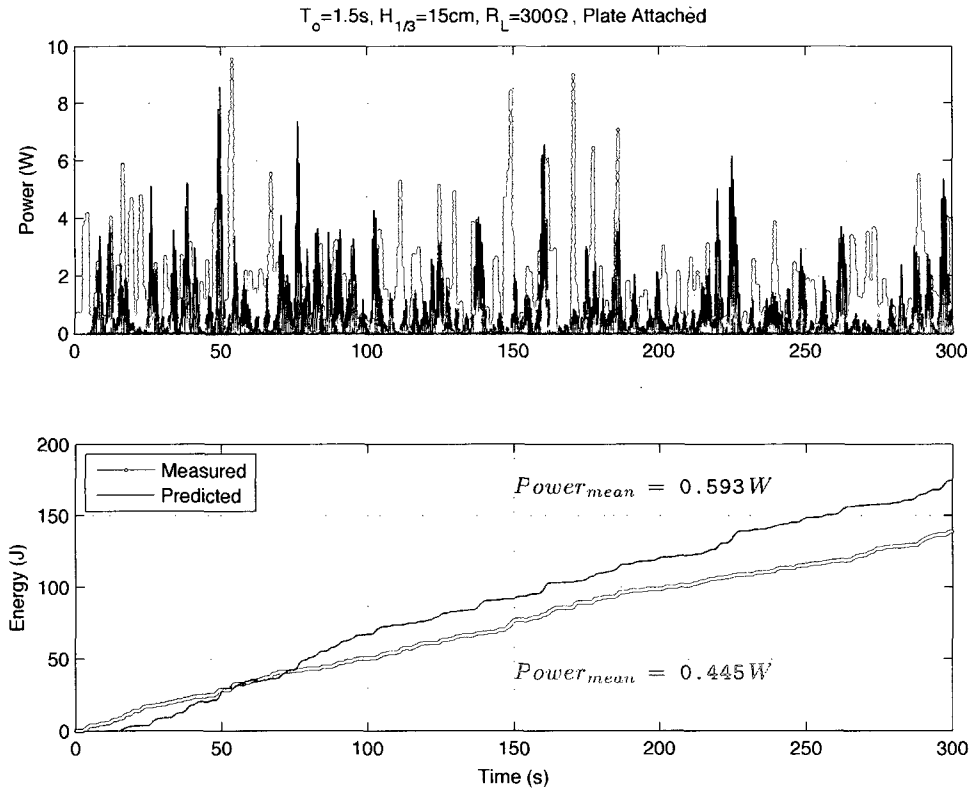

Figure B-41: Validation comparisons for coupled WEC System with a submerged damping plate in irregular waves. ($T_o = 1.5s,\ H_{1/3} = 0.15m,\ and\ R_L = 300\Omega$)

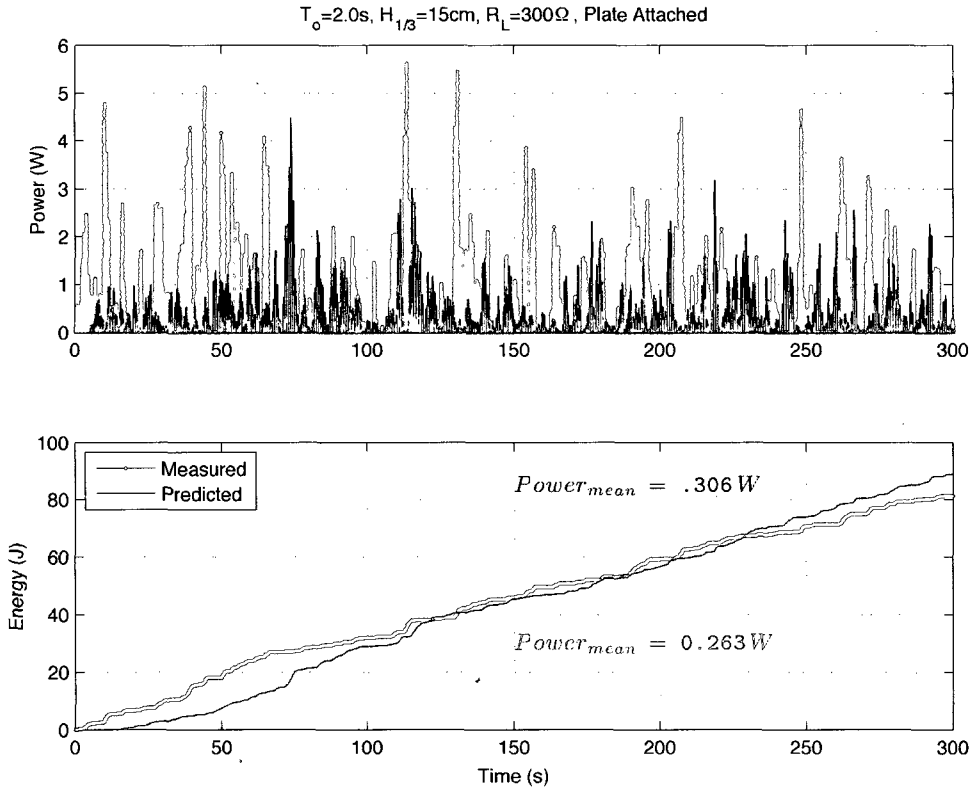

Figure B-42: Validation comparisons for coupled WEC System with a submerged damping plate in irregular waves. ($T_o = 2.0s$, $H_{1/3} = 0.15m$, *and* $R_L = 300\Omega$)

APPENDIX C

MATLAB Code

Bretschneider_Spectrum.m generates a discrete time-series of surface elevation, surface velocity, and surface acceleration for a given Bretschneider Spectrum defined by the significant wave height ($H_{1/3}$) and nodal frequency (f_o).

```
%% Bretschneider_Spectrum.m
% Generate a Synthetic Time Series from the Bretschneider Spectrum
clc; close all; clear all;

%% Synthetic Real Time Series
N=100000; % #pts in time series
Δ=.02; % seconds between pts in time series
j= [1:(N/2)-1]; % index 1 to N/2-1
f=j./(N*Δ); % range of frequencies, equally spaced

%%
% Bretschneider Spectrum
H13 = 4.0; %Significant Wave Height (m)
fo = 1/7;  %Peak Frequency (Dominant Period)
S = 5.*(H13.^2)./(16*fo).*(f./fo).^(-5).*exp((-5/4).*(f./fo).^(-4));

%% Plot Spectrum
subplot(2,1,1)
plot(f,S,'-')
title('Bretschneider Spectrum')
xlabel('Frequency (1/s)')
ylabel('Wave Spectral Density (m^{2}s)')
axis([0 2 0 15])
legend(['H_{1/3} = ' num2str(H13,3) ' & T_o = ' num2str(1/fo,3)])

%% Solve for Time Series
% Solve for Cj (amplitide)
C=sqrt(S./(2*N*Δ));
% Solve for Random phases
phase=(2*pi).*rand(1,(N/2)-1);
% Solve for A and B using symmetry
```

```
a=C.*cos(phase);
b=C.*sin(phase);
A=[0 a 0 fliplr(a)];
B=[0 b 0 -fliplr(b)];
% Inverse transform
y = ifft(A+(1i.*B)).*N; %Surface Elevation (m)
% Time
t = [0:Δ:N*Δ-Δ];

%% Plot Synthetic Time Series
subplot(2,1,2)
plot(t,y,'k-')
title('Synthetic Time Series')
xlabel('Time (seconds)')
ylabel('Surface Elevation (m)')
% axis([0 60 -.2 .2])
grid

%% Differentiate Surface Position for Velocity and Acceleration
dy = diff(y)./diff(t);
dys = fastsmooth(dy,15,2,1);
dyy = diff(dys)./diff(t(1:end-1));
dyys = fastsmooth(dyy,5,2,1);

%% Plot Output values
figure(2)
subplot(3,1,1); plot(t,y)
ylabel('$y$','Interpreter','latex')
axis([0 30 -3 3])
subplot(3,1,2); plot(t(1:end-1),dys,'-')
ylabel('$\dot{y}$','Interpreter','latex')
axis([0 30 -4 5])
subplot(3,1,3); plot(t(1:end-2),dyys,'-')
xlabel('Time $(s)$','Interpreter','latex')
ylabel('$\ddot{y}$','Interpreter','latex')
axis([0 30 -10 10])

%% Relabel Values
RealSea(1,:) = t;
RealSea(2,:) = y;
RealSea(3,:) = [dys dys(end)];
RealSea(4,:) = [dyys dyys(end) dyys(end)] ;

%% Save Output
save('UNHRealSea.mat','RealSea')
```

REFERENCES

Aws ocean energy, 2009. URL www.awsocean.com.

Finavera renewables, 2009. URL www.finavera.com.

Ocean power technologies, 2009. URL www.oceanpowertechnologies.com.

Pelamis wave power ltd, 2009. URL www.pelamiswave.com.

H. O. Berteaux. *Buoy Engineering.* John Wiley and Sons, 1976.

H. O. Berteaux. *Coastal and Oceanic Buoy Engineering.* H. O. Berteaux, 1991.

J. Brooke. *Wave Energy Conversion*, volume 6 of *Elsevier Ocean Engineering.* Elservier, 2003.

P. Cantillon-Murphy. An evaluation of current trends in tidal and wave energy conversion. April 2005.

R. G. Dean and R. A. Dalrymple. *Water Wave Mechanics for Engineers and Scientists.* Prentince Hall, Inc., 1984.

J. Falnes. A review of wave-energy extraction. *Marine Structures*, (20):185–201, 2007.

B. S. Guru and H. R. Hiziroğlu. *Electric Machinery and Transormers.* Oxford University Press, third edition, 2001.

D. C. Ipsen. *Units, dimensions, and dimensionless numbers.* McGraw-Hill, New York, 1960.

F. J. and B. K. Wave power conversion by point absorbers. *Norwegian Maritime Res*, 1978.

S. Kelly. Hydrodynamic optimisation of a point wave-energy converter using laboratory experiments hydrodynamic optimisation of a point wave-energy converter using laboratory experiments. Master's thesis, The University of Auckland, New Zealand, 2007.

T. Kenjo and S. Nagamori. *Permanent-Magnet and Brushless DC Motors.* Oxford University Press, 1985.

G. H. Mike Previsic, Roger Bedard. E2i epri assessment: Offshore wave enegy conversion devices. Technical report, 2004.

K. Ogata. *System Dynamics.* Prentice Hall, fourth edition, 2004.

E. B. Page. An innovative approach to dc motor characterization. *First Motorcon*, 1981.

T. Thorpe. A review of wave energy. Technical report, Dept. of Trade and Industry, 1992.

J. G. Vining. Ocean wave energy converters: Overview, legal and economic aspects, and direct-drive power take-off. Master's thesis, University of Wisconsin-Madison, 2007.

F. M. White. *Fluid Mechanics*. McGraw-Hill, New York, 1994.